DIGITAL ACCESS TO SCHOLARSHIP AT HARVARD
DASH.HARVARD.EDU

HARVARD LIBRARY

Coherent control of diamond defects for quantum information science and quantum sensing

Citation

Maurer, Peter. 2014. Coherent control of diamond defects for quantum information science and quantum sensing. Doctoral dissertation, Harvard University.

Link

http://nrs.harvard.edu/urn-3:HUL.InstRepos:12269840

Terms of use

This article was downloaded from Harvard University's DASH repository, and is made available under the terms and conditions applicable to Other Posted Material (LAA), as set forth at
https://harvardwiki.atlassian.net/wiki/external/NGY5NDE4ZjgzNTc5NDQzMGIzZWZhMGFlOWI2M2EwYTg

Accessibility

https://accessibility.huit.harvard.edu/digital-accessibility-policy

Share Your Story

The Harvard community has made this article openly available.
Please share how this access benefits you. Submit a story

Coherent control of diamond defects for quantum information science and quantum sensing

A dissertation presented

by

Peter Maurer

to

The Department of Physics

in partial fulfillment of the requirements

for the degree of

Doctor of Philosophy

in the subject of

Physics

Harvard University

Cambridge, Massachusetts

April 2014

©2014 - Peter Maurer

All rights reserved.

Dissertation Advisor: Author

Professor Mikhail D. Lukin **Peter Maurer**

Coherent control of diamond defects for quantum information science and quantum sensing

Abstract

Quantum mechanics, arguably one of the greatest achievements of modern physics, has not only fundamentally changed our understanding of nature but is also taking an ever increasing role in engineering. Today, the control of quantum systems has already had a far-reaching impact on time and frequency metrology. By gaining further control over a large variety of different quantum systems, many potential applications are emerging. Those applications range from the development of quantum sensors and new quantum metrological approaches to the realization of quantum information processors and quantum networks. Unfortunately most quantum systems are very fragile objects that require tremendous experimental effort to avoid dephasing. Being able to control the interaction between a quantum system with its local environment embodies therefore an important aspect for application and hence is at the focus of this thesis.

Nitrogen Vacancy (NV) color centers in diamond have recently attracted attention as a room temperature solid state spin system that expresses long coherence times. The electronic spin associated with NV centers can be efficiently manipulated, initialized and readout using microwave and optical techniques. Inspired by these extraordinary properties, much effort has been dedicated to use NV centers as a building block for scalable room

temperature quantum information processing and quantum communication as well as a quantum sensing.

In the first part of this thesis we demonstrate that by decoupling the spin from the local environment the coherence time of a NV quantum register can be extended by three order of magnitudes. Employing a novel dissipative mechanism in combination with dynamical decoupling, memory times exceeding one second are observed. The second part shows that, based on quantum control, NV centers in nano-diamonds provide a nanoscale temperature sensor with unprecedented accuracy enabling local temperature measurements in living biological cells. This opens the door for the engineering of nano-scaled chemical reactions to the study of temperature dependent biological processes. Finally, a novel technique is introduced that facilitates optical spin detection with nanoscale resolution based on an optical far-field technique; by combining this with a 'quantum Zeno' like effect coherent manipulation of nominally identical spins at a nanoscale is achieved.

Contents

Title Page i
Abstract iii
Table of Contents v
Citations to Previously Published Work viii
Acknowledgments ix
Dedication xiii

1 Introduction **1**
1.1 Background 1
1.1.1 Motivation 1
1.1.2 Controlled quantum systems 5
1.2 Nitrogen vacancy centers in diamond 9
1.3 Overview of the thesis 15
1.3.1 Room-temperature quantum bit memory exceeding one second . . . 15
1.3.2 Nanometer scale thermometry in a living cell 16
1.3.3 Far-field optical imaging and manipulation of individual spins with nanoscale resolution 17

2 Room-Temperature Quantum Bit Memory Exceeding One Second **18**
2.1 Introduction 18
2.2 NV Based quantum register 19
2.3 Single shoot readout of single nuclear spin 22
2.4 Laser induced motional averaging rate 25
2.5 Photon counting statistics and readout fidelity 27
2.6 Second long coherence time 31
2.7 NV based quantum memory 33
2.8 Maximal storage time 36
2.9 Conclusions and outlook 37

3 Nanometer Scale Thermometry in a Living Cell **39**
3.1 Introduction 39

3.2 NV based thermometry 41
3.3 Sensing temperature with confocal resolution 45
3.4 Injection of nanodiamonds into cells 50
3.5 Temperature sensing in a single living cell 52
3.6 Ultimate sensitivity 55
3.7 Conclusions and outlook 56

4 Far-field Optical Imaging and Manipulation of Individual Spins with Nanoscale Resolution 58
4.1 Introduction 58
4.2 The concept of sub-diffraction spin detection and control 60
4.3 Nanoscale optical imaging using spin state 62
4.4 Spin imaging resolution 65
4.5 Sub-wavelength optical magnetometry 66
4.6 Measurements of local magnetic field environment 68
4.7 Coherent spin control 69
4.8 Inhibition mechanism of electronic-spin rabi oscillations 73
4.9 Conclusions and outlook 78

5 Conclusions and Outlook 81
5.1 Room-temperature quantum bit memory exceeding one second 82
5.2 Nanometer scale thermometry in a living cell 84
5.3 Far-field optical imaging and manipulation of individual spins with nanoscale resolution 87

A Repetitive Readout of a Single Electronic Spin via Quantum Logic with Nuclear Spin Ancillae 91
A.1 Introduction 91
A.2 Quantum logic for improved readout fidelity 93
A.3 Repetitive Readout with one nuclear spin 97
A.4 Imperfections and optically induced depolarization 101
A.5 Repetitive readout with two nuclear spins 101
A.6 Limitations 103
A.7 Conclusion 105

B Scalable Architecture for a Room Temperature Solid-State Quantum Information Processor 107
B.1 Introduction 107
B.2 Motivation for NV based quantum information processor 108
B.3 The NV Qubit Register 110
B.4 Qubit control based on Laguerre-Gaussian beams 113
B.5 Arbitrary Two-Qubit Gates within the NV Register 115

B.6 Approach to Scalable Architecture 115
B.7 Dark Spin Chain Data Bus 118
B.8 Controlling Qubit-Chain Coupling in the NV Architecture 123
B.9 Specific Implementation of Architecture 125
B.10 Implementation, Operational Errors and Gate Fidelities 127
B.11 Discussion 131

C Supporting material of previous sections 134
C.1 Supporting material of Chapter 2 134
C.1.1 Detailed model nuclear coherence and depolarization 134
C.1.2 Nuclear decoherence under dynamical decoupling 137
C.1.3 Process tomography and fidelity 144
C.2 Supporting material of Chapter 4 148
C.2.1 Imaging resolution under imperfections of the Laguerre-Gaussian mode 149
C.2.2 Measurements of local magnetic field environment with sub-diffraction resolution 152
C.2.3 Coherent single spin manipulation 157
C.2.4 Measurement of individual spin states in coherent manipulation experiments 158

Bibliography 161

Citations to Previously Published Work

With minor modifications the entire Chapter 2 and part of Appendix C have been published in the main text and the supplementary information of

> P. C. Maurer*, G. Kucsko*, C. Latta, L. Jiang, N. Yao, S. Bennett, F. Pastawski, D. Hunger, N. Chisholm, M. Markham, D. Twitchen, I. Cirac, M. D. Lukin, *Multi-second quantum memory based upon a single nuclear spin in a room temperature solid*, Science **336**, 1283 to 1286 (2012)

With slight modifications Chapter 3 is in its entirety published in the main text and the supplementary information of

> G. Kucsko*, P. C. Maurer*, N. Yao, M. Kubo, H. J. Noh, P. Lo, H. Park, M. D. Lukin, *Nanometer scale thermometry in a living cell*, Nature **500**, 54 to 58 (2013)

All of Chapter 4 and part of Appendix C appeared in the main text and the supplementary information of the following publication

> P. C. Maurer*, J. R. Maze*, P. Stanwix*, L. Jiang, A. V. Gorshkov, A. A. Zibrov, B. Harke, J. S. Hodges, A. Yacoby, D. Twitchen, S. W. Hell, R. L. Walsworth, M. D. Lukin, *Far-field optical imaging and manipulation of individual spins with nanoscale resolution*, Nature Physics **6**, 912 to 918 (2010)

Appendix A appears in its entirety as

> L., Jiang*, J. S. Hodges*, J. R. Maze*, P. C. Maurer, J. M. Taylor, D. G. Cory, P. R. Hemmer, R. L. Walsworth, A. Yacoby, A. S. Zibrov, M. D. Lukin, *Repetitive readout of a single electronic spin via quantum logic with nuclear spin ancillae*, Science **326**, 267 to 272 (2009)

Appendix B appears completely in the main text and the supplementary information of

> N. Y. Yao*, L. Jiang*, A. V. Gorshkov*, P. C. Maurer, G. Giedke, J. I. Cirac, M. D. Lukin, *Scalable architecture for a room temperature solid-state quantum information processor*, Nature communications **3**, 800 (2012)

* These authors contributed equally to this work.

Acknowledgments

First of all, I would like to thank my advisor, Prof. Mikhail Lukin, for all the guidance and support that I have enjoyed during my six years of graduate education at Harvard University. I think one of the most valuable assets that I have learned from working with Misha is how to 'think out of the box' and follow original approaches that can often lead to powerful novel tools. Moreover, working for Misha has been very enriching in the sense that while being a theoretical physicists by training he had also a very solid experimental understanding and was comfortable in giving advice whenever needed. As a junior graduate student it was particularly satisfying to rely on the support of such an advisor that both could come up with very intriguing questions as well as could help with the specific implementation. While Misha provided a constant flow of great ideas he has also been very supportive when it came down to the realization of my own ideas. Specifically, at the end of my graduate studies Misha gave me full support to realize a nanoscale temperature sensing technique, for which I will always be thankful to him.

Second, I also would like to thank my longterm collaborator Prof. Ronald Walsworth. The work on super-resolution imaging, co-lead by Ron, was the first experiment that I carried out at Harvard. The scientific exchange with Ron and his group has always been very stimulating as their interest aligned well with my research. Another collaborator that I would like to acknowledge is Prof. Liang Jiang from Yale University and a former graduate student in the Lukin group. Although Liang was already in his final year at Harvard when I started graduate school we have co-worked on several projects.

Moreover, I would also like to thank Prof. Amir Yacoby and Prof. Markus Greiner for their academic advice and guidance and for volunteering as member on my thesis committee. In addition, I appreciate the stimulating scientific discussions that I had with both. For

the sub-diffractional imaging project it was particularly valuable to rely on Markus' extensive optics knowledge. On many other occasions Amir's background in condensed matter physics and his work on NV-based magnetic sensing proved to be pivotal.

Also much thanks goes to Prof. Jeronimo Maze and Georg Kucsko. When I joined the Lukin group Jero was a senior graduate student and pioneered much of the work on NV centers. In my first year we worked together on the realization of super-resolution imaging and manipulation of individual NV centers, when I learned a lot about experimental work in optics from him. I am happy that I could pass on this knowledge to Georg, a junior graduate student who continues my work on room temperature spin control. Together with Georg we implemented our NV based quantum memory as well as our nanoscale thermometer sensing technique. I specifically would like to acknowledge his persistency in perfecting lithographic processes required for microwave engineering. Finally I like to thank both for the great and cheerful time we had in the lab particularly when working long hours on our experiments.

Furthermore, I would also like to acknowledge Norman Yao, Prof. Liang Jiang and Prof. Alexey Gorshkov who led the work on a scalable NV based room temperature quantum computation architecture. It was a very enriching experience for me to collaborate with three such great theoretical physicists.

Finally I would like to thank all members of the Lukin group for many intriguing discussions and helpful hands on the experiments. Specifically I would like to point out the contributions of Joonhee Choi, Ruffin Evans, Alp Sipahigil, Shimon Kolkowitz, Michael Goldman, Nicholas Chisholm, Igor Lovchinsky, Brendan Shields, Jeff Thompson, Dr. Christian Latta, Dr. Steven Bennett, Dr. Alexander Zibrov (and his son), Dr. Jonathan Hodges, Dr.

Nathalie de Leon, Dr. Alexander Kubanek, Dr. Alexander Sushkov, Dr. Emre Togan, Dr. Tobias Tiecke and Dr. Yiwen Chu. As well as Stephen DeVience, Erik Bauch, Dr. Paul Stanwix, Dr. Linh Pham, Dr. Chinmay Belthangady, Dr. David Le Sage, Dr. David Glenn and Dr. Alexei Trifonov from the Walsworth group.

Also much thanks goes to my collaborators from outside of the Harvard physics department who crucially contributed to the success of these projects. Specifically this includes Dr. Benjamin Harke and Prof. Stefan Hell from the Max Planck Institute for Biophysics in Goettingen for their assistance in implementing our sub-diffraction imaging techniques. Also I am grateful to Dr. Fernando Pastawski, Dr. David Hunger, Dr. Geza Giedke and Prof. Ignacio Cirac from the Max Planck Institute for Quantum Optics in Garchingen for their contribution towards the second long quantum memory and the room temperature quantum computing architecture. Moreover my appreciation goes to Minako Kubo, Prof. Peggy Lo and Prof. Hongkun Park from the chemistry department at Harvard for preparing biological sample, which was crucial for the demonstration of the NV based temperature control in biological systems. And of course, I also like to acknowledge our industry collaborators from Element Six Dr. Matthew Markham and Dr. Daniel Twitchen who supplied us with high quality diamond samples that enabled most of the presented results. In addition I also like to thanks Prof. Fedor Jelezko from the University of Ulm and Prof. Junichi Isoya from University of Tsukuba, with whom we recently have started a collaboration to study many-body effects in an ensemble of strongly coupled NV spins.

I would also like to acknowledge the Fulbright Science and Technology Award, the Harvard Merit Fellowship, the Swiss National Science Foundation and the Harvard Purcell Fellowship for financial support, which I received during my graduate education. In addi-

tion I also like to thank my grandparents, Wilhelm and Elsa Maurer and Prof. Christian Menn for their generous support and encouragement.

Finally my deepest appreciation goes to my family Dr. Hyun Ji Noh and my parents Andreas and Claudia Maurer. Hyun Ji did not only understand when I relocated to advance my career but she also actively arrange her plans such that we can be together, which I will always remember. Moreover, I enjoyed the many scientific discussions we had especially the ones related to applications of novel physical techniques to study biological questions. It was discussions with her that ignited the start of our nanoscale temperature sensing experiment. Moreover, I would like to thank my parents for all their support during my education. Without their engagement I would never have been able to reach this academic point. It was my father who triggered my curiosity for physics and science in general and it was both my parents who supported and advised me from the start of elementary school until the end of graduate school. This thesis is dedicated to the three of you.

I am looking forward to many more years of fruitful scientific collaborations with all my former collaborators and specifically with my Ph.D. advisor Misha.

To my Family

Andreas & Claudia Maurer and Hyun Ji Noh

Chapter 1

Introduction

1.1 Background

The precise control of quantum systems lies at the heart of modern atomic physics. Over the last two decades it has become possible to control the quantum mechanical state of a variety of different systems with high fidelity [1]. These advances were honored by the 2012 Nobel Prize in physics awarded to Serge Haroche and David Wineland ”for their ground-breaking experimental methods that enable the measurement and manipulation of individual quantum systems” [2]. The ability to efficiently control quantum systems has far reaching applications ranging from the development of nanoscale sensors with unparalleled sensitivity to the test of fundamental properties of many-body systems.

1.1.1 Motivation

The first experiments that demonstrated coherent control over a quantum system based on microwave manipulation of the intrinsic hyperfine states in atomic gases. Norman Ram-

sey pioneered the development of interference techniques that enabled a spectroscopic measurement of these hyperfine transitions with unprecedented accuracy [3]. Soon, it was recognized that based on such precise interference measurements of atomic transitions novel clocks could be developed which would surpass the frequency standard set by quartz oscillators [4]. Over the last half-century, the accuracy of atomic clocks has continuously increased by a total of eight order of magnitudes. Today the most accurate atomic clocks are based upon optical rather than microwave transitions and achieve relative accuracies of 10^{-18} [5] with possible further improvements by utilizing squeezed states [6]. This example of frequency metrology illustrates how the precise control over a quantum system opens the door to metrological measurements many order of magnitudes superior to any known classical approach.

In the case of precision measurements, like atomic clocks, interactions between the system and the environment are undesirable as they limit the measurement accuracy, and hence much effort is taken to suppress these averse effects. A large variety of quantum systems are highly sensitive to local magnetic and/or electric fields or depend on temperature. Exactly these interactions with the environment can also be seen as a valuable resource for the characterization of the local environment with great accuracy. Being able to measure those quantities on the nanoscale would benefit many different areas of research ranging from nano-engineering to biomedical research. While one of the first applications of such a 'quantum sensing' approach relied upon Rubidium vapor cells to measure local magnetic fields by optical detection of a Zeeman shift, it is today possible to utilize a single electronic spin confined to a solid state system to sense magnetic fields with nanometer resolution [7]. Being able to detect fields at a nanoscale is of tremendous importance to

many fields and, for example, might enable nuclear spin resonance measurements on a single macro-biological molecule [8] or imaging of neuron activities in networks [9].

Being able to entangle quantum systems in a well controlled way not only offers the ability to increase the sensitivity for quantum metrology and sensing but also is a powerful resource for the study of complex correlated systems. Many-body systems are of particularly interest since many important condensed matter systems consist of a large number of interacting quantum mechanical particles. The dimensionality of these problems makes any classical simulation impractical since the Hilbert space scales exponentially with particle number. However, by using a quantum system for which the interaction properties of individual particles can be tailored to represent a Hamiltonian of interest, it might be possible to perform certain simulations that would otherwise not be accessible. The idea of such 'quantum simulations' was introduced by Richard Feynman and is now being actively pursued based on ultra cold atoms where systems of large particle numbers can be created routinely [10]. Experiments based on Bose gases of rubidium atoms in optical lattices [11] or ions in linear Paul traps [12] have recently enabled the study of phase transitions in a regime where the particle number is large enough to prevent classical simulations.

While interaction quantum systems open the door to quantum simulations they might also enable quantum computation which can considerably speed up certain algorithms [13]. In principle such a quantum computer can be realized if a large number of quantum bits (qubits) can be controlled via an universal set of quantum gates, can maintain sufficiently long coherence time and can be reliably initialized and readout [14]. Peter Shor discovered for example that a quantum computer can outperform its classical counterpart when decompositing a large number into its coprimes [13]. This is of particular interest since today's

public-key encryption algorithms like RSA are based on the assumption that large numbers can not be efficiently factorized. Today, several different systems are being investigated as a promising basis for the realization of a scalable quantum computer. Among others, trapped ions and superconducting qubits have rapidly developed as a promising scalable systems where simple quantum algorithms have been implemented [15, 16]. However one fundamental hurdle that any scalable quantum computer faces is the problem of dephasing during its operations.

While quantum computation in principle allows for the breaking of public encryption protocols, quantum communication provides a way for secure information transfer [17]. Specifically, two distant parties can securely communicate by transmitting information encoded in qubits, typically photons, rather than by exchanging classical information. This type of communication is provably secure since without knowing the encryption basis, a measurement of the qubits by a third partiy will inevitably leave a trace. However, the problem with this approach is that it is susceptible to loss of photon coherence in the transmission channel as attenuation can fundamentally not be distinguished from eavesdropping. Since attenuation scales with the distance of transmission this has hampered communication over long distances. Fortunately, this problem can be circumvented by employing an array of quantum repeaters along the transmission channel facilitating long distance communication [18]. One of the biggest problems related to the realization of quantum repeaters is the ability to interface optical qubits with a long-lived local memory qubit [17]. A variety of different systems are currently being developed to enable an interface between a local stationary qubit and an optical photon.

Although these are all fundamentally very different applications, their realizations re-

quire the ability to control individual quantum systems with high fidelity. This includes high fidelity initialization and readout as well as accurate coherent manipulation. Using quantum control on even simple non-interacting quantum systems already offers an intriguing array of applications in quantum metrology, sensing and encryption. While the ability to control more complicated interacting quantum systems enables an even wider range of applications, high fidelity control of individual qubits still remains a key challenge to many of these systems. Furthermore, preserving the coherence of quantum systems for extended periods of times is critical to all of the mentioned applications. Unfortunately, for many real world systems these two requirements turn frequently out to be orthogonal to each other. Therefore, depending on the application, certain systems are more suitable for some tasks while other system are more adequate for others.

1.1.2 Controlled quantum systems

Motivated by these applications over the last two decades, an array of different systems have been developed. Individual atoms are not only one of the oldest system but also resemble the most precisely controllable as well as the one with the longest coherence times. Here individual qubits are usually encoded in magneticaly insensitive hyperfine 'clock' states. This allows for an efficient decoupling of the qubit from perturbations in the environment and hence enables the observation of coherence times approaching minutes [19]. Atomic qubits can be coherently manipulated by driving an optical Raman transition enabling operations on sub-nanosecond time scales [20]. Moreover, it is possible, for a chain of ions cooled to the motional ground state, to deterministically entangle the spin state of individual ions by using the common center of mass mode. These interactions can be

precisely controlled by applying optical pulses to the ions enabling the realization of a controlled-phase gate with high fidelity [21, 22]. While optical techniques not only provide a tool for coherent manipulation of the spin state they also give access to efficient readout. Based on the presence of a strongly fluorescent near perfect cycling transition in the extended level scheme, the associated readout fidelities of the qubit spin state can be better than 99.99 % [23], approaching the regime required for quantum error correction. While ion traps exhibit unprecedented coherence times and hence can be extraordinary frequency standards, the ability to perform high fidelity two qubit operations also makes them an interesting candidate for quantum computation. Despite recent impressive developments in ion traps the realization of a scalable architecture has been hampered by the difficulty of addressing individual vibrational modes in systems with large ion numbers [24]. Nevertheless, in recent years approaches including segmented traps [25] or integration into optical networks [26] have emerged as potential way to bypass these hurdles.

As proposed by Loss and DiVincenzo [27], solid state systems based on artificial mesoscopic structures represent another compelling approach to quantum information technology. Specifically, quantum dots and more recently superconducting qubits have attracted much attention. These qubit types utilize artificial nanostructures lithographically patterned on semiconductor surfaces. For quantum dots, individual electrons are confined in space either via surface-gates or epitaxial growth with the qubit levels defined by the electronic spin state [28]. In the case of superconducting qubits the individual qubit states are either determined by the number of Cooper pairs on a superconducting island (charge qubit), the superconducting phase associated with a superconducting loop (phase qubit) or the flux through the loop (flux qubit) [29]. For all of these systems an intrinsic anharmonicity is

associated with the corresponding energy spectrum, for which the term artificial atoms has been coined. Since the size of most of these nanostructures is eventually limited by the resolution of nanofabrication, the relevant energy scales are usually on the order of μeV to meV, enabling manipulations in the microwave regime and requiring these systems to be cooled down to milli-Kelvin temperatures. One particular advantage of using condensed matter over atomic systems lies in the fact that trapping is not required. Moreover, the nanofabrication involved is highly efficient as it relies on techniques that were perfected over the last half-century for CMOS technology. These advances have rendered condensed matter systems a serious alternative to atomic systems in the quest for a scalable quantum computer. While solid state qubits are certainly an intriguing approach to quantum computation, they in general suffer from coherence times many order of magnitudes inferior to those of atomic systems.

While qubits based on individual atoms have intrinsically long coherence times the experimental effort of trapping and laser cooling is considerable. Moreover, cooling and controlling large numbers of ions in segmented Paul traps remains an outstanding challenge hampering the realization of a scalable quantum computer architecture. Likewise, solid state systems have limited coherence times owing to interaction with the nuclear spin bath in the case of quantum dots or defects induced during the fabrication of superconducting qubits. A novel system that approaches this problem from a different angle are crystallographic defects in highly purified single crystalline materials. These defects can behave very much like an atom trapped in a solid state system. Over the last decade a variety of defects with interesting spin properties in different materials have been identified. For many applications in quantum information, it is desirable to be able to address and

readout individual defects rather than an ensemble. In principle, there are two main routes towards the detection of individual spins: one relies on electrical and the other on optical measurements.

Phosphorus doped silicon (Si:P) is one particularly interesting defect that can be electronically readout when cooled down to cryogenic temperatures [30]. This defect is formed by a single phosphorus atom that substitutes a silicon atom in the host lattice and acts as a donor. In its neutral charge state Si:P posseses a spin of S=$1/2$, which can in the presence of a strong magnetic field be further Zeeman splitted. With the help of a nearby gate, spin-to-charge conversion can be achieved which then enables single shot readout of the spin state using an single electron transistor. This projective measurement process also efficiently initializes the electronic spin [30]. Moreover, by applying microwave pulses at well defined frequencies it is possible to coherently manipulate the electronic spin state. In isotopically pure Si the associated coherence times can be remarkably long, due to the absence of impurities. By encoding the qubit not in the electronic spin but rather the nuclear spin of the phosphorus, it is further possible to store quantum information for several seconds [31, 32]. One application that is currently being pursued makes use of an array of Si:P for quantum information processing analogue to the Loss and DiVincenzo architecture [33, 34].

1.2 Nitrogen vacancy centers in diamond

The nitrogen vacancy (NV) center is a crystallographic defect in diamond with intriguing spin properties. Unlike Si:P, NV centers are a good qubit even at room temperature that can be efficiently initialized and readout by optical techniques.

NV centers are a naturally occurring crystallographic point defect consisting of a substitutional nitrogen and a adjacent vacant lattice size (the crystallographic structure is shown in Fig. 1.1). The combined complex of a nitrogen and a vacancy to become a NV center is thermodynamically more stable than the two defects separately. While NV centers can occur naturally it is also possible to artificially create NV defects in the diamond host lattice by ion implantation. During this process the nitrogen ions collide with the diamond lattice and knock out carbon atoms leaving vacancies on the decelerating path. When annealing the implanted diamond above 800° C some of these vacancies will become mobile and combine with a substitutional nitrogen to form a more stable NV defect [35]. Unfortunately this type of implantation and annealing is a random process with only a modest yield. Recently an array of different approaches with varying success have been pursued to both increase conversion yield as well as to implant nitrogen defects with nanoscale resolution [36, 37, 38, 39].

The electronic structure of the NV center can be derived by considering a linear combination of the highest occupied molecular orbital. Since the nitrogen and the carbon atoms in diamond are all sp^3 hybridized, the relevant orbitals associated with the NV center consist of the lone pair associated with the substitutional nitrogen (σ_N) and the three dangling bonds ($\sigma_{1,2,3}$) pointing from the neighboring carbon atoms towards the vacancy. In a nearest neighbor tight binding model the individual energy levels of the NV orbitals are found by a

linear superposition. Under the absence of strain this hamiltonian has C_{3v} symmetry which tells us that two of the four resulting linear combined orbital energy levels are degenerate. The new molecular orbitals are then given by [40]

$$\begin{aligned} a_1^{(1)} :\ \varphi_1 &= \sqrt{1-\alpha^2}\sigma_N - \tfrac{\alpha}{\sqrt{3}}\left(\sigma_1+\sigma_2+\sigma_3\right) \\ a_1^{(2)} :\ \varphi_2 &= \alpha\sigma_N + \sqrt{\tfrac{1-\alpha^2}{3}}\left(\sigma_1+\sigma_2+\sigma_3\right) \\ e_x :\ \varphi_3 &= \tfrac{1}{\sqrt{6}}\left(2\sigma_1-\sigma_2-\sigma_3\right) \\ e_y :\ \varphi_4 &= \tfrac{1}{\sqrt{2}}\left(\sigma_2-\sigma_3\right), \end{aligned} \tag{1.1}$$

with $0 \leq \alpha \leq 1/2$. Because nitrogen has a larger electronegativity than carbon we can order the energy of the individual orbitals by $E_{a_1^{(1)}} \leq E_{a_1^{(2)}} \leq E_{e_x} = E_{e_y}$. In a more quantitative approach the energies of these orbital states can be obtained through ab-initio calculations [40]. From such calculations one finds that the lowest lying energy level is located within the valence band of diamond and the remaining levels are within the band gap as shown in Fig. 1.1b. The charge state of NV centers in bulk diamond is 70% of the time singly negatively charged and the remaining time neutral [41]. The spin configuration of the ground state of NV^- is found by filling the six electrons, three from the carbon dangling bounds, two from the nitrogen and one additional from the negative charge, into these orbital states. In the electronic ground state four of the six electrons fill the lowest two levels $a_1^{(1)}$ and $a_1^{(2)}$ and the remaining two electrons occupy the e_x and e_y orbitals. Since e_x and e_y are degenerate in energy Hund's rule can be applied resulting in a spin triplet ground state. An extensive and complete discussion of the different states associated with the NV center can be found in [40].

Under green illumination, the NV center can be excited from this ground to the electronic first excited state by moving one electron from $a_1^{(2)}$ to the $e_{x,y}$ orbital. The lifetime

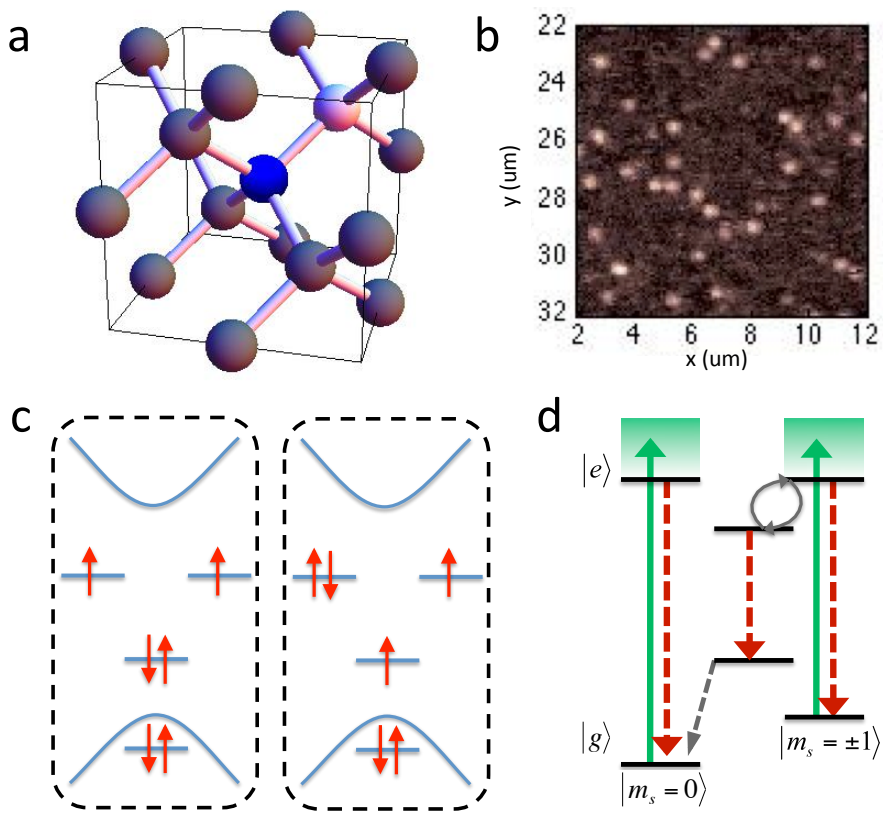

Figure 1.1: | **Nitrogen vacancy center in diamond. a,** Crystallographic structure of the NV center. Carbon atoms are represented in gray, nitrogen blue and the vacancy white spheres. **b,** Confocal image of bulk diamond, each fluorescent spot constitutes an individual NV center. **c,** Schematic representation of the energy level diagram for the NV orbitals in the electronic ground (left) and first excited (right) state. The blue parabolas represent the conducting and valence band and the red arrows represent the electrons. **d,** Simplified level diagram for the NV center with $|g\rangle$ ($|e\rangle$) denoting the electronic ground (excited) state. Green arrows represent optical driven transition and the red dashed arrows represent fluorescent transitions. The gray dashed arrow is a non-radiative transition from the long-lived ($1/\gamma = 300$ ns) metastable singlet state to $m_s = 0$ and the gray arrows in the excited state represent spin-orbit coupling mixing $m_s = \pm 1$ and a nearby singlet state.

of this electronic excited state is on the order of 12 ns and emits at wavelength greater than 637 nm. While this process mainly conserves the spin projection mixing of the excited state with a nearby singlet state induces coupling of the m_s=± 1 projection to a metastable singlet state [42]. Since the lifetime of this metastable singlet state is long, on the order of 300 ns, the fluorescence rate of the NV center in the m_s=± 1 manifold is reduced compared to rate in the m_s=0, enabling efficient optical spin detection. Finally this metastable singlet state predominantly decays into the m_s=0 state, allowing not only for fluorescent readout of the NV's spin state but also for efficient initialization by optical pumping.

In the ground state the spin triplet of the NV center has a magnetic anisotropy of the form ΔS_z^2, with $\Delta = (2\pi)\, 2.88\ GHz$. This zero-field splitting originates from a non-vanishing dipole-dipole interaction between the electronic spins in the $e_{x,y}$ orbital due to the absence of inversion symmetry in the NV's electron density. Applying an external magnetic field further lifts the degeneracy between m_s=± 1 and enables selective coherent manipulation between m_s=0 and m_s=$+1$ or -1. An example of such a coherently driven Rabi oscillations is shown in Fig. 1.2. Using large microwave fields, coherent manipulation with Rabi frequencies in the GHz regime can be achieved [43].

For exceptionally pure type IIa diamond, with paramagnetic impurity concentrations below parts per billion, the free induced decay of a Ramsey type experiment (see Fig. 1.2c) is limited by interaction with a bath of ^{13}C nuclear spins, which has a natural abundance of 1.1%. The noise created by the ^{13}C spin bath is non-Markovian and hence coherence can be restored by dynamical decoupling [44], as shown in Fig. 1.2d. This technique can extend the NV coherence time to a few milliseconds at room temperature, only limited by electron T_1 processes. Since the underlying mechanism of this depolarization is caused by phonon

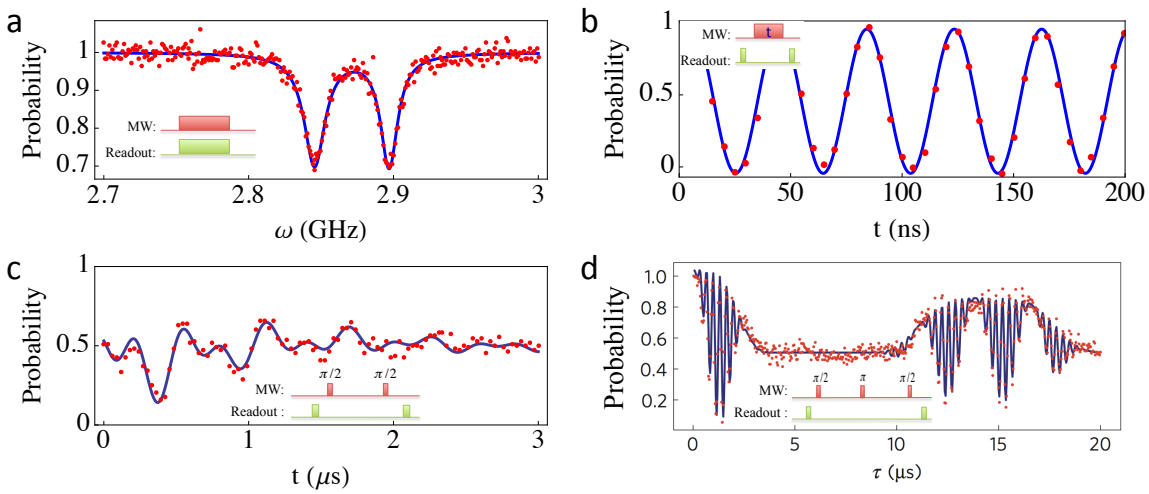

Figure 1.2: | **Coherent electron spin manipulation of a single NV center. a,** ESR Spectrum of a NV center in the presence of an external magnetic field. **b,** Microwave driven Rabi oscillations. **c,** Ramsey fringes consisting of three distinct frequencies originating from hyperfine interaction with the ^{14}N nuclear spin. **d,** The electronic coherence can be extended by using a refocusing π-pulse. Collapse and revival in the signal originate from interactions with a precessing ^{13}C nuclear spin bath. The fast oscillations stem from hyperfine interaction with the ^{15}N nuclear spin of the NV center (Figure **(d)** is taken from Fig, 4.3).

induced spin lattice relaxation, it is possible to further increase T_1 and T_2 by cooling of the diamond [45].

Motivated by these long room temperature coherence properties and the ability to optically initialize and readout the NV's spin state, several different intriguing applications in quantum information science and quantum metrology have been proposed. One possible application is the realization of a room temperature quantum information processor. Individual NV centers constitute different qubits that can interact with each other through magnetic dipole-dipole interaction of the electronic spin. In a proof-of-principle experiment a controlled-not gate has been demonstrated between two NVs with fidelities of 85% and separations of approximately 25 nm [46]. Higher fidelities could be possible by further decreasing NV-NV distance and increasing coherence times.

Another application that operates at cryogenic temperatures deploys NV centers as an interface between optical and solid state qubits for the realization of a quantum repeater [47]. Here first, the spins of two distanced NV centers are separately entangled with two identical photons. By performing a Bell-measurement on these two photons it is then possible to entangle the two distanced NV-centers with each other. Based on this scheme in recent experiments [48] it has been possible to entangle two NV centers separated on a macroscopic distance. While for these demonstrated experiments the bit rate is still at a impractically low level, it could be significantly improved by combining these experiments with cavity quantum electrodynamics [49, 50, 51].

Finally the ability to control and optically readout the spin state of a room temperature system opens an avenue for applications in quantum sensing. Specifically, recent experiments have used NV centers to sense the local magnetic field by using ESR to spectroscop-

ically determine the Zeeman splitting. Since the magnetic dipole moment falls off with the third power of the distance, having a nanoscale magnetic field sensor is of particular interest when probing small detection volumes (e.g. single spins) [52]. Moreover, a scanning sensor can be realized by using NV centers in nanodiamonds or artificial nanostructures [53]. This approach has recently allowed for the measurement of individual electronic spins and ensembles of nuclear spins [54, 55, 56, 57, 58].

1.3 Overview of the thesis

This thesis discusses quantum control of NV centers for applications in quantum information science and quantum metrology. Particularly, we borrow a variety of tools from atomic physics to coherently manipulate the NV spin, to realize an extraordinary room temperature quantum memory, a nanoscale temperature sensor as well as super-reslolution spin imaging and control.

1.3.1 Room-temperature quantum bit memory exceeding one second

Even though NV centers maintain extraordinarily long coherence times at room temperature, they are short on macroscopic time scales. In Chapter 2 of this thesis a novel technique is introduced that allows for a three orders of magnitude increase in storage time to beyond one second. In this technique, the NV is utilized as a quantum register composed of the electronic spin as a control qubit and a nearby weakly coupled ^{13}C nuclear spin as the memory qubit. The NV's electronic spin is then used to initialize and read out the nuclear memory qubit. However, the coupling between the electronic and nuclear spin also induces

decoherence of the memory qubit. In our approach this is avoided by subjecting the NV center to a controlled dissipative optical field that effectively decouples the control qubit from the memory qubit during the storage process. Utilizing a homonuclear RF decoupling sequence interactions between the memory nuclear spin and the ^{13}C spin in the host lattice are eliminated. This promotes NV centers as a unique room temperature quantum register with coherence times comparable to those of trapped ions, but without their experimental complexity.

1.3.2 Nanometer scale thermometry in a living cell

Chapter 3 makes use of coherent control of the NV spin for novel applications in nanoscale sensing, which enable the mapping of temperature profiles with unprecedented accuracy and sub-micrometer spatial resolution. The high sensitivity of our temperature sensing approach is based upon an accurate measurement of the temperature dependent zero-field splitting of NV centers. Using dynamical decoupling it is possible to probe the zero-field splitting with maximal accuracy enabling a temperature sensitivity of $10\text{mK}/\sqrt{\text{Hz}}$. Finally, injecting nanodiamonds that contain NV centers into living biological cells combined with local laser-induced heating we accurately control the temperature profile on sub-cellular length scales. This enables a wide variety of applications ranging from the engineering of nanoscale chemical reactions and the measurement of heat dissipation in electronic circuits to the study of temperature dependent biological processes and the cell selective treatment of diseases.

1.3.3 Far-field optical imaging and manipulation of individual spins with nanoscale resolution

Optical initialization and read-out of the spin state of individual NV centers is key for many applications in quantum sensing and quantum information processing. While these optical techniques are very powerful, they carry the distinct disadvantage of having the resolution limited by diffraction. Yet, for many applications particularly in the field of biological sciences a variety of relevant processes occur on length scales of the order of a few tens of nanometers. In Chapter 4 a novel approach relying on optical far-field techniques is introduced. This approach towards sub-diffraction imaging is based on the non-linear saturation properties of NV centers in combination with a Laguerre-Gaussian mode and enables a one order of magnitude improvement in resolution compared to the diffraction limit. Moreover by combining this sub-diffraction technique with a 'quantum Zeno' like effect it is further possible to selectively manipulate an individual NV in an ensemble of identical indistinguishable spins.

Chapter 2

Room-Temperature Quantum Bit Memory Exceeding One Second

2.1 Introduction

Stable quantum bits, capable of both storing quantum information for macroscopic timescales and of integration inside small, portable devices, represent an essential building block for an array of potential applications. Many technological driven implementations of quantum communication [59] and quantum computation [1] rely upon the ability to maintain an arbitrary coherent superposition of a quantum bit (qubit) for an extended period of time. Furthermore, integrating such quantum mechanical systems in compact, mobile devices remains an outstanding experimental task.

While trapped ions and atoms [19] can exhibit coherence times as long as minutes, they typically require a complex infrastructure involving laser-cooling and ultra-high vacuum. Other systems, most notably ensembles of electronic and nuclear spins, have also

achieved long coherence times in bulk ESR and NMR experiments [60, 61, 62]; however, owing to their exceptional isolation, individual preparation, addressing and high fidelity measurement remains challenging, even at cryogenic temperatures [30].

In this chapter, we discuss the demonstration of a high fidelity readout of a solid-state qubit, which preserves its polarization for several minutes and features coherence lifetimes exceeding one second at room temperature. The qubit consists of a single ^{13}C nuclear spin in the vicinity of a Nitrogen-Vacancy (NV) color center within an isotopically purified diamond crystal. The long qubit memory time is achieved via a novel technique involving dissipative decoupling of the single nuclear spin from its local environment. The versatility, robustness and potential scalability of this system may allow for new applications in quantum information science.

2.2 NV Based quantum register

One approach towards the realization of a long lived quantum memory bases upon NV centers as individual quantum registers that consist of a control and a memory qubit. Here the electronic spin (control qubit) associated with the NV center is used to control one or several nearby nuclear spins (memory qubit) that are coupled to the electronic spin via hyperfine interaction. In principle, for an NV center the coherence time of such a nuclear spin, due to its small gyromagnetic ratio, can exceed the coherence time of the electron spin. Using this approach NV quantum registers have been demonstrated to maintain coherence times on the order of several milliseconds in room-temperature diamond.

For readout of the nuclear spin the electronic spin is entangled with the nuclear spin via a controlled not-gate (C_nNOT_e), mediated by hyperfine interaction. By a subsequent fluo-

rescence measurement of the electronic spin state the nuclear spin is then determined [63, 64, 65]. However, in general each measurement of the electronic spin also slightly depolarizes the nearby nuclear spin [66]. This effect limits the number of photons that can be scattered and therefore sets a bound to the readout fidelity. Nevertheless it has been possible to suppress this depolarization by subjecting the NV center to a large magnetic field [65], which enables single shot readout of the nuclear spin with repetitive readout [67].

Furthermore, full coherent control over the nuclear spin state can be achieved by either directly employing radio frequency (RF) pulses [68, 65] or indirectly controlling the nuclear Larmor precession via precise microwave induced manipulations of the electronic spin [63].

In contrast our approach is based upon an individual weakly coupled ^{13}C nuclear spin in a room-temperature diamond. Using a combination of laser illumination and RF decoupling pulse sequences [60, 69] enables the extension of our qubit memory lifetime by nearly three orders of magnitude. This approach decouples the nuclear qubit from both the nearby electronic spin and other nuclear spins, demonstrating that dissipative decoupling can be a robust and effective tool for protecting coherence in various quantum information systems [1, 70, 71].

Our experiments utilize an individual NV center and a single ^{13}C ($I = 1/2$) nuclear spin (Fig. 2.1a) in a diamond crystal. We work with an isotopically pure diamond sample, grown using Chemical Vapor Deposition from isotopically enriched carbon consisting of 99.99% spinless ^{12}C isotope. In such a sample, the optically detected electron spin resonance (ESR) associated with a single NV center is only weakly perturbed by ^{13}C nuclear spins, resulting in long electronic spin coherence times [72]. This allows us to make use of a Ramsey pulse

sequence to detect a weakly coupled single nuclear spin, separated from the NV by 1-2 nanometers. The coupling strength at such a distance is sufficient to prepare and measure the nuclear spin qubit with high fidelity. For the present concentration of ^{13}C nuclei, about 10% of all NV centers exhibit a coupled nuclear spin with a separation of this order.

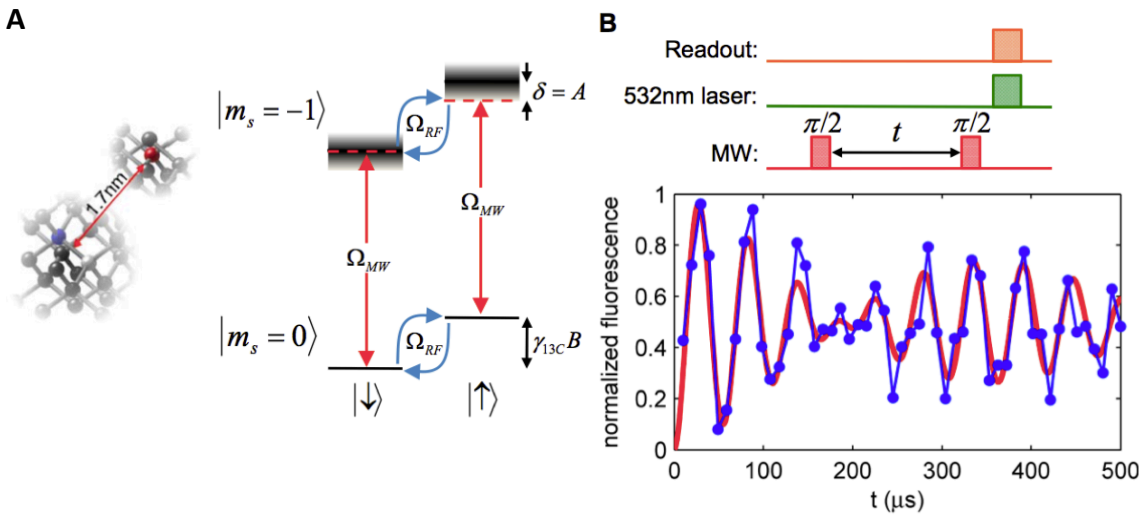

Figure 2.1: | **Experimental System. a,** The NV center with a proximal ^{13}C spin can be modeled as a simple four-level system to understand readout dynamics. Nuclear spin sublevels $|\uparrow\rangle$ and $|\downarrow\rangle$ are split by a Zeeman shift ($\gamma_{13C}B$) and addressed via RF radiation with Rabi frequency Ω_{RF}. The electronic transition $|0\rangle \rightarrow |-1\rangle$ (red arrows) can be simultaneously driven by a microwave field with relative detuning given by the hyperfine coupling strength, $A = \sqrt{A_{\parallel}^2 + A_{\perp}^2}$. **b,** An electron Ramsey measurement as a function of free evolution time (t), depicts beating due to the different hyperfine transitions and a $T_{2e}^* = (470 \pm 100)\ \mu$s.

In our experimental setup, the diamond sample is magnetically shielded from external perturbations, and a static magnetic field $B = (244.42 \pm 0.02)$ G is applied along the NV symmetry axis. The spin transition between the $|0\rangle \rightarrow |-1\rangle$ electronic spin states is addressed via microwave radiation. Figure 2.1b shows the free electron precession of an individual NV center, measured via a Ramsey sequence. The signal dephases on a time

scale of $T_{2e}^{*} = (470 \pm 100)\mu s$ consistent with the given isotopic purity of the sample [72]. The characteristic collapses and revivals of the Ramsey signal correspond to the signature of a single weakly coupled ^{13}C nuclear spin. This coupling strength, originating from a hyperfine interaction, corresponds to an electron-nuclear separation of roughly 1.7 nm (see Appendix C.1.1).

To confirm that the signal originates from a ^{13}C nuclear spin, we measure the probability of a RF-induced nuclear spin-flip as a function of carrier frequency, ω. As described below, we prepare the nuclear spin in either the $|\downarrow\rangle$ or $|\uparrow\rangle$-state by performing a projective measurement. After preparation of the nuclear spin via projection a 1.25 ms Gaussian shaped RF π-pulse is applied. A second step of nuclear measurement then allows us the nuclear spin-flip to be determined. Figure 2.2 shows that this probability is characterized by three resonances located at $\omega/(2\pi) = 258.86, 261.52, 264.18$ kHz, corresponding to the NV electronic spin being in $m_s = 1, 0, -1$ respectively; this indicates a projected hyperfine interaction, $A_{\parallel} = (2\pi)\,(2.66 \pm 0.08)$ kHz.

2.3 Single shoot readout of single nuclear spin

An important facet of quantum control involves the ability to perform high fidelity initialization and readout. One way to achieve single shot detection of the nuclear spin state relays on repetitive readout. In this approach (Fig. 2.3a) the electronic spin is first polarized into the $|0\rangle$ state. Next, a $\mathrm{C}_n\mathrm{NOT}_e$ logic gate (electronic spin-flip conditioned on the nuclear spin) is performed and the resulting state of the electronic spin is optically detected; this sequence is repeated multiple times to improve the readout fidelity. The required quantum logic is achieved via a Ramsey sequence on the electronic spin, where

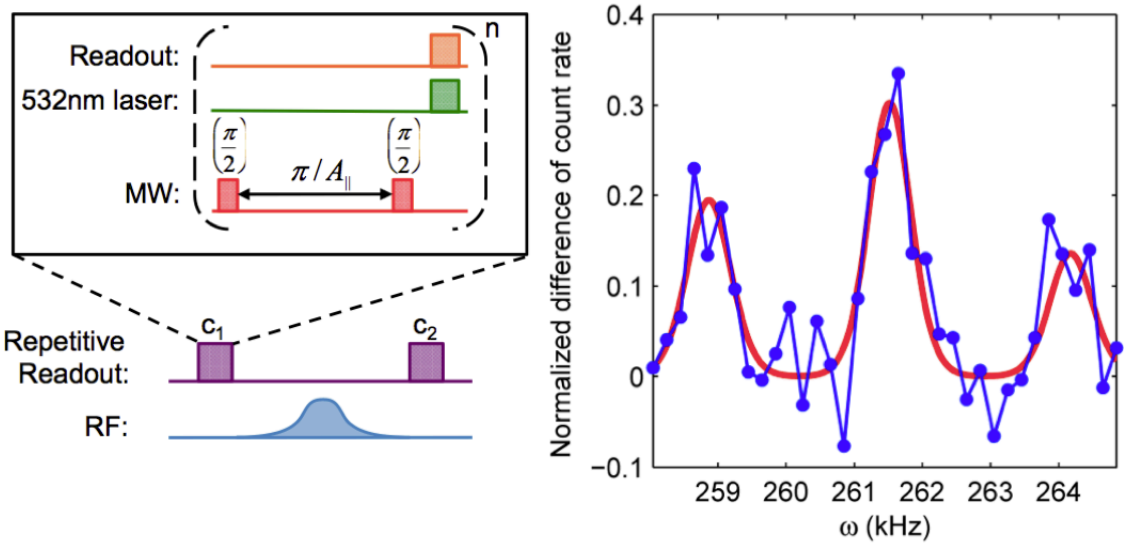

Figure 2.2: | **Sensing of a weakly coupled nuclear spin.** NMR spectra of ^{13}C, obtained via the depicted pulse sequence, demonstrate three different nuclear transitions corresponding to electronic spin states $m_s = 0, \pm 1$. The pulse sequence contains a Gaussian RF pulse (blue) and two repetitive readouts (purple), c_1 and c_2.

the free precession time is chosen to be $\tau = \pi/A_{\parallel}$. Fig. 2.3b depicts an example trace of the accumulated fluorescence of 20000 readout repetitions per data point. The resulting signal clearly switches between two distinct values, which correspond to the two states of the spin-$\frac{1}{2}$ ^{13}C nuclear spin. We associate high (low) count rates with the $|\uparrow(\downarrow)\rangle$ states of the nuclear spin, noting that these do not necessarily correspond to alignment/anti-alignment with the external field. This time trace indicates that the nuclear spin preserves its orientation, on average, for about half a minute.

To achieve high fidelity initialization of the nuclear spin, we post-select repetitive readout measurements that are below (above) a threshold corresponding to $147\,(195)$ counts per 2.2 s. This allows us to prepare the nuclear spin state with > 97 % fidelity. After successful initialization via projection, a second repetitive readout measurement is performed. This

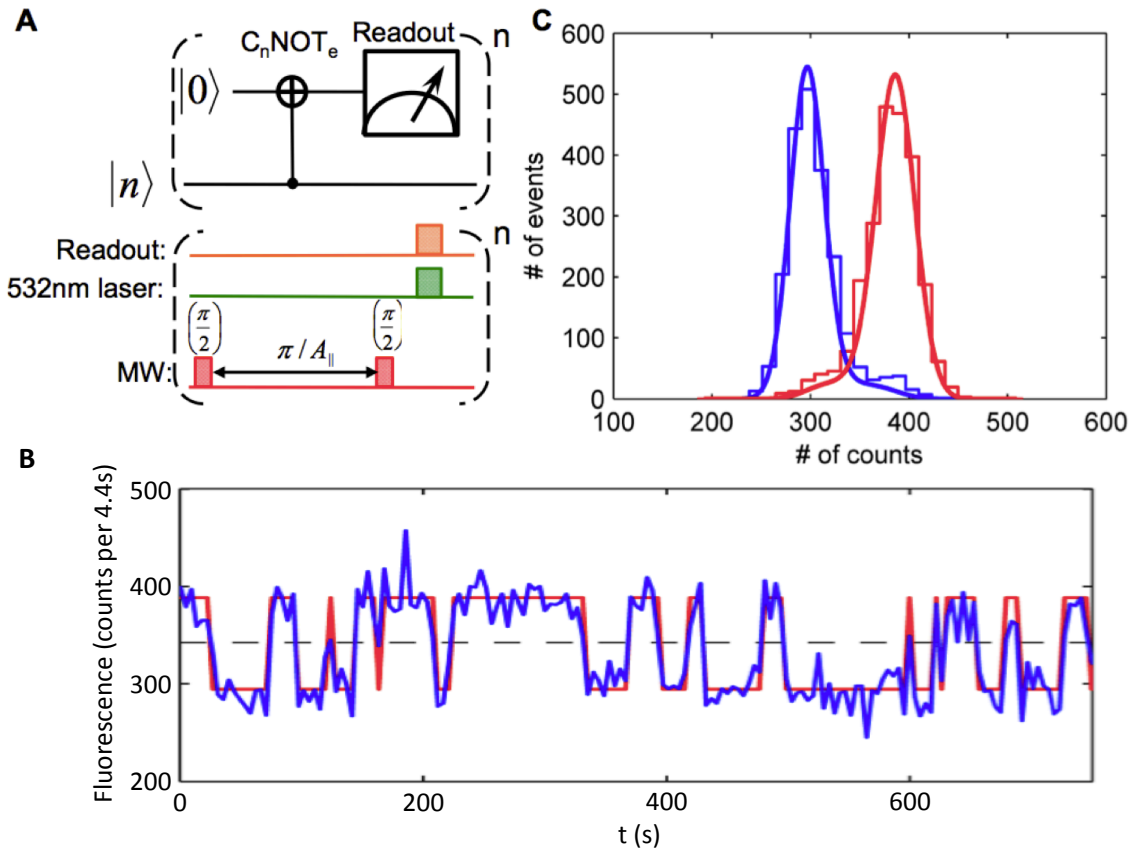

Figure 2.3: | **Qubit readout. a,** Circuit diagram of repetitive readout of the nuclear spin $|n\rangle$. The readout uses a C_nNOT_e gate consisting of multiple repetitions of an electronic spin Ramsey and subsequent repolarization. **b,** Fluorescence time trace showing single shot readout of the nuclear spin and corresponding quantum jumps. The integration time for a single point is 4.4 s. **c,** Histogram of continuous repetitive readouts (per 4.4 s) showing two overlapping distributions of nuclear spin states: $|\downarrow\rangle$ (blue) and $|\uparrow\rangle$ (red) (see Appendix C).

allows us to extract readout count statistics dependent on the nuclear spin state. As shown in Fig. 2.3c, the two distributions for the count rates of $|\uparrow\rangle$ and $|\downarrow\rangle$ are clearly resolved and their medians match the high and low levels of the fluorescence trace in Fig. 2.3b. From the overlap between the two distributions, we obtain a projective readout fidelity of $(91.9 \pm 2.5)\ \%$ [73].

2.4 Laser induced motional averaging rate

The long spin orientation lifetime, extracted from Fig. 2.3b, implies that our ^{13}C nuclear spin is an exceptionally robust degree of freedom. To quantify the nuclear depolarization rate, the T_{1n} time was measured as a function of laser intensity. When illuminated with a weak optical field, T_{1n} drops to (1.7 ± 0.5) s and increases linearly for higher laser intensities (Fig. 2.4d), which is consistent with predictions from a spin-fluctuator model [67, 66].

The spin-fluctuator model consists of the nuclear spin and the NV's electronic spin (fluctuator). The nuclear spin evolves coherently while the fluctuator undergoes incoherent stochastic transitions between different levels. Such evolution of the fluctuator induces then depolarization and decoherence of the nuclear spin.

The Hamiltonian associated with the nuclear spin is

$$H_n = (\gamma_{^{13}C} B)\hat{I}_z + \sum_{\alpha,\beta=x,y,z} A_{\alpha,\beta}\hat{S}_\alpha \hat{I}_\beta, \tag{2.1}$$

which consists of the Zeeman splitting due to an external magnetic field ($\gamma_{^{13}C} B$) and dipole interaction with the electronic spin ($A_{\alpha,\beta}$). In this simple model we assume that under strong green illumination the electronic spin fluctuates between the states $m_s = \pm\frac{1}{2}$. Ap-

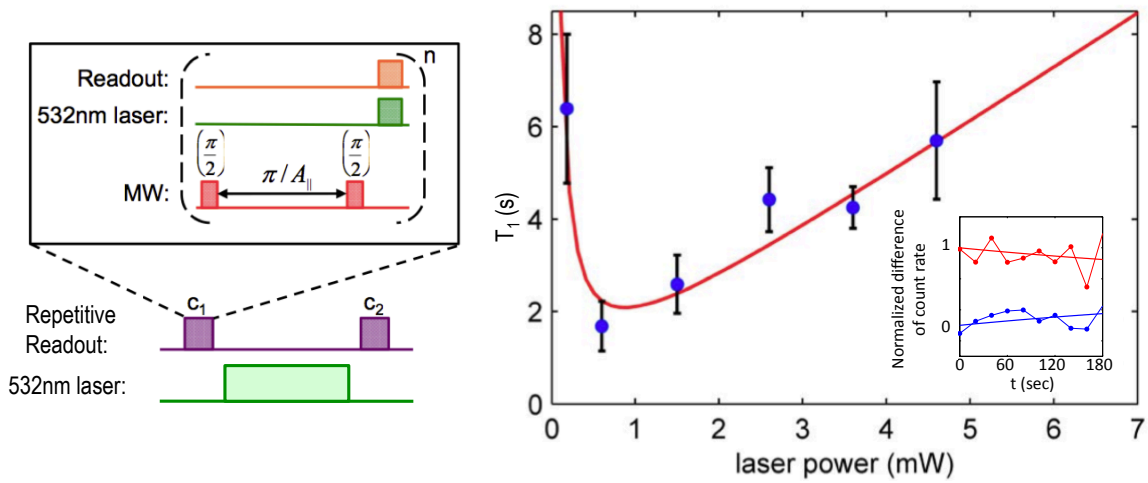

Figure 2.4: | **Nuclear depolarization rate.** Nuclear spin orientation lifetime, T_{1n} (error bars are one standard deviation), as a function of laser power in the presence of illumination by a 532 nm laser. As schematically shown on the left, each data point is extracted from a series of two repetitive readout sequences. The solid red curve represents the theoretical prediction from the simple model of nuclear depolarization induced by the off-axis dipolar hyperfine field. The inset shows the polarization as function of time measured in the dark.

proximating this effective Hamiltonian as $H_n = (\gamma_{^{13}C}B)\hat{I}_z + f(t)\sum_{\beta=x,y,z} A_{z,\beta}\hat{I}_\beta$, where we replaced $\hat{S}_z$ by the time-dependent stochastic variable $f(t) = \{-\frac{1}{2}, \frac{1}{2}\}$ described by a Bernoulli process and neglected other terms associated with $\hat{S}_x$ and $\hat{S}_y$. For simplicity, we assume that $\langle f(t)\rangle = 0$. The correlation function is then $\langle f(t)f(0)\rangle = \langle f^2(0)\rangle\, e^{-2\gamma|t|} = \frac{1}{4}e^{-2\gamma|t|}$, where γ is the forward/backward effective transition rate proportional to the laser intensity.

The Hamiltonian can be rewritten as $H_n = (\gamma_{^{13}C}B)\hat{I}_z + f(t)(A_{z,z|}\hat{I}_z + A_{z+}\hat{I}_+ + A_{z-}\hat{I}_-)$ with $\hat{I}_\pm = (I_x \pm iI_y)$ and $A_{z,\pm}\left(= A^*_{z,\mp}\right) = (A_{z,x} \mp iA_{z,y})/2$. We can estimate the nuclear spin depolarization rate induced by the terms $f(t)(A_{z,+}\hat{I}_+ + A_{z,-}\hat{I}_-)$. Noting that $|A_{z,+}| = |A_{z,-}| \equiv: A_\perp/2$, the noise can be re-express as, $A_\perp f(t)I_x$. First order time-dependent perturbation theory yields the transition rates in the two directions as:

$\Gamma_\uparrow = \left(\frac{A_\perp}{2}\right)^2 S_q(-\gamma_{^{13}C}B)$ and $\Gamma_\downarrow = \left(\frac{A_\perp}{2}\right)^2 S_q(\gamma_{^{13}C}B)$ where $S_q(\omega)$ is the noise spectral density. Assuming classical telegraph noise, the spectral density is given by $S_q(\omega) = \frac{\gamma/4}{\left(\gamma_{^{13}C}B/2\right)^2+\gamma^2}$, yielding a depolarization rate,

$$1/T_{1n} = \Gamma_\uparrow + \Gamma_\downarrow = \frac{A_\perp^2}{8}\frac{\gamma}{\left(\gamma_{^{13}C}B/2\right)^2+\gamma^2}. \tag{2.2}$$

Figure 2.4 demonstrates that this model is in excellent agreement with the data.

However, without laser excitation, the nuclear spin lifetime is no longer limited by optically induced depolarization given in (eq. 2.2). Instead, in this regime, the dominant contribution to T_{1n} is expected to be coherent dipole-dipole interactions, $H_{dd} = D_{dd}\left(3(\mathbf{I}\cdot\mathbf{n})(\mathbf{I}'\cdot\mathbf{n}) - \mathbf{I}\cdot\mathbf{I}'\right)$ between the memory spin $\mathbf{I}$ and neighboring ^{13}C nuclear spins $\mathbf{I}'$. In our present experiment D_{dd} is on the order of 1 Hz. However, when the dephasing rate of the nuclear spin is much large than that of coherent interactions (D_{dd}), spin-flips are suppressed. In this case, commonly denoted as the quantum-Zeno effect [74], the nuclear polarization, $n_\uparrow$, is characterized by an exponential decay as a function of time,

$$n_\uparrow(t) = \frac{1}{2}\left(1 + \exp\left(-\frac{(D_{dd}/(2\pi))^2}{1/T_{1e}}t\right)\right). \tag{2.3}$$

The measurement in the inset in Fig. 2.4 depicts the nuclear spin dependent fluorescence rate as a function of waiting time t between initialization and readout. The data indicate that for $t < 3$ min no noticeable decay in the nuclear spin polarization is evinced.

2.5 Photon counting statistics and readout fidelity

To understand the statistics of the detected photons during the repetitive readout of the nuclear spin for a certain integration time we derive an analytical expression for the

photon's distribution that is fitted in Fig. 2.3c. We then analyze the readout and initialization fidelity derived from these distributions.

We start by first pointing out that the probability $p^{(n)}$ for n quantum jumps during the integration window τ is Poissonian-distributed with $p^{(n)} = \frac{\lambda^n}{n!} \exp(-\lambda)$, where $\lambda = \tau/T_{1n}$ and $1/T_{1n}$ is the nuclear depolarization rate. For an integration time of $\tau = 4.4$ s (Fig. 2.3c and Fig. 2.5a) and a nuclear spin flip time $T_{1n} = 25$ s, the probability for undergoing no quantum jump during readout is $p^{(0)} = 83.8\%$. The probability for one quantum jump is $p^{(1)} = 14.8\%$ and $p^{(n>1)} = 1\%$ for more than one jump. This allows us to restrict the discussion to the case where either zero or one quantum jump takes place during the readout time.

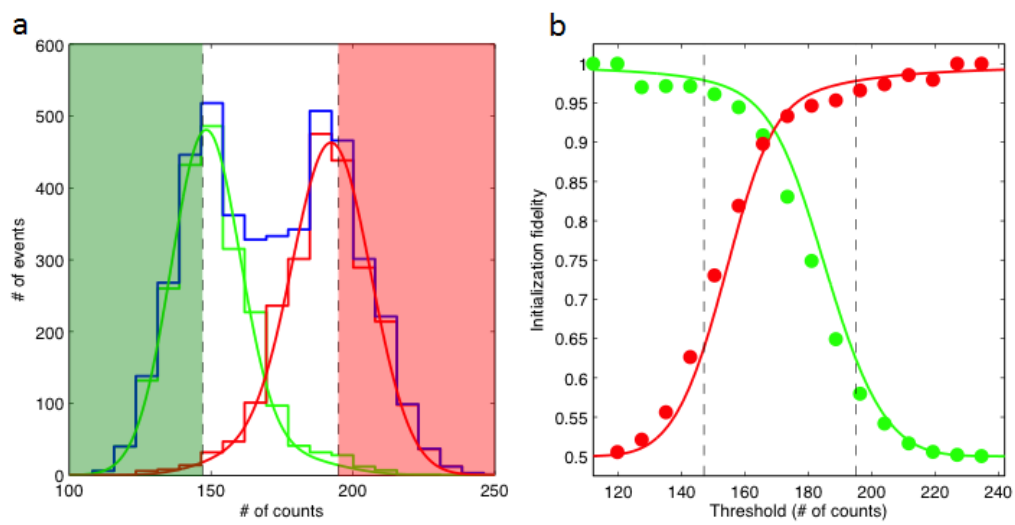

Figure 2.5: | **Photon count statistics and initialization fidelity.** **a,** Shows the photon counting statistics after initialization of the nuclear spin to $|\downarrow\rangle$ (green) and $|\uparrow\rangle$ (red). The histograms are measured data and the solid lines are theory fit. The blue histogram is the total distribution. The green(red) area indicates count rates for which the nuclear spin is initialized in $|\downarrow(\uparrow)\rangle$. **b,** shows the initialization fidelity of the nuclear spin in $|\downarrow(\uparrow)\rangle$ green(red) as function of threshold. The points are extracted from the histogram in a, the lines are preparation fidelity extracted from the fits in a.

For the case of no quantum jump during the readout τ, the photon count statistics $\alpha_s^{(0)}$ is Gaussian:

$$\alpha_s^{(0)}(x) = \frac{1}{\sqrt{2\pi\mu_s}} \exp\left(-\frac{(x-\mu_s)^2}{2\mu_s}\right), \tag{2.4}$$

where μ_s is the average photon count rate for the nuclear spin in the $|s =\downarrow (\uparrow)\rangle$ state and x is the number of detected photons. For shot-noise limited detection, we take the standard deviation $\sigma_s = \sqrt{\mu_s}$.

In the case of a single quantum jump event, the number of detected photons $\alpha_s^{(1)}$ will no longer be Gaussian distributed. We note that conditioned on one quantum jump occurring during the readout interval τ, the time spent in $|s\rangle$ will be uniformly distributed. Hence the number of counted photons is given by $\mu \sim \mu_\downarrow + (\mu_\uparrow - \mu_\downarrow)$Unif, where Unif denotes the uniform distribution on the interval $(0, 1)$. Taking into account the photon shot noise, we find the statistics of detected photons conditional on a single nuclear spin flip:

$$\begin{aligned}\alpha^{(1)}(x) &= \frac{1}{\mu_\uparrow - \mu_\downarrow} \int_{\mu_\downarrow}^{\mu_\uparrow} d\mu \frac{1}{\sqrt{2\pi\mu}} \exp\left(-\frac{(x-\mu)^2}{2\mu}\right) \\ &\approx \frac{1}{2(\mu_\uparrow - \mu_\downarrow)} \left(\text{Erf}\left(\frac{\mu_\downarrow - x}{\sqrt{2\mu_\downarrow}}\right) - \text{Erf}\left(\frac{\mu_\uparrow - x}{\sqrt{2\mu_\uparrow}}\right)\right),\end{aligned} \tag{2.5}$$

which is independent of the initial nuclear spin state $|s\rangle$.

Combing (eq. 2.4), (2.5) we can find an analytical expression for the photon counting statistics:

$$\alpha_s(x) \approx p^{(0)}\alpha_s^{(0)}(x) + p^{(1)}\alpha^{(1)}(x). \tag{2.6}$$

In Fig. 2.5c we fit this function to the recorded photon counting statistics with $\mu_{\downarrow(\uparrow)}$ being fit parameters. The measured data is in excellent agreement with our model of Fig. 2.5c and Fig. 2.5a.

As discussed we define the readout fidelity $\eta_{\downarrow}(n_{thr})$ by the probability of being in nuclear spin $|\downarrow\rangle$ conditional on detecting a photon number smaller than a threshold n_{thr}. The readout fidelity $\eta_{\downarrow}(n_{thr})$ is then given by

$$\eta_{\downarrow}(n_{thr}) = \frac{P_{\downarrow}(n_{thr})}{P_{\downarrow}(n_{thr}) + P_{\uparrow}(n_{thr})}, \tag{2.7}$$

where $P_{\downarrow(\uparrow)}(n_{thr}) = \int_0^{n_{thr}} \alpha_{\downarrow(\uparrow)}(x)dx$ is the probability that for nuclear spin $\downarrow$ $(\uparrow)$ the number of detected photons is below n_{thr}, and vice versa for $\eta_{\uparrow}(n_{thr})$. The optimal readout fidelity η is achieved for the threshold n_{thr} such that $\eta_{\downarrow(\uparrow)}$ is maximized.

Experimentally we determine η by initializing the nuclear spin in a known state $\downarrow$ $(\uparrow)$ and consecutively reading it out with our single shot measurement. The readout (20,000 repetitions) allows us then to determine the photon counting distribution depending on the initial state and hence the fidelity η.

However, this approach relies on the ability to initialize the nuclear spin to a well known state with high fidelity. One possible approach to realize high fiedelity initialization of the nuclear spin bases on repetitive readout of the spin state. If the recorded counts are smaller than a threshold $n_{thr}^{\downarrow}$ we assign the nuclear spin to $|\downarrow\rangle$ if they are larger than $n_{thr}^{\uparrow}$ we assign $|\uparrow\rangle$. In principle this allows for initialization with fidelity well above 99 $\%$ at the cost of efficiency. In Fig. 2.5b we plot the initialization fidelity as a function of the threshold $n_{thr}^{\downarrow}$ and $n_{thr}^{\uparrow}$. For a threshold of $147(195)$ counts we can initialize the nuclear spin state with a fidelity of $\approx 97\%$.

2.6 Second long coherence time

To probe the qubit's coherence time, our nuclear spin is again prepared via a projective measurement, after which, an NMR Ramsey pulse sequence is applied. The final state of the nuclear spin is then detected via repetitive readout. The results (Fig. 2.6b) demonstrate that, in the dark, the nuclear coherence time T_{2n}^* is limited to about (8.2 ± 1.3) ms. The origin of this relatively fast dephasing time can be understood by noting its direct correspondence with the population lifetime of the electronic spin $T_{1e} = (7.5 \pm 0.8)$ ms (blue curve Fig. 2.6b) [68]. Because the electron-nuclear coupling $A_{\|}$ exceeds $1/T_{1e}$, a single (random) flip of the electronic spin (from $|0\rangle$ to $|\pm 1\rangle$) is sufficient to dephase the nuclear spin.

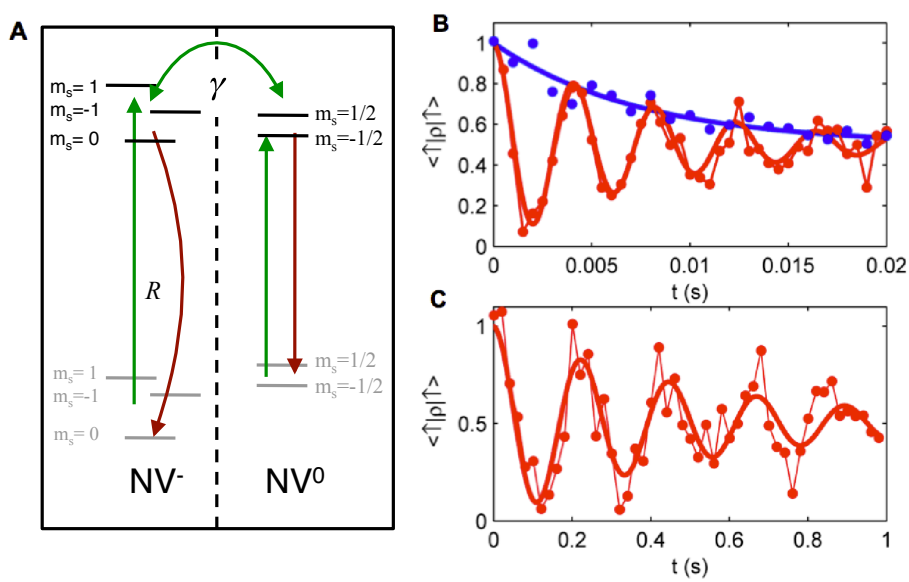

Figure 2.6: | **Nuclear spin coherence, motional averaging. a,** Model for repolarization and ionization dynamics. In the NV$^-$ charge state, the electronic spin can be pumped via green illumination to $m_s = 0$ at a rate R. **b,** Nuclear Ramsey experiment (red curve) depicting a dephasing time $T_{2n}^* = (8.2 \pm 1.3)$ ms. The origin of this dephasing is the depolarization of the electronic spin (blue curve), with $T_{1e} = (7.5 \pm 0.8)$ ms. **c,** Nuclear Ramsey experiment under concurrent green illumination, showing $T_{2n}^* = (0.53 \pm 0.14)$ s.

To extend the nuclear memory time, we must effectively decouple the electronic and nuclear spin during the storage interval. This is achieved by subjecting the electronic spin to controlled dissipation. Specifically, the NV center is excited by a focused green laser beam, resulting in optical pumping of the NV center out of the magnetic states ($|\pm 1\rangle$). In addition, the NV center also undergoes rapid ionization and deionization at a rate γ, proportional to the laser intensity. When these transition rates exceed the hyperfine coupling strength, the interaction between the nuclear and electronic spin is strongly suppressed owing to a phenomenon analogous to motional averaging [66].

Using this decoupling scheme, we show in Fig. 2.6c that the nuclear coherence time can be enhanced by simply applying green laser light; in particular, 10 mW of green laser excitation, yield an extended nuclear coherence time of $T_{2n}^{*} = (0.53 \pm 0.14)$ s. An improvement of T_{2n}^{*} by almost two orders of magnitude compared with measurements in the dark. The dependence of T_{2n}^{*} on green laser intensity shows a linear increase for low intensities and saturates around one second (Fig. 2.7d).

The effect of optical excitation on to the nuclear coherence time can be understood by a similar fluctuator model as discussed in Section 2.4. To estimate the nuclear spin dephasing rate only the term $A_{z,z}(t)\,\hat{I}_z$ of the Hamiltonian (eq. 2.1) is relevant. For time T, the random phase accumulated by the nuclear spin is given by $\Phi_{FID} = \int_0^T A_{z,z}(t)\,dt$. Assuming Gaussian noise we can compute the expectation value of the nuclear coherence, we have

$$\langle e^{i\Phi_{FID}} \rangle = e^{-\frac{1}{2}\langle \Phi_{FID}^2 \rangle} \approx e^{-T/T_{FID}}, \text{ where } 1/T_{FID} = \frac{A_{\parallel}^2}{8\gamma}, \tag{2.8}$$

because $\frac{1}{2}\langle \Phi_{FID}^2 \rangle = \frac{1}{2}\int_0^T dt \int_0^T dt' A_{z,z}^2 \langle f(t) f(t') \rangle \approx \frac{1}{2}\int_0^T dt \int_{-\infty}^{\infty} d\tau A_{z,z}^2 \langle f(\tau) f(0) \rangle = \frac{A_{z,z}^2}{8\gamma} T$ and $A_{\parallel} = A_{z,z}$. For our system, γ increases with the laser intensity, and consequently

T_{FID} increases with the laser intensity, which is related to the motional averaging effect in NMR.

For large laser power the observed limitation of coherence enhancement arises from dipole-dipole interactions of the nuclear qubit with other ^{13}C nuclei in the environment. In our sample, we estimate this average dipole-dipole interaction to be ~ 1 Hz, consistent with the observed coherence time. Further improvement of the nuclear coherence is achieved via a homonuclear RF-decoupling sequence. The composite sequence (Fig. 2.7d) is designed to both average out the inter-nuclear dipole-dipole interactions (to first order) and to compensate for magnetic field drifts (see Appendix C.1.2). Applying this decoupling sequence in combination with green excitation can further extend the coherence time to beyond one second (Fig. 2.7e, blue points).

2.7 NV based quantum memory

These measurements demonstrate that individual nuclear spins in isotopically pure diamond represent an exceptional candidate for long-lived memory qubits. The qubit memory performance is fully quantified by two additional measurements. First, the average fidelity is determined by preparing and measuring the qubit along three orthogonal directions. This fidelity, $\bar{F} = \frac{1}{2}(1 + \langle C \rangle)$, is extracted from the observed contrast (C) of the Ramsey signal and is presented in Fig. 2.8a for two cases (with and without homonuclear decoupling) [63]. Even for memory times up to (2.11 ± 0.3) s, the fidelity remains above the classical limit of $^2/_3$. Finally, a full characterization of our memory (at one second of storage time) is obtained via quantum process tomography. The corresponding χ-matrix (Fig. 2.8c) reveals an average fidelity of $\bar{F} = (87 \pm 5)$ % (see Appendix C.1.3).

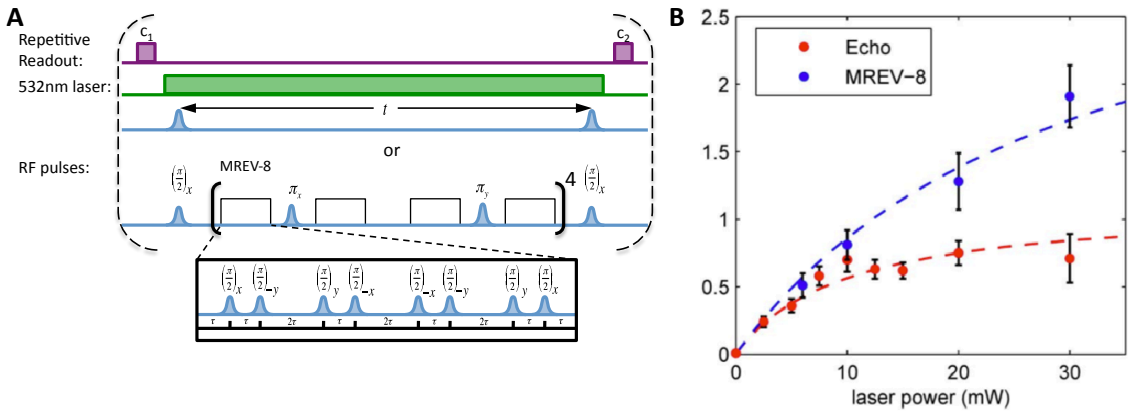

Figure 2.7: | **Nuclear spin coherence, dynamical decoupling. a,** Experimental sequence used to measure the nuclear coherence time. A modified Mansfield Rhim Elleman Vaughan (MREV) decoupling sequence [60] is utilized. It consists of 16 MREV-8 pulse trains interwoven with 8 phase-refocusing π-pulses. Each MREV-8 pulse sequence can be achieved through $\pi/2$ rotations around four different axes. **b,** Nuclear coherence as a function of green laser power. Red data constitute a measurement of T_{2n} using a nuclear spin echo; blue data T_{2n} contain the additional MREV sequence. The dashed fits are calculated from the spin-fluctuator model. Each data point is extracted via a measurement analogous to Fig. 2.6c.

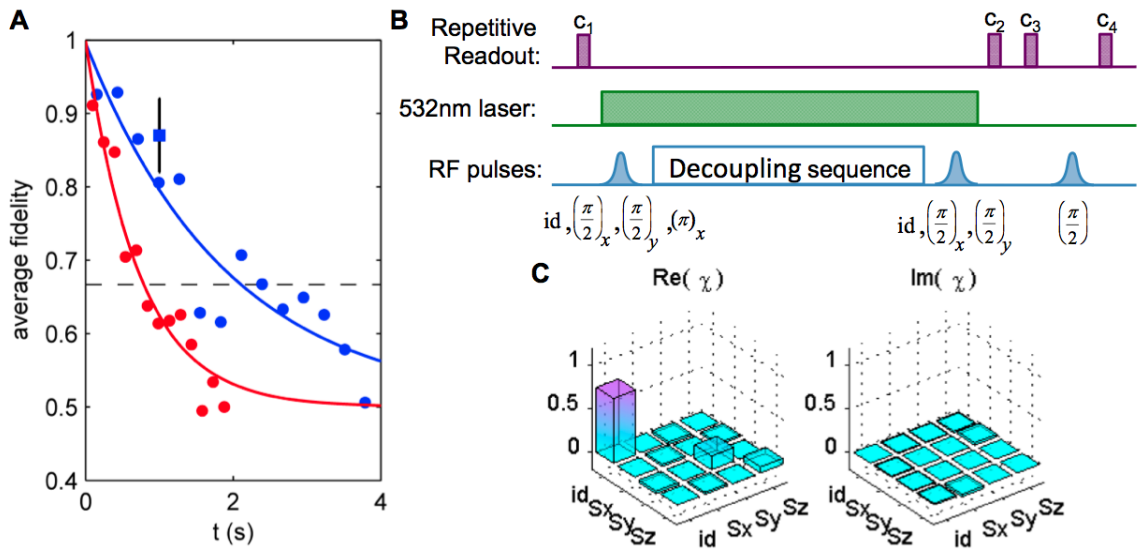

Figure 2.8: | **Nuclear memory fidelity. a,** Average fidelity as a function of time obtained from states prepared along $|x\rangle = \frac{1}{\sqrt{2}}(|\downarrow\rangle + |\uparrow\rangle)$, $|y\rangle = \frac{1}{\sqrt{2}}(|\downarrow\rangle + i|\uparrow\rangle)$ and $|z\rangle = |\downarrow\rangle$. The nuclear echo (red curve) is obtained at 10 mW of green power while the MREV sequence (blue curve) is obtained at 30 mW of green power. The square data point represents the fidelity extracted from process tomography. **b,** Pulse sequence depicting the initialization of four different nuclear states and three subsequent rotations. **c,** The χ matrix of the full quantum process tomography at one second of storage time with 30 mW of continuous green illumination (see Appendix C.1.3).

To quantitatively understand the coherence extension under green illumination, we consider depolarization and dephasing of the nuclear spin due to optical illumination and interaction with the nuclear spin environment. Excitation with 532 nm (de)ionizes the NV center with a rate proportional to the laser intensity[41]. Because the hyperfine interaction is much smaller than the electronic Zeemann splitting, flip-flop interactions between the electronic and nuclear spin can be neglected. However, in the presence of an off-axis dipolar hyperfine field $A_\perp$, nuclear depolarization still occurs at a rate ${}^{1}/_{T_{1n}} \sim \frac{A_\perp^2}{(\gamma_{^{13}C}B/2)^2+(\gamma)^2}\gamma$. While this simple analysis is already in good agreement with our observations (Fig. 2.6b), further insight is provided by a detailed 11-level model of NV dynamics (see Appendix C.1.1). As

T_{1n} limits our readout, a careful alignment of the external field (i.e. choosing $A_\perp \to 0$) and enhanced collection efficiency should enable readout fidelities greater than 99%.

For (de)ionization rates γ much larger than the hyperfine interaction, the dephasing rate depends on the parallel component of the dipole field, ${}^1/_{T^*_{2n}} = \Gamma_{opt} + \Gamma_{dd}$, where Γ_{dd} is the spin-bath induced dephasing rate and $\Gamma_{opt} \sim \frac{A_\parallel^2}{\gamma}$ is the optically induced decoherence. The dashed red line in Fig. 2.7e demonstrates that this model is in good agreement with our data. Application of our decoupling sequence also allows us to suppress nuclear-nuclear dephasing. We find that the main imperfection in this decoupling procedure originates from a finite RF detuning (see Appendix C.1.3). Accounting for this imperfection, we find excellent agreement with our data, as shown by the dashed blue line in Fig. 2.7b. Moreover, this model indicates that the coherence time increases almost linearly as a function of applied laser intensity, suggesting a large potential for improvement.

2.8 Maximal storage time

The use of even higher laser intensities is limited by heating of the diamond sample, which causes drifts in the ESR transition [75]. However, this can be overcome by measuring the nuclear spin using $m_s = \pm 1$ instead of $m_s = 0/+1$, yielding an order of magnitude improvement in the coherence time to approximately one minute. Further improvement can be achieved by decreasing the hyperfine and the nuclear-nuclear interaction strength through a reduction of the ^{13}C concentration, potentially resulting in hour-long storage times (see Fig. 2.9). Finally, it is possible to use coherent decoupling sequences and techniques based upon optimal control theory [76], which scale more favorably than our current dissipation-based method. With such techniques, we estimate that the memory

lifetime can approach the timescale of phonon-induced nuclear depolarization, measured to exceed $T_{1n}^{max} \sim 36$ h [77].

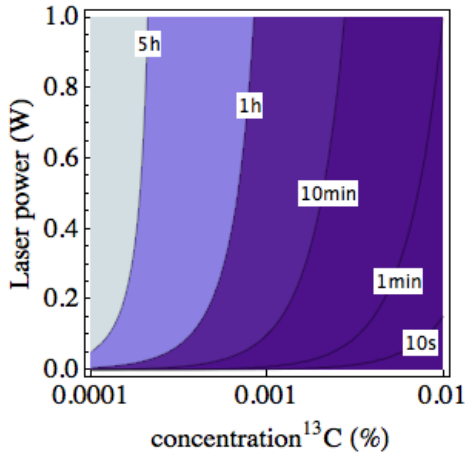

Figure 2.9: | **Estimated nuclear coherence time** as a function of laser power and ^{13}C concentration. The hyperfine interaction is chosen to scale proportionally to the ^{13}C concentration.

2.9 Conclusions and outlook

As a future application of our techniques the realization of fraud resistant quantum tokens can be considered. Here, secure bits of information are encoded into long-lived quantum memories. Along with a classical serial number, an array of such memories, may possible constitutes a unique unforgeable token [78, 79]. With a further enhancement of storage times, such tokens may potentially be used as quantum-protected credit cards or as quantum identification cards [79] with absolute security. Furthermore, NV-based quantum registers can take advantage of the nuclear spin for storage, while utilizing the electronic spin for quantum gates and readout [63, 64]. In particular, recent progress in the deterministic creation of arrays of NV centers [36] and NV-C pairs‘[80], enables the exploration

of scalable architectures [81, 82]. Finally, recent experiments have also demonstrated the entanglement of a photon with the electronic spin-state of an NV center [47]. Combining the advantages of an ultra-long nuclear quantum memory with the possibility of photonic entanglement opens up novel routes to long-distance quantum communication and solid state quantum repeaters [59].

Chapter 3

Nanometer Scale Thermometry in a Living Cell

3.1 Introduction

Sensitive probing of temperature variations on nanometer scales represents an outstanding challenge in many areas of modern science and technology [83]. In particular, a thermometer capable of sub-degree temperature resolution over a large range of temperatures as well as integration within a living system could provide a powerful new tool for many areas of biological, physical and chemical research; possibilities range from the temperature-induced control of gene expression [84, 85, 86, 87] and tumor metabolism [88] to the cell-selective treatment of disease [89, 90] and the study of heat dissipation in integrated circuits [83]. By combining local light-induced heat sources with sensitive nanoscale thermometry, it may also be possible to engineer biological processes at the sub-cellular level [84, 85, 87, 86]. Here, we demonstrate a new approach to nanoscale thermometry

that utilizes coherent manipulation of the electronic spin associated with nitrogen-vacancy (NV) color centers in diamond. We show the ability to detect temperature variations down to 1.8 mK (sensitivity of $9\ \mathrm{mK}/\sqrt{\mathrm{Hz}}$) in an ultra-pure bulk diamond sample. Using NV centers in diamond nanocrystals (nanodiamonds), we directly measure the local thermal environment at length scales down to 200 nm. Finally, by introducing both nanodiamonds and gold nanoparticles into a single human embryonic fibroblast cell, we demonstrate temperature-gradient control and mapping at the sub-cellular level, enabling unique potential applications in life sciences.

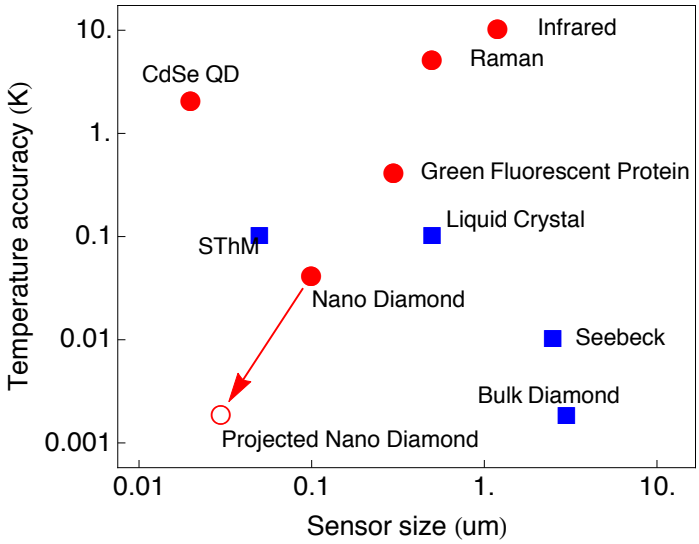

Figure 3.1: | **Accuracy of different temperature sensing techniques** Comparison between the NV quantum thermometer and other reported techniques as a function of sensor size and temperature accuracy. Red circles indicate methods that are biologically compatible, blue those that are not. The red open circle indicates the ultimate expected accuracy for our measurement technique in solution.

Many promising approaches to local temperature sensing [83] are currently being explored. These include scanning probe microscopy [83, 91], Raman spectroscopy [92], and fluorescence-based measurements using nanoparticles [93, 94] and organic dyes [95, 96].

Fluorescent polymers [95] and green fluorescent proteins (GFPs) [96] have recently been used for temperature mapping within a living cell (see Fig. 3.1 for a comparison between spatial resolution and measurement accuracy). However, many of these existing methods are limited by drawbacks such as low sensitivity and systematic errors owing to fluctuations in the fluorescence rate [93, 94], the local chemical environment [95] and the optical properties of the surrounding medium [96]. Moreover, while promising, GFP-based methods rely on cellular transfection [96] that proves to be difficult to achieve in certain primary cell types [97].

3.2 NV based thermometry

Our new approach to nanoscale thermometry utilizes the quantum mechanical spin associated with nitrogen vacancy (NV) color centers in diamond. As illustrated in Fig. 3.2, in its electronic ground state, the NV center constitutes a spin-1 system. These spin states can be coherently manipulated using microwave pulses and efficiently initialized and detected via laser illumination. In the absence of an external magnetic field, the precise value of the transition frequency (Δ) between the $|m_s = 0\rangle$ and $|m_s = \pm 1\rangle$ states exhibits a temperature dependence ($d\Delta/dT = -(2\pi)77$ kHz/K) due to thermally induced lattice strains [75, 42, 98].

The operational principle of NV-based thermometry relies upon the accurate measurement of this transition frequency, which can be optically detected with high spatial resolution (Fig. 3.2). For a sensor containing N color centers, the temperature sensitivity is given

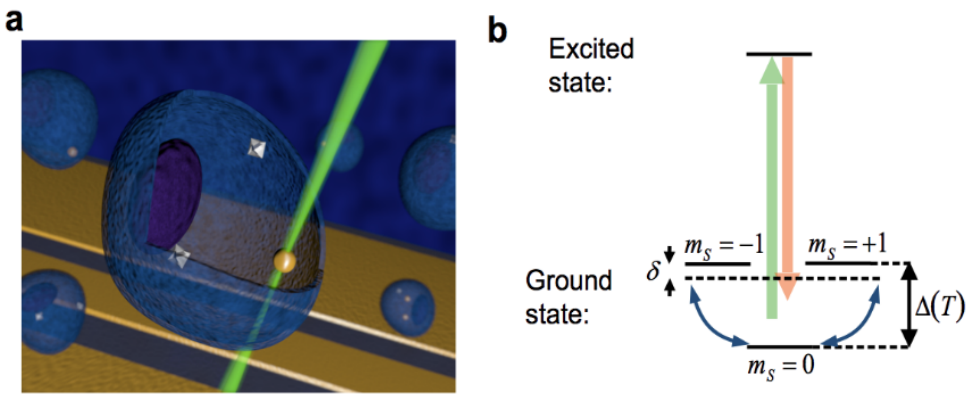

Figure 3.2: | **NV-based nanoscale thermometry. a,** Schematic image depicting nanodiamonds and gold nanoparticles (gold nanoparticles) within a living cell. The controlled application of local heat is achieved via laser illumination of the gold nanoparticle, while nanoscale thermometry is achieved via precision spectroscopy of the NV spins in nanodiamonds. **b,** Simplified NV level diagram showing a ground state spin triplet and an excited state. At zero magnetic field, the $|\pm 1\rangle$ sub-levels are split from the $|0\rangle$ state by a temperature-dependent zero field splitting $\Delta(T)$. Pulsed microwave radiation is applied (detuning δ) to perform Ramsey-type spectroscopy.

by

$$\eta = \frac{C}{d\Delta/dT}\frac{1}{\sqrt{T_{\text{coh}}Nt}}, \tag{3.1}$$

where T_{coh} is the NV-spin coherence time and t is the integration time. Here, we also introduce a factor C to account for imperfections in readout and initialization [52]. Assuming T_{coh} is on the order of a few milliseconds and $C \approx 0.03$[52], a single NV can potentially exhibit a sensitivity better than 1 mK$/\sqrt{\text{Hz}}$. Beyond high sensitivity, NV-based thermometry also offers several distinct advantages over existing methods in biological and chemical temperature sensing. First, owing to diamond's chemical inertness, it is generally robust to changes in the local chemical environment. Second, it can be applied over a wide range of temperatures, $200 - 600$ K [42, 98], which is of particular interest in the study of nanoscale chemical reactions [99].

As a first benchmark experiment, we demonstrate the high temperature sensitivity of NV-based thermometry in a bulk diamond sample. While the NV's magnetic sensitivity has rendered it a competitive magnetometer [100, 101], to accurately determine the temperature, it is necessary to decouple the NV electronic spin from fluctuating external magnetic fields. This is achieved via a modified spin-echo sequence that makes use of the spin-1 nature of the NV defect [102], allowing us to eliminate the effects of an external, slowly varying, magnetic field. Specifically, we apply a microwave pulse at frequency ω (Fig. 3.2b) to create a coherent superposition $\frac{1}{\sqrt{2}}(|0\rangle+|B\rangle)$, where $|B\rangle = \frac{1}{\sqrt{2}}(|+1\rangle+|-1\rangle)$. After half the total evolution time τ we apply a 2π echo-pulse that swaps the population of the $|+1\rangle$ and $|-1\rangle$ states (Fig. 3.3a). Following another period of free evolution for time τ, quasi-static, magnetic-field-induced shifts of these $|\pm 1\rangle$ levels are eliminated, allowing for accurate temperature sensing. In the experiment, we use a CVD-grown, isotopically pure diamond ($99.99\,\%$ spinless ^{12}C isotope) sample [72] to further reduce magnetic-field fluctuations originating from the intrinsic ^{13}C nuclear spin bath. As shown in Fig. 3.3, this allows us to observe coherence fringes approaching 0.5 ms. Interestingly, for all NVs tested, we observe a characteristic low-frequency beating of the fluorescence signal that varies from NV to NV, which is most likely due to locally fluctuating charge traps [103]. Despite this beating, for a fixed evolution time 2τ, the NV spin depends sensitively on the sample temperature (Fig. 3.3). We observe a temperature sensitivity of $\eta = (9 \pm 1.8)$ mK/$\sqrt{\text{Hz}}$ for $2\tau = 250\ \mu$s.

The temperature sensitivity η for bulk diamond is estimated from the measurement shown in Fig. 3.3. Using the standard deviation σ (shown error bars) we evaluate the accuracy as $\delta T = \sigma/(c\,\frac{d\Delta}{dT}\,2\tau)$, where c is the oscillation amplitude and 2τ is the free evolution

time. We find that for integration times $t < 30\ s$ (limited by temperature stability) the temperature accuracy improves as $\sqrt{t}$, giving a sensitivity $\eta = \delta T\sqrt{t}$. With 30 seconds of integration, we achieve a measurement accuracy $\delta T = 1.8 \pm 0.3$ mK. While the measurement sequence for a single value of 2τ allows us to determine the temperature only up to a multiple of $(2d\Delta/dT2\tau)^{-1}$, absolute temperature variations can be determined by repeating the measurement for $2\tau' < 2\tau$ as shown in Fig. 3.3b.

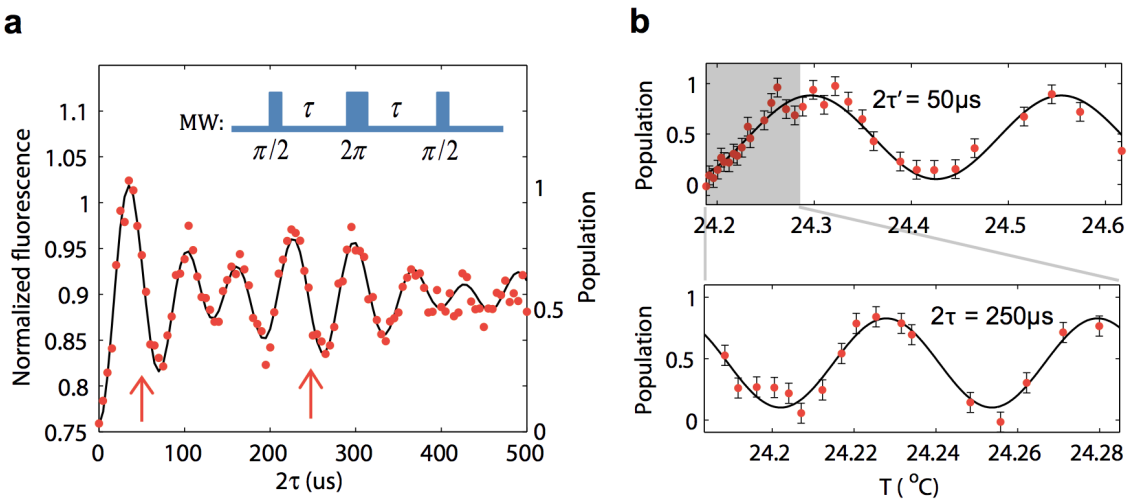

Figure 3.3: | **Sensitivity of single NV Thermometer. a,** Measured fluorescence as a function of echo evolution time 2τ (red points); the black solid line indicates a fit corresponding to a damped cosine function with two distinct frequencies. The characteristic beating can be explained by fluctuating proximal charge traps located at distances of about 50 nm. The inset depicts the microwave 2π-echo-pulse sequence used to cancel unwanted external magnetic field fluctuations [102]. **b,** Measured fluorescence (red points), corresponding error bars (one standard deviation) and best fit line as function of temperature for an echo time of $2\tau = 250\ \mu$s (bottom) and $2\tau' = 50\ \mu$s (top). The fixed evolution times of 2τ and $2\tau'$ are indicated in (a) by red arrows. The temperature is controlled by a Peltier element at the sample mount, while the (local) x-axis temperature is determined via a thermistor located immediately next to the sample. The fluorescence is converted to population by normalizing to two reference measurements where the spin is prepared in $m_s = 0$ ($m_s = -1$).

3.3 Sensing temperature with confocal resolution

We now demonstrate the high spatial resolution of NV-based thermometry. This is achieved by using nanodiamonds. In most commercially available nanodiamonds, the NV coherence time is limited to approximately 1 μs due to additional paramagnetic impurities. While this shortened coherence time reduces the intrinsic temperature sensitivity for a single defect, this decrease can be offset by using an ensemble of NVs to enhance the signal to noise ratio by a factor of $\sqrt{N}$. Note that unlike NV-based magnetometry, where the proximity to the source (often limited by nanodiamond size) is critical to the maximum sensitivity, NV thermometry is not subject to such a constraint; in fact, the excellent thermal conductivity of diamond ensures that *all* NV centers within a nanocrystal are in thermal equilibrium with the local heat environment. To maximize the number of NV centers and to minimize the lattice strain, our measurements are performed on single-crystalline nanodiamonds containing approximately 500 NV centers (Adamas Nanotechnologies). The zero-field splitting Δ of the NV ensemble, and thus the temperature, is determined by recording a continuous-wave electron spin resonance (ESR) spectrum. Specifically, we measure changes to the zero-field splitting by recording the fluorescence at four different frequencies centered around $\Delta = 2.87$ GHz (Fig. 3.4a). This procedure eliminates unwanted effects from fluctuations in the total fluorescence rate, ESR contrast, Rabi frequency and magnetic field, yielding a robust thermometer.

Combining our nanodiamond thermometer with the laser heating of a gold nanoparticle allows us to both control and monitor temperature at nanometer length scales (Fig. 3.4). Both nanodiamonds and gold nanoparticles (nominal diameter 100 nm) are initially spin-coated on a microscope coverslip. Using a confocal microscope with two independent

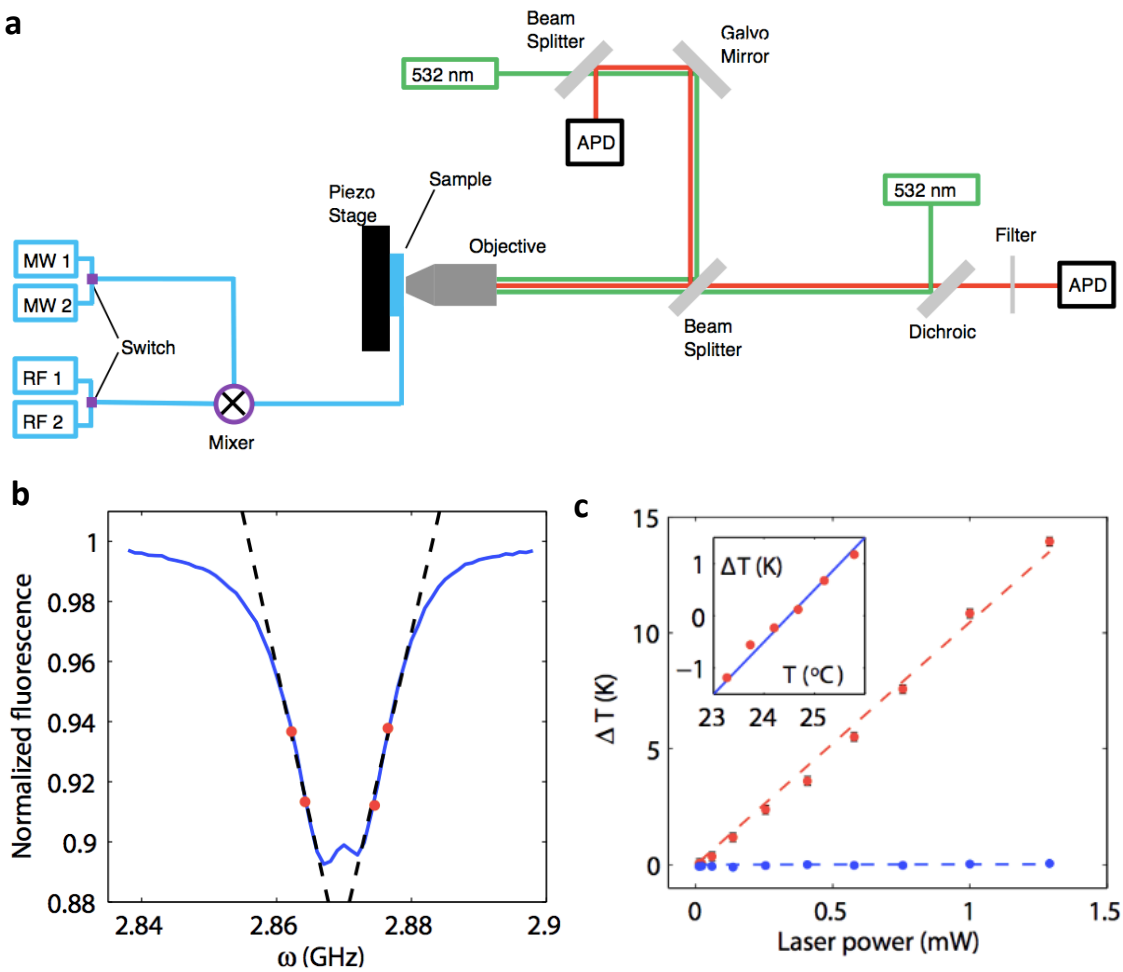

Figure 3.4: | **Sub-micron thermometry using nanodiamonds. a,** The experimental apparatus consists of a confocal microscope with two independent excitation/collection paths allowing for measurement and heating at two independent locations simultaneously. Microwaves are delivered via a lithographically defined coplanar waveguide on top of a glass coverslip. **b,** Frequency scan of a single nanodiamond containing approximately 500 NV centers. The four red points indicate the measurement frequencies used to extract the temperature. **c,** Temperature of a single nanodiamond as a function of laser power for two different laser-focus locations. The red data points depict the dramatic heating of a nanodiamond as a result of laser illumination on a nearby gold nanoparticle. The blue data points depict the same measurement with the laser focus displaced by 0.8 μm from the gold nanoparticle location; this results in the negligible heating of the nanodiamond as a function of laser power. The inset shows the measured temperature change of a nanodiamond, when the surrounding temperature is controlled by a Peltier element.

scanning beams, we co-localize gold nanoparticles and nanodiamonds with ~ 100 nm resolution.

Under green excitation, the gold nanoparticles used in the present work exhibit an emission spectrum which is slightly blue shifted relative to the NV spectrum (Fig. 3.5a)). This allows us to use a frequency doubled YAG laser (532 nm) for excitation of both NV centers and gold nanoparticle. To distinguish the fluorescence of nanoparticles from NV centers, a (560 ± 25) nm band pass filter is used. By comparing scans with and without a band pass filter (Fig. 3.5b,c)), it is possible to clearly identify the location of gold nanoparticles. To verify the presence of a nanodiamond, we utilize the electron spin resonance (ESR) response of NV centers; in particular, we measure changes to the photoluminescence under microwave excitation.

While locally heating the gold nanoparticle via continuous illumination with a variable-power green laser (focused to a diffraction limited spot), we simultaneously measure the temperature at the nanodiamond location using ESR spectroscopy.

The ability to measure temperature with nanodiamonds is verified by heating the substrate temperature over a range of 2.5 K and simultaneously monitoring the zero-field splitting (see Fig. 3.4b, inset). To demonstrate nano-scale temperature control Fig. 3.4b depicts the temperature change recorded by the Nanodiamond as a function of the green laser power applied to the gold nanoparticle at a distance of 0.8 ± 0.1 μm. To further verify that the temperature change originates from local laser induced heating of the gold nanoparticle, we repeat the measurement with the excitation laser displaced from the Nanodiamond by 0.8 μm in the opposite direction. In this case, the temperature measured by the nanodiamond remained constant as a function of laser power (blue points), thereby confirming the

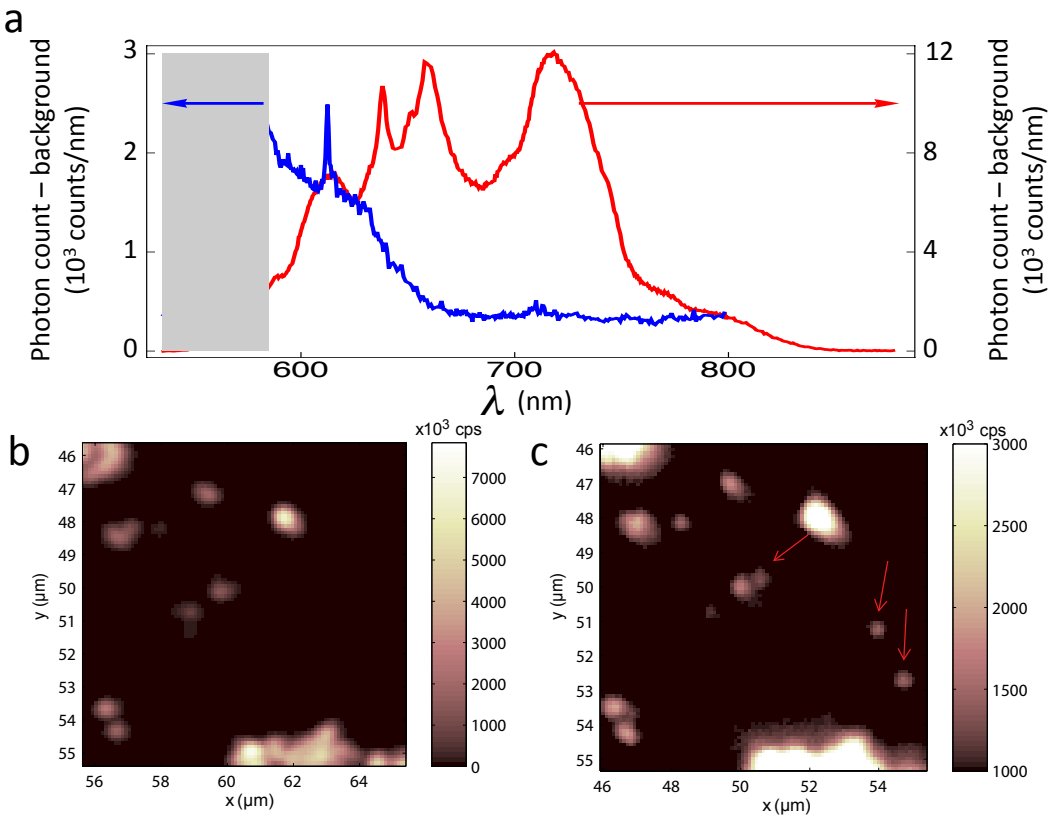

Figure 3.5: | **Co-localization of nano diamonds and gold nanoparticles. a,** Fluorescence spectrum under green excitation of gold nanoparticles (blue data) and nanodi- amonds (red data). The shaded region indicates the bandpass filter used for detection of gold. The arrows mark the respective y-axis scaling for each curve. **(c)** Confocal scan of gold nanoparticles and nanodiamonds taken with a 633 nm long-pass filter. **(b)** Scan of the same area using a 560 25 nm bandpass filter. For visual clarity, a lower bound of 1000 kcps and an upper limit of 3000 kcps is set. The red arrows indicate locations of gold nanoparticles

locality of the heat source.

From a linear fit to the data we estimate the accuracy of our Nanodiamond sensor to be $\delta T = (44 \pm 10)$ mK and the corresponding sensitivity of $\eta = (900 \pm 200) mK/\sqrt{Hz}$. The accuracy is calculated by fitting a linear function, with slope m, to the data (red dashed line), which determines the measurement accuracy using $\delta T = \sqrt{\frac{1}{N-1}\Sigma_{i=1}^{N}\left(T_i - m\ P_i\right)^2}$; where T_i is the measured temperature and P_i the corresponding laser power. The error bars are evaluated as $\sigma\left(\delta T\right) = \delta T\sqrt{1 - \frac{2}{N-1}\frac{\Gamma^2(n/2)}{\Gamma^2((n-1)/2)}}$, where $\Gamma(\cdot)$ indicates the Gamma distribution.

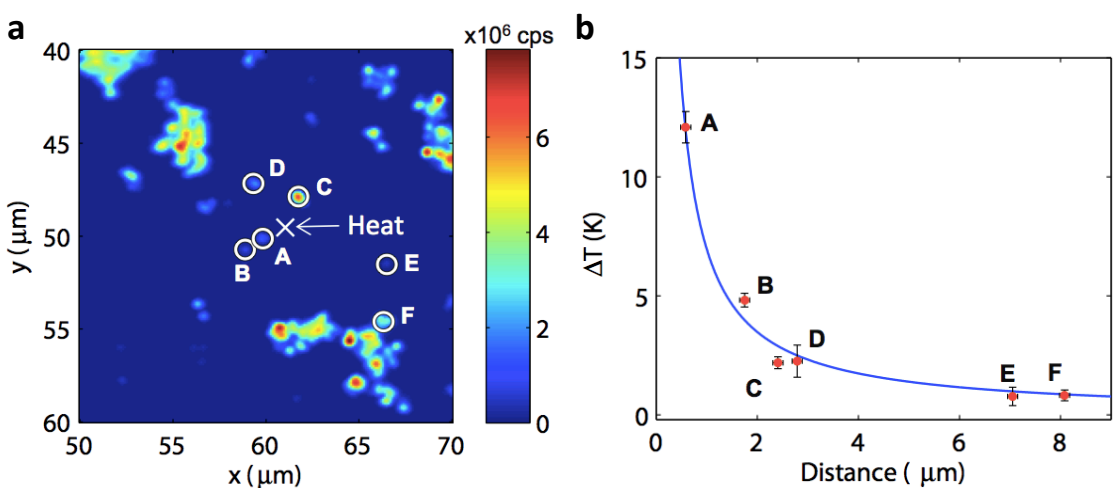

Figure 3.6: | **Sub-micron thermometry using nanodiamonds. a,** Two-dimensional confocal scan of nanodiamonds (circles) and gold nanoparticles (cross) spin-coated onto a glass coverslip. The color bar represents fluorescence given in counts per second (cps). **b,** Temperature changes measured (red points) at the six nanodiamond locations in (a) as a function of distance from the illuminated gold nanoparticle (cross). The blue curve represents the theoretical temperature profile based upon a steady-state solution of the heat equation. All data in this figure are obtained on a glass coverslip, and all error bars correspond to one standard deviation.

The measured temperature change agrees with the theoretically expected temperature profile based upon a steady-state solution of the heat equation, $\Delta T(r) = \frac{\dot{Q}}{4\pi\kappa r}$, where $\dot{Q}$

is the heat dissipation, κ is the thermal conductivity of glass and r is the distance between the nanodiamond and the gold nanoparticle. As shown in Fig. 3.6a, by recording the temperature of six nanodiamonds at different distances from the laser-heated gold nanoparticle we find that the measured temperature profile (Fig. 3.6b) is in excellent agreement with the theoretical steady-state prediction (solid line). This allows us to directly estimate the temperature change at the location of the gold nanoparticle to be 72 ± 6 K.

3.4 Injection of nanodiamonds into cells

To demonstrate that nanodiamond thermometry is compatible of measuring temperature within living cells, we introduce nanodiamonds and gold nanoparticles into human embryonic fibroblast WS1 cells via nanowire-assisted delivery [97]. Nanodiamonds and gold nanoparticles were introduced into WS1 cells via silicon nanowire-mediated delivery [97]. For this the silicon nanowires were treated with 3-amino- propyltrimethoxysilane to present NH_2 functionality on the surface, nanodiamonds and gold nanoparticles were subsequently attached via electrostatic binding. Afterwards, human embryonic fibroblast WS1 cells were plated on the silicon nanowire substrates and cultured overnight. The cells were removed by trypsin treatment and re-plated on a glass slide with lithographically defined strip lines for ESR measurements. To investigate cell viability the samples were stained with calcein-AM and ethidium homodimer-1 for the live/dead assay.

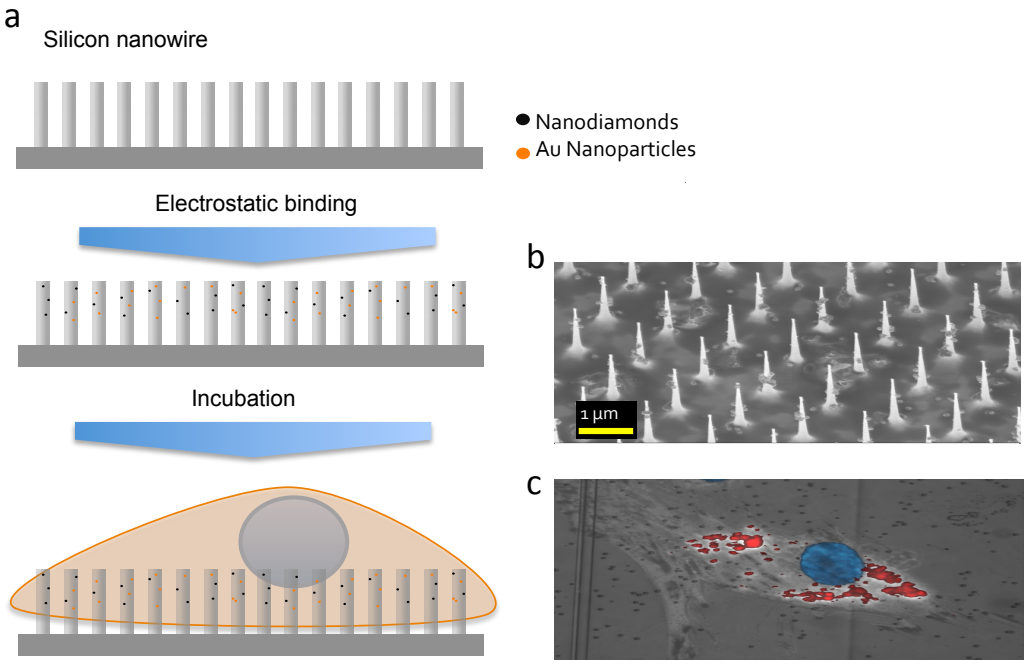

Figure 3.7: | **Nano-injection assisted injection of nano-particles into living cells. a,** Schematic description of nanoinjection. The array depicts etched silicon nanowires. The small points represent gold colloids and nanodiamonds coated on the nanowire. In the bottom sub-figure a cell with nucleus is grown on the nanowire array. **b,** Electron microscopy image of a nanowire array coated with gold nanoparticles and nanodiamonds. **c,** Confocal image of WS1 cell with stained nucleus (blue) and nanodiamonds (red). (credit for image **b** and **c**: Minako Kubo)

3.5 Temperature sensing in a single living cell

Just as in the control experiments of section 3.3, we probe the temperature at two different locations (NV_1 and NV_2) within a single cell while locally heating an individual gold nanoparticle (Fig. 3.8a). As shown in Fig. 3.8b, NV_1, which is significantly closer to the heat source, exhibits a stronger temperature dependence as a function of laser power than NV_2. Varying the incident power allows us to generate controlled temperature gradients of up to 5 K over distances of approximately 7 μm. To ensure that this temperature gradient is created by the controlled illumination of the nanoparticle and does not result from heating of the cellular cytoplasm, we displace the laser spot from the gold nanoparticle; this then results in a negligible temperature change at the location of NV_1 with $\Delta T = (-20 \pm 50)$ mK (green square, Fig. 3.8b). The increased measurement uncertainty for larger laser powers is the result of heating fluctuations from drift of the gold nanoparticle and changes in the relative distance between gold nanoparticle and gold colloid.

The experiments shown in Fig. 3.8b clearly demonstrate the sub-micron measurement of an intra-cellular heat gradient. However, the substantial heating induced by constant illumination for an extended period of time ultimately leads to the death of the cell, which is confirmed using a standard live/dead assay (Calcein AM/Ethidium Homodimer-1). To demonstrate that our technique can be employed within living cells, we increase the concentration of gold nanoparticles to allow for heat generation at different locations by simply moving the laser focus. Then, we measured the temperature variation at a single nanodiamond (bar plot in Fig. 3.9a) while introducing a slight heating of gold nanoparticles in two differing locations (crosses). After our measurement, the viability of the cell is confirmed (Fig. 3.9b).

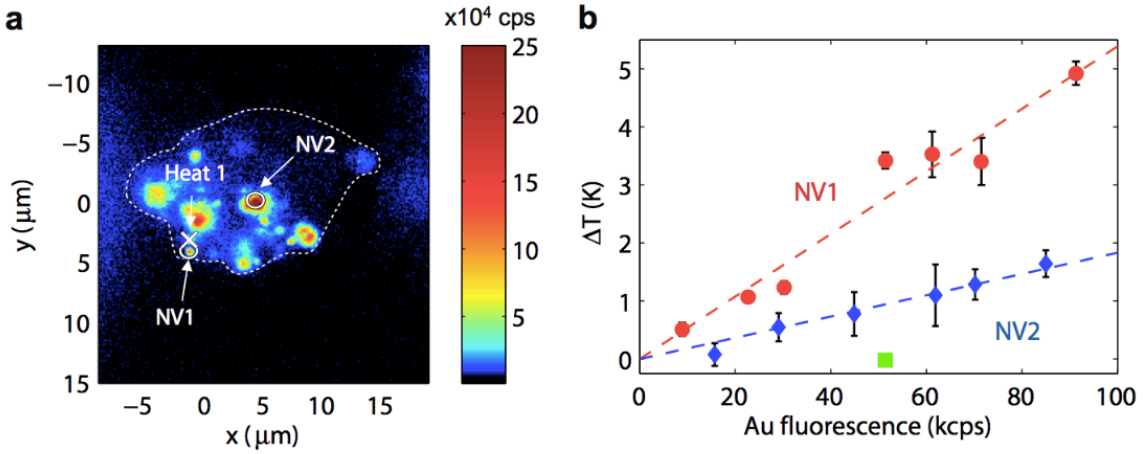

Figure 3.8: | **Nanoscale thermometry in cells. a,** Confocal scan of a single cell under 532 nm excitation with collection above 638 nm. The cross corresponds to the position of the gold nanoparticle used for heating, while circles represent the location of the nanodiamonds (NV_1 and NV_2) used for thermometry. The dotted line provides a guide to the eye and outlines the cell membrane. Color bars indicate the fluorescence in cps. **b,** Measured change in temperature at the position of NV_1 and NV_2 relative to the incident laser power applied to the gold nanoparticle. Dashed lines are linear fits to the data. Each point consists of an average of 5 measurements with each individual measurement taking 4 seconds. The error bars (one standard deviation) are set by fluctuations in the laser heating of the gold nanoparticle.

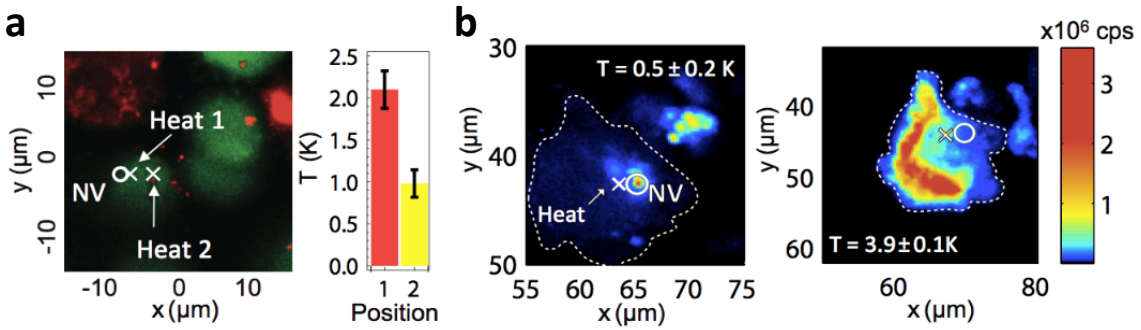

Figure 3.9: | **Standard live/dead assay. a,** Fluorescence scan of stained cells (live/dead assay) with excitation at $494/528$ nm and emission at 515 nm (green - cell alive) and 617 nm (red - cell dead). The bar plot depicts the temperature of a single nanodiamond (circle) with local heat applied at two different locations (cross). **b,** Confocal fluorescence scans of an individual cell under varying illumination power. Excitation occurs at 532 nm and collection is above 630 nm. Cell death is indicated by the penetration of ethidium homodimer-1 through the cell membrane, staining the nucleus. At low laser powers, the cell remains alive, while cell-death occurs as laser-induced heating is increased.

Finally, we demonstrate that our method can be used to control cell viability. To start, we heat the cell with $12\ \mu$W of laser power and measure a temperature change of 0.5 ± 0.2 K at the nanodiamond location; this corresponds to a change of approximately 10K at the gold nanoparticle spot. At this point, the cell is still alive, as confirmed by the absence of ethidium homodimer-1 fluorescence inside the membrane (Fig. 3.9b). By increasing the laser power to 120μW, we induce a temperature change of 3.9 ± 0.1K at the nanodiamond location (approximately 80K at the location of the laser focus); in this case, the cell is flooded with fluorescence from the ethidium homodimer, thus signaling cell death. This proof-of-principle experiment indicates that nanodiamond thermometry may enable the optimization of nanoparticle-based photothermal therapies [90].

3.6 Ultimate sensitivity

The ultimate sensitivity of our method is limited by the NV coherence time and the number of defect centers. In our current experiment, we have demonstrated a sensitivity of 9 mK$/\sqrt{\text{Hz}}$ (with a free evolution time of 250 μs). Two natural extensions enable longer NV coherences: 1) decreasing the ^{13}C concentration to suppress the nuclear spin bath and 2) further dynamical decoupling. These methods can, in principle, allow us to extend the evolution time up to $T_1 \sim 3$ ms. In combination with a nanocrystal that contains ~ 1000 NV centers, this could yield an ultimate sensitivity limit of 80 μK$/\sqrt{\text{Hz}}$. Further improvement may be possible by employing spin squeezed states [104]. Finally, the determination of absolute temperature is limited by variations of the zero-field splitting due to spatially varying strain. For low strain diamond samples, we find that the variation in the zero-field splitting is less than 60 kHz, allowing for sub-K absolute temperature determination. In addition, the use of an ensemble of NV centers in different nanodiamonds with uncorrelated strain values allows for a further increase in absolute sensitivity by a factor $\sqrt{n}$, where n is the number of nanodiamonds.

In cases where our method is used to probe a system that is in solution (e.g. cells, chemical reactions), the primary accuracy limit is set by heat dissipation during the measurement process. In particular, the microwave spectroscopy used to detect changes in the NV zero-field splitting also induces heating of the solution. In the present experiment, we utilize a lithographically fabricated microwave loop (diameter 200 μm) to generate an ac-magnetic field, $B \approx 10$ mGauss, for spin manipulations. Estimating the effective dipole field created by the microwave loop shows that the solution (water) absorbs 10^{-6} W of power yielding a temperature increase of 5 mK in the steady state. By using a smaller microwave loop

($20\ \mu$m) and reducing the duty cycle, it could be possible to decrease the heating of the solution to approximately $50\ \mu$K.

3.7 Conclusions and outlook

Our experiments demonstrate that NV centers in diamond can be used as robust temperature sensors that combine the virtues of sub-micron spatial resolution, sub-degree thermal sensitivity and bio-compatibility. The sensitivity of our current measurement can be enhanced by improving the relevant coherence time and by increasing the number of NV centers within the nanocrystal. Optimizing these factors should allow us to reach sensitivities of $80\ \mu\text{K}/\sqrt{\text{Hz}}$, yielding the ability to sense sub-kelvin temperature variations with milli-second time resolution. In solution, the ultimate accuracy of our method will likely be limited by residual heating during the measurement process. As discussed in section 3.6, this limit is in the range of $50\ \mu$K to 5 mK, depending on experimental conditions. While the present work focuses on monitoring temperature variations, the use of diamond samples with low strain or, alternatively, ensembles of nanodiamonds, should allow for the realization of an absolute thermometer. The spatial resolution of our method can be further improved by using far-field sub-diffraction techniques [105].

The present observations open up a number of intriguing possibilities. For instance, the simultaneous measurement and control of a sub-cellular thermal gradient could enable the accurate control of gene expression [106]. Further improvements in sensitivity may allow for real-time observations of non-equilibrium sub-cellular processes in biological and medical applications [93]. The large dynamic range of our quantum thermometer and it's intrinsic robustness may also allow for the direct microscopic monitoring and control of chemical

reactions [99]. Moreover, combining our technique with two-photon microscopy [107, 108] may enable *in vivo* identification of local tumor activity by mapping atypical thermogenesis at the single-cell level [109]. Finally the combination of thermoablative therapy with our temperature sensor constitutes a potent tool for the selective identification and killing of malignant cells without damaging surrounding tissue [89, 90].

Chapter 4

Far-field Optical Imaging and Manipulation of Individual Spins with Nanoscale Resolution

4.1 Introduction

A fundamental limit to existing optical techniques for measurement and manipulation of spin degrees of freedom is set by diffraction, which does not allow spins separated by less than about a quarter of a micrometer to be resolved using conventional far-field optics. Here, we report an efficient far-field optical technique that overcomes the limiting role of diffraction, allowing individual electronic spins to be detected, imaged and manipulated coherently with nanoscale resolution. The technique involves selective flipping of the orientation of individual spins, associated with Nitrogen-Vacancy (NV) centers in room temperature diamond, using a focused beam of light with intensity vanishing at a control-

lable location, which enables simultaneous single-spin imaging and magnetometry at the nanoscale with considerably less power than conventional techniques. Furthermore, by inhibiting spin transitions away from the laser intensity null, selective coherent rotation of individual spins is realized. This technique can be extended to sub-nanometer dimensions, thus enabling applications in diverse areas ranging from quantum information science to bioimaging.

Optical techniques constitute powerful tools for spin detection and manipulation that enable applications ranging from atomic clocks [110] and magnetometers [7], to quantum information processors [111, 63, 112, 81] and novel sensors and imaging modalities for biological and life sciences [52, 113, 100, 101, 72]. Several promising methods for fluorescence imaging have recently been developed to surpass the diffraction limit and are already being applied to important problems in biology and neuroscience [114, 115, 116] as well as sub-wavelength optical lithography [117, 118, 119]. For example, sub-diffraction imaging of fluorophores can be obtained by stimulated emission depletion (STED) microscopy and related methods based on reversible saturable optical linear fluorescence transitions (RESOLFT) [120, 121, 122]. Using optical fields with intensity zeros and steep spatial gradients, such as those provided by doughnut-shaped beams, one can transiently switch the fluorophores to a different state everywhere except for a small region near the vanishing optical intensity. In this case the emitters from that small region can be separated from neighbours closer than the diffraction limit. Since the emitters are switched to the designated (on or off) state provided the optical stimulation rate exceeds that of the spontaneous decay rate of that state, the ultimate resolution is, in principle, limited only by the applicable optical power [122].

4.2 The concept of sub-diffraction spin detection and control

Our new approach to sub-diffraction spin detection and manipulation is outlined in Fig. 4.1. We consider an electronic spin system, such as the NV center in diamond, which can be polarized via optical pumping, coherently manipulated with resonant microwave radiation, and read-out with spin-state-dependent fluorescence. Improved spatial resolution is achieved by illuminating the sample with a doughnut-shaped optical beam just prior to optical spin readout. Spins positioned directly in the center of the doughnut beam are not affected by it. However, spins that are even a few tens of nanometers away from the zero intensity position are re-polarized by the doughnut beam and thus contribute differently to the fluorescence signal, providing nanoscale imaging contrast. Moreover, selective coherent manipulation of a spin in the doughnut center can be achieved by simultaneous exposure to resonant microwave radiation and the optical doughnut beam (Fig. 4.1c). The essence of this process is that all coherent spin transitions away from the doughnut center are inhibited by the laser field, thereby allowing coherent rotation of an individual spin at the doughnut center.

Before proceeding we note that STED and related RESOLFT techniques have been demonstrated to be effective in systems containing metastable states [120], but in all cases electronic excitations were critically employed to resolve at sub-diffraction distances. A specific advantage of our present approach, which we refer to as spin-RESOLFT, stems from the exceptionally long lifetimes associated with spin sublevels of electronic ground states in certain systems, which can reach seconds and exceed the lifetimes of electronic

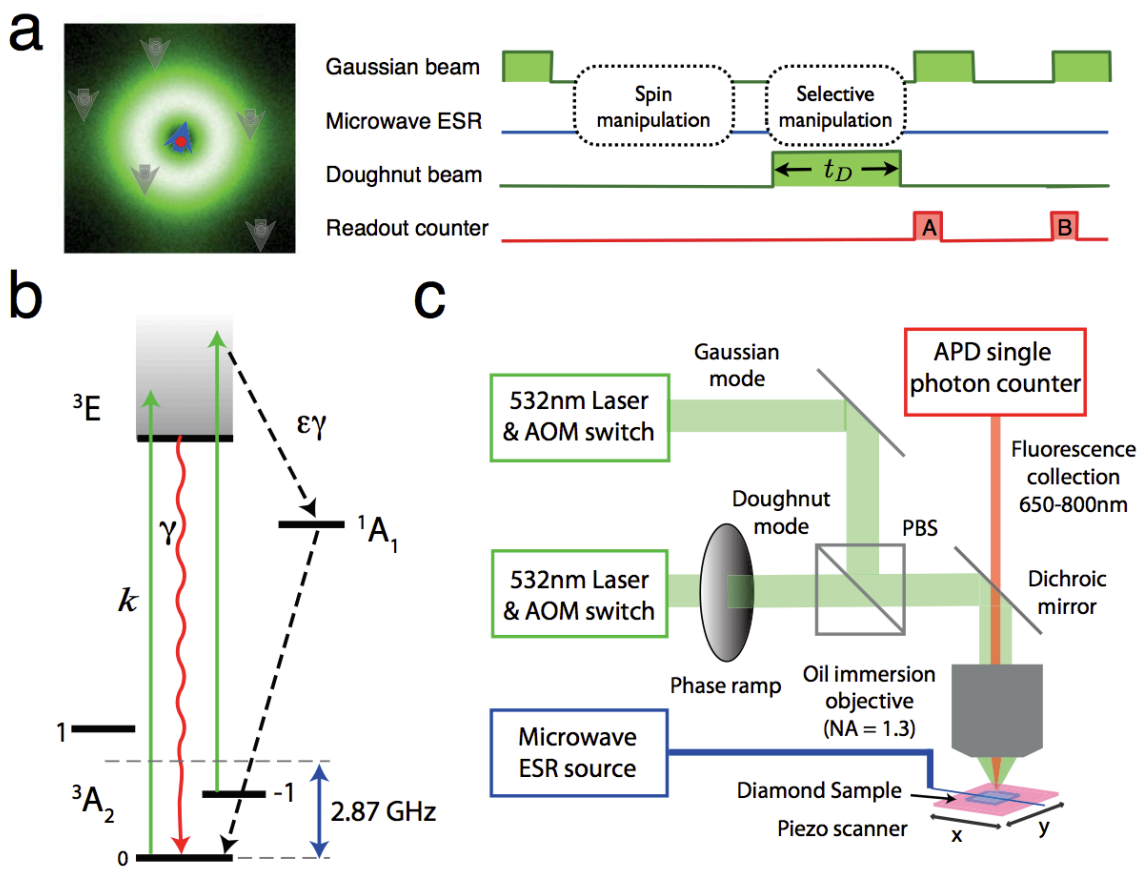

Figure 4.1: | **Principles of sub-diffraction far-field optical imaging and magnetometry** of individual NV electronic spins in diamond ("spin-RESOLFT"). **a**, Experimental sequence using pulsed optical and microwave excitation. NV spins are first optically pumped to $m_s = 0$ using a Gaussian beam at 532 nm followed by microwave manipulation. Application of 532 nm doughnut beam re-polarizes the outer ring to $m_s = 0$, allowing the spin-state of the central dark region to be independently read-out. **b**, Energy level diagram of NV center showing optical absorption (k) and fluorescence (γ) rates. NV electronic spins are optically pumped from $|m_s| = 1$ to $m_s = 0$ spin states through non-radiative relaxation via the metastable $^1A_1$ singlet state. Microwave fields at around 2.87 GHz coherently manipulate the NV spin states. The differential spin-state population is measured via spin-state-dependent fluorescence in the red. **c**, Schematic of experimental approach. NV centers are imaged using confocal microscopy by scanning the sample around the focal point using a 3-axis piezo stage. The doughnut beam is generated by passing a Gaussian beam through a vortex waveplate (2π azimuthally varying phase ramp).

transitions by more than six orders of magnitude. Optical transitions involving such ground-state spin levels can be differentially saturated by scattering just a few photons. Therefore, spin-RESOLFT allows individual electronic spins associated with NV centers to be imaged on the nanoscale, with several orders of magnitude lower laser power than most other super-resolution imaging techniques. This offers significant advantages in many applications, especially to biological systems. Alternatively, for a given power of the doughnut laser beam, spin-RESOLFT allows a dramatic improvement in resolution relative to STED and other RESOLFT approaches, potentially extending to sub-nanometer scales. We also note that another method for resolving closely spaced spins employs large magnetic field gradients [101], as in conventional magnetic resonance imaging. This method, however, requires detailed knowledge of the magnetic gradient topography and is only possible for spins that can be resolved spectrally in ESR or NMR measurements. In what follows we show that the present technique allows one to use far-field optical detection to resolve individual spins spaced by sub-diffraction distances, sense their local magnetic environment, and perform coherent spin manipulation, even when ESR or NMR measurements are not capable of resolving individual spins spectrally.

4.3 Nanoscale optical imaging using spin state

Our experimental demonstration makes use of individual NV centers in diamond. An electronic spin associated with the NV triplet ground state can be optically polarized, coherently manipulated using conventional electron spin resonance (ESR) techniques [28, 123], and read-out through spin-state-dependent fluorescence [124] (see Fig. 4.1b). NV centers in ultra pure diamond display exceptional electron spin lifetimes (T_1), of several milliseconds

at room temperature [81]. To realize sub-diffraction optical imaging and magnetometry using NV spins, we first polarize all NV centers in the field of view into the ground spin state $m_s = 0$ using a focused Gaussian beam; then drive ESR spin transitions to the $m_s = +1$ or -1 state, or to a coherent superposition of these states; and subsequently use an optical doughnut beam to selectively re-polarize the spins of nearby NV centers. NV centers located in regions of high intensity are optically pumped to the $|0\rangle$ ground state, whereas an NV center located at the central intensity zero remains unaffected and maintains its original state. Thus, spatial information associated with this central NV is encoded into its electronic spin state. It is subsequently determined by conventional optical readout of the NV fluorescence, since the NV centers that are not repolarized are darker than those that are repolarized. Scanning the sample with respect to the beams and repeating the above procedure allows sub-diffraction imaging of the NV centers in the field of view, as well as sensitive nanoscale magnetometry at the location of each NV center due to the Larmor precession of a coherent superposition of NV spin states (detectable via spin-state-dependent fluorescence) [52, 100].

Fig. 4.2 shows example sub-diffraction optical images of an NV electronic spin in diamond, acquired using the spin-RESOLFT technique. A ten-fold improvement of 1D resolution was obtained for a fixed power of approximately 2 mW, focused to a diffraction limited spot of 0.07 μm^2, by increasing the duration of the doughnut beam pulse. A similar resolution improvement was achieved for much lower doughnut power of about 0.1 mW, provided the decrease in power is compensated by an increase in doughnut duration. These observations are in excellent agreement with predictions from a simple model of the imaging resolution Δr provided by our sub-diffraction spin detection technique:

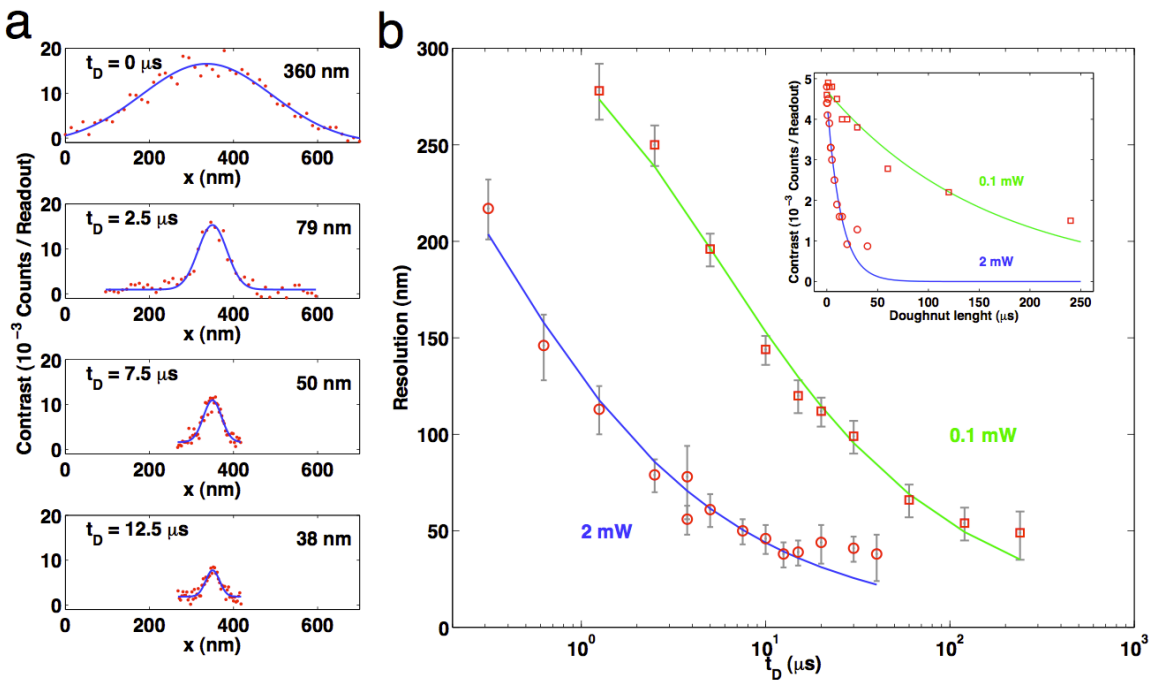

Figure 4.2: | **Demonstration of sub-diffraction optical spin imaging.** **a**, Scanning 1D optical images of an NV electronic spin in diamond, for several values of doughnut pulse duration (t_D) at 2 mW total doughnut beam power. Contrast is defined as the number of readout counts during the reference readout (period B in Figure 4.1) minus the number of counts during signal (period A). **b**, Resolution (FWHM) of 1D spin images as a function of doughnut pulse duration, for both 2 mW and 0.1 mW total doughnut beam power. The error bars represent 95% confidence intervals. Solid lines represent a fit to Equation (1). Equivalent resolution is achieved for lower power optical fields applied for longer duration. Long NV spin lifetimes (>10 ms) enables comparable resolution for the present spin-RESOLFT technique with $\sim$0.1$\%$ of the laser power used in STED imaging of NV centers [122]. Resolution is limited by imperfections of the doughnut intensity zero, and/or mechanical instability during doughnut application, which leads to loss of contrast for very large t_D (inset).

$$\Delta r \approx \frac{\lambda/2\mathrm{NA}}{\sqrt{1+\Gamma t_D}} \tag{4.1}$$

Here λ is the wavelength of the optical field, NA is the numerical aperture of the objective, Γ characterizes the maximum rate of optical excitation out of spin state $|1\rangle$, and t_D is the duration of the doughnut beam. Note that the spin imaging resolution is determined by the product of the power and duration of the doughnut beam: hence sub-diffraction-limited resolution can be achieved with a laser power that is well below optical saturation of the excited state (^3E), provided that t_D is sufficiently long. Since the maximum length of t_D is limited by spin state relaxation ($T_1 \approx 8$ ms) for spin-RESOLFT and by the electronic excited state lifetime ($\sim$10 ns) for STED, we are able to realize sub-diffraction spin imaging using sub-mW doughnut beam power with comparable resolution to that of STED using about one Watt of doughnut power [122].

4.4 Spin imaging resolution

The spin-RESOLFT signal is proportional to $f(x) = n_0(x)I_G(x)$ where n_0 is the population of the $m_s = 0$ state, $I_G = \exp(-\alpha(x/r_C)^2)$ is the intensity profile of the gaussian beam used for readout of the electronic spin, $r_C = \lambda/2\mathrm{NA}$ is the confocal resolution and $\alpha = 4/log(2)$. n_0 depends on duration of the doughnut beam t_D; it can be evaluated by solving rate equations. In the limit of large lifetime of spin transition, it is given by $n_0 = \exp(-R_x t_D)$, where R_x is the position-dependent optical polarization rate. In the unsaturated regime, $R_x = R_0 + \alpha\Gamma(x/r_C)^2$, where $\Gamma = \kappa\epsilon$ is proportional to the optical excitation rate associated with the maximal intensity of the doughnut κ, and ϵ is the

branching ratio of the spin changing ($m_s = 1 \rightarrow m_s = 0$) decay relative to the total decay of the excited state. $R_0 = \epsilon\kappa_0$ is proportional to the intensity at the doughnut center and the corresponding excitation κ_0. The spin-RESOLFT resolution r is defined by $f(x) = \exp(-\alpha(x/r)^2)$. Solving for r leads to (eq. 4.1). In our experiments, the resolution is limited by small imperfection of the doughnut-zero intensity. As shown in the Appendix C.2.1, using a model that includes a back pumping processes that brings the electronic spin from the $m_s = 0$ to the $m_s = 1$ state and finite spin lifetime, we find that the improvement in resolution relative to the diffraction limit of a confocal microscope is given by $r/r_C \sim \sqrt{R_0/\Gamma}\sqrt{1 + 2\gamma_{0\rightarrow 1}/R_0} \approx \sqrt{R_0/\Gamma}$, where $\gamma_{0\rightarrow 1}$ is the total rate out of the electronic spin state $m_s = 0$. This estimate is in good agreement with experimental observations.

4.5 Sub-wavelength optical magnetometry

To demonstrate simultaneous nanoscale spin imaging and magnetometry, we applied the spin-RESOLFT technique to NV centers in bulk diamond separated by less than the diffraction limit. Fig. 4.3a shows sub-diffraction 2D imaging of two NV centers with identical ESR lines. In this case, it is not possible to identify the presence of multiple centers using conventional confocal imaging and ESR techniques alone. However, by using our new technique, the presence of two NV centers separated by ∼150 nm is directly revealed in a 2D sub-diffraction spin image (Fig. 4.3b).

Detection of local magnetic fields with sub-diffraction resolution is presented in Figure 4.3c,d. Specifically, when imaged individually with spin-RESOLFT, each NV center exhibits a distinct modulation of its Rabi oscillation (Fig. 4.3c), determined by a relative

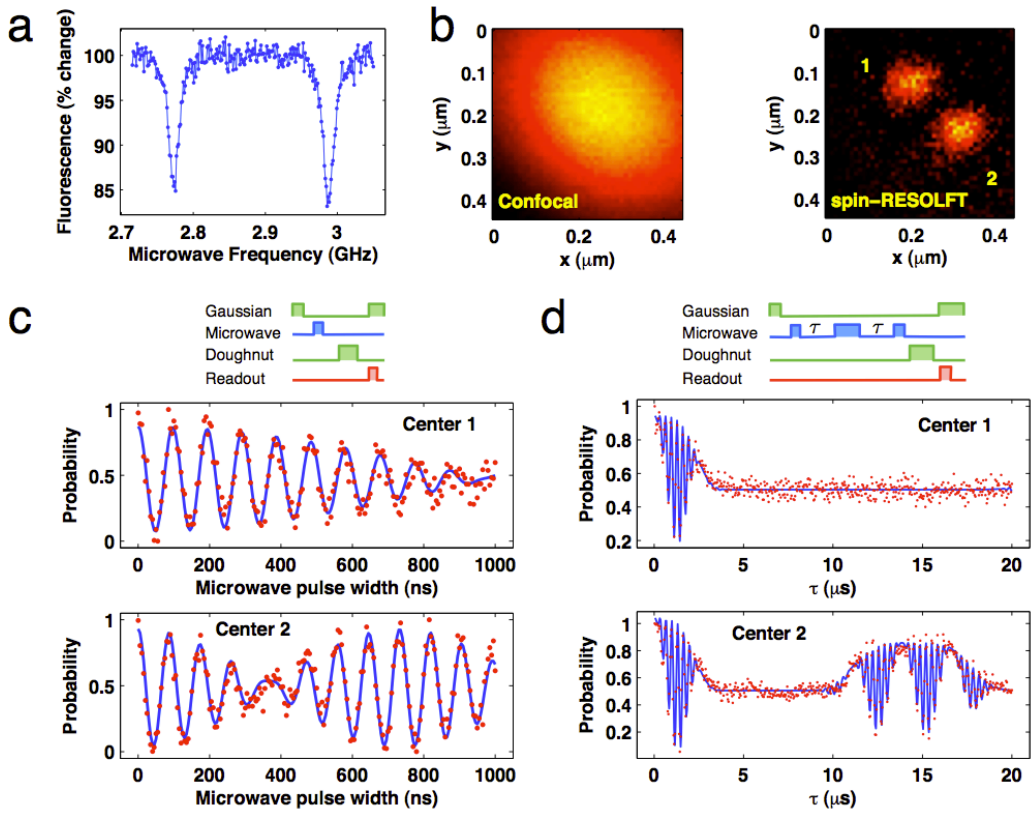

Figure 4.3: | **Sub-diffraction optical magnetic sensing. a**, Multiple NV centers cannot be identified or distinguished by their optically-detected ESR spectrum, acquired using confocal fluorescence microscopy. **b**, Confocal image does not resolve multiple NV centers; whereas 2D spin imaging using spin-RESOLFT reveals two NV centers separated by ∼150 nm. The image has 50 x 50 pixels, with a data acquisition time per pixel of 7.2 seconds. **c**, spin-RESOLFT provides spatially-selective measurements of Rabi oscillations for the two neighboring NV spins, which display stark differences due to different local magnetic field environments. **d**, spin-RESOLFT also enables spatially-selective spin-echo measurements for the two NV spins, which reveal substantial differences in spin coherence times, indicating the presence of magnetic impurities in the local environment of NV Center 1. Solid lines in **c** and **d** are fits to a model that includes the electronic spin of the NV center and the nuclear spin of the center's ^{15}N atom.

shift in the center's ESR transition frequency arising from small differences (< 1 G) in the static local magnetic field that each center experiences. Even more subtle differences in the local magnetic field environment of the two NV centers are revealed by sub-diffraction spin-echo measurements using spin-RESOLFT (Fig. 4.3d). While at short times each of the centers display spin echoes modulated by Larmor precession of the ^{15}N nuclei in the applied static magnetic field, at longer times the echo signals are substantially different. Center 2 displays good coherent dynamics, evidenced by echo revivals exceeding 20 μs, whereas Center 1 shows no echo revival, due to a nearby ^{13}C nucleus [125] or other magnetic defects (see Appendix C.2.2). When NV centers have different crystallographic axes and therefore different ESR spectra, the spin-RESOLFT technique can associate each spectral line with the corresponding location of an individual NV centers with sub-diffraction limited resolution (see Figure C.7).

4.6 Measurements of local magnetic field environment

The observed modulations of the Rabi oscillations shown in Fig. 4.3c reveal the different magnetic field experienced by each NV center. These modulations are caused by hyperfine-induced splitting in the NV electronic spin transition ($m_s = 0 \rightarrow 1$) associated with the ^{15}N nuclear spin ($I = \frac{1}{2}$). Such modulations appear when the microwave frequency is detuned from the central transition $\nu_0^i = \Delta + \gamma_e B^i$, where B^i is the magnetic field along the NV axis of center i , Δ is the zero-field splitting, and γ_e is the gyromagnetic ratio of the electronic spin. The modulation frequency for NV center i is thus given by (see Appendix C.2.2) $(\nu_0^i - \nu)A/\Omega$, where ν is the microwave frequency, $A = 3.05$ MHz is the hyperfine interaction between the electronic and nuclear spin and Ω is the Rabi frequency.

The difference in the beating frequencies of each center reveals a difference in effective static magnetic field experienced by each center of about 1 G.

In our spin echo measurements (Fig. 4.3d), the dominant contribution comes from the interaction between the electronic spin of the NV center and the ^{15}N nuclear spin and ^{13}C nuclear spin bath. The high frequency oscillations (3.05 MHz) correspond to the hyperfine interaction A between the electronic spin and nuclear spin of the ^{15}N atom in the NV center, as discussed above. Meanwhile the slow frequency component of the dynamics (360 kHz) corresponds to the Larmor frequency of the ^{15}N nuclear spin in the local magnetic field which is enhanced by virtual transitions of the electronic and nuclear spin (see Appendix C.2.2). The enhancement factor can be as large as $2(\gamma_e/\gamma_n)(A/\Delta) \approx 14$ when the magnetic field is perpendicular to the NV axis. The observed spin echo collapses and revivals are due to the interaction between NV centers and ^{13}C nuclei. The revival frequency in Fig. 4.3d, 74 kHz, is given by the bare Larmor frequency of ^{13}C corresponding to a magnetic field of 69 G (see Appendix C.2.2). Note that Center 1 shows no revival which is likely due to a proximal ^{13}C nuclear spins that quickly decoheres the electronic spin of this center [23].

4.7 Coherent spin control

The spin-RESOLFT technique also enables selective coherent manipulation of individual NV spins separated from other nearby NV centers by less than the diffraction limit. Applying a strong optical doughnut field simultaneously with a resonant microwave field (Fig. 4.4a) can suppress coherent spin transitions away from the laser intensity null.

We first demonstrated this effect for an individual, isolated NV center, initially polar-

ized into its $m_s = 0$ state. To distinguish the optical suppression of microwave-driven spin transitions from the conventional optical process used above for re-polarization, we exploited the fact that the optical pumping from $m_s = \pm 1$ into $m_s = 0$ occurs via transition through a metastable singlet state on a timescale of about $\tau_s = 300$ ns. Therefore, we applied a microwave π pulse driving the $|0\rangle \rightarrow |1\rangle$ transition together with a simultaneous pulse of the green laser beam; after which we immediately (within $\tau_d \leq 50$ ns $\ll \tau_s$) optically measured the populations in the $m_s = 0, \pm 1$ and metastable singlet states (see Appendix C.2.3). As shown in Fig. 4.4a, as we increased the laser power, the population in each state (triangles) approached the values measured when no microwave pulse was applied (open circles). This demonstrates that at high laser power no population transfer occurs between the $|0\rangle$ and $|1\rangle$ states. Since our experiment measured the populations before the metastable singlet could decay into the ground state $m_s = 0$, the data of Fig. 4.4a directly confirms that the observed inhibition of population transfer was not due to repumping out of the $|m_s| = 1$ states.

The observed population dynamics can be due to three effects, all of which result in a suppression of coherent spin manipulation by the applied microwave field. First, if an NV center is optically promoted to the electronic excited state, then the microwave transition between spin states with $m_s = 0$ and $m_s = 1$ is suppressed due to the different zero field splitting in the electronic ground and excited states. Second, if an NV center is transferred nonradiatively to the metastable $^1A_1$ state, then coherent spin rotations are prevented since the $^1A_1$ state is a spin singlet. Finally, optical excitation inhibits the build up of spin coherence between the $|0\rangle$ and $|1\rangle$ states even in the absence of population transfer to the excited state, a phenomena known as the quantum Zeno effect [74]. To estimate how substantially

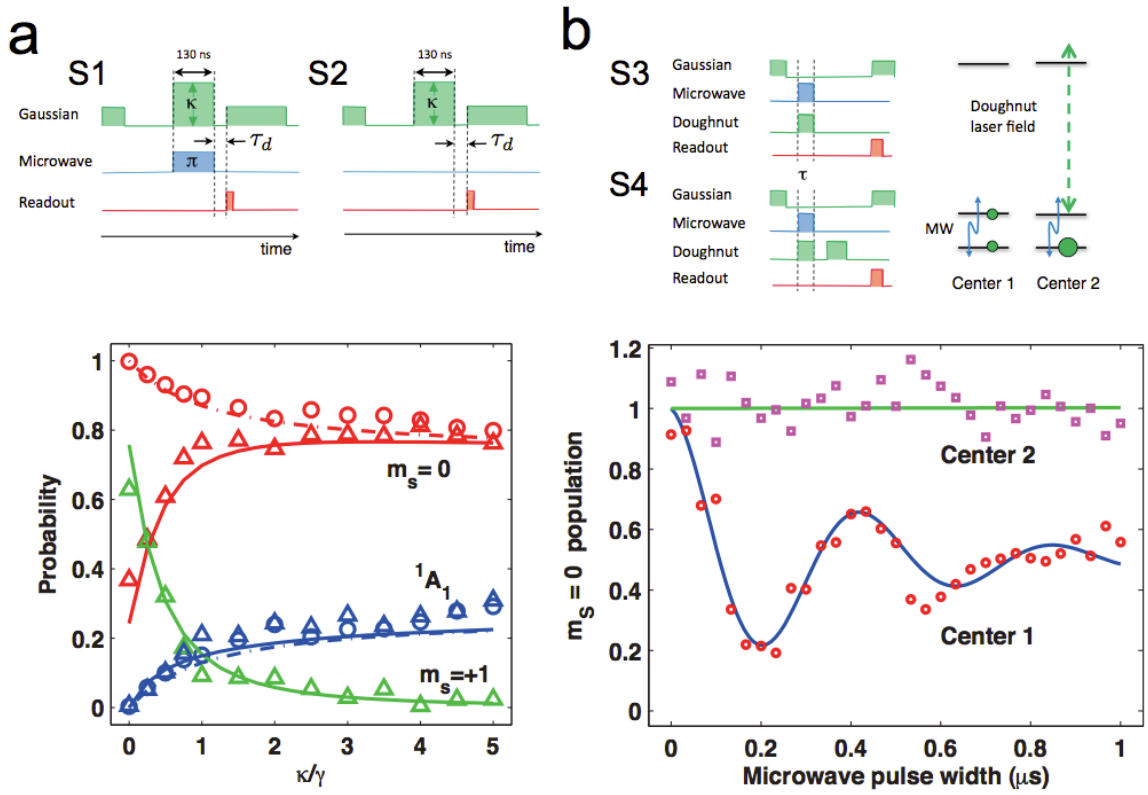

Figure 4.4: | **Sub-diffraction coherent manipulation of spectrally.** indistinguishable NV spins using optically-induced effects. **a**, Suppression of a single, isolated NV center's spin transitions, driven by a resonant microwave pulse, as a function of Gaussian laser beam power (characterized by the NV optical excitation rate, κ). Using sequences S1 and S2, the populations of the $m_s = 0$ state (red), $m_s = +1$ state (green), and $^1A_1$ state (blue) were measured with (triangles) and without (open circles) a resonant microwave π pulse of 130 ns duration, applied simultaneously with the Gaussian optical beam. The state populations were determined by recording the fluorescence right after microwave pulse application ($\tau_d < 50$ ns) and also after waiting for a time ($\tau_d = 5$ μs) much longer than the singlet deshelving time (300 ns). The comparison between these two measurements allows us to extract the populations of all states, including the singlet (see SI). Solid lines are fits using the master equation described in Ref. [32] and in the SI. **b**, Coherent spin transitions induced by resonant microwave radiation (MW) are inhibited for NV centers away from the central null of a simultaneously applied green doughnut beam. Selective Rabi oscillations are observed only for the NV spin in the doughnut null (Center 1); whereas NV Center 2, separated from Center 1 by 150 nm, is located outside the doughnut null, and is observed to remain in the ground state. Populations of Centers 1 and 2 are obtained from experimental sequences S3 and S4 as described in Appendix C.2.4.

each of these three processes contributes to the observed suppression of coherent spin transitions, we calculated the populations in the electronic excited state and in the $^1A_1$ state using the transition rates determined in Fig. 4.4a. As shown in Figure 4.6 for our experimental parameters ($R/\gamma \approx 1$), the estimated population in the ground state is of the same order as the sum of populations in the excited state and the singlet. Thus population transfer and the quantum Zeno effect contribute approximately equally to the observed suppression of coherent spin manipulation.

We next employed spin-RESOLFT for selective coherent manipulation of one of two closely spaced NV spins (Center 1 in Fig. 4.3b), while the other NV spin (Center 2) was kept in its $m_s = 0$ state via optically-induced suppression of coherent spin transitions, as discussed above. A pulsed strong doughnut beam was applied simultaneously with a microwave pulse of variable Rabi spin-flip angle, followed by optical measurement of the state of the NV spin at the doughnut center. In a separate calibration experiment, the states of both NV spins were measured together (no optical doughnut applied) as a function of microwave pulse length (Rabi spin-flip angle). The spin-RESOLFT and calibration measurements enabled us to determine the states of the two proximally spaced NV spins individually. Specifically, two experiments were performed. In one, the spin states of both NV centers were measured (sequence S3); in the second, the spin state of Center 1 was determined using spin-RESOLFT (sequence S4); see Appendix C.2.4 for details. As shown in Fig. 4.4b, spin transitions are inhibited for the NV center outside the central null of the doughnut beam; whereas the central NV spin undergoes coherent evolution, i.e., Rabi oscillations, in excellent agreement with a theoretical model (blue and green curves in Fig. 4.4b), as described in Appendix C.2.4.

4.8 Inhibition mechanism of electronic-spin rabi oscillations

In this section, we describe in detail the optical inhibition of electronic spin Rabi oscillations using a doughnut beam (Figure 4.4b). The basic idea can be explained by considering a simple two-level system (with states $|0\rangle$ and $|1\rangle$), which undergoes Rabi oscillations (with Rabi frequency Ω) and which is subject to an effective dephasing (with dephasing rate γ_p). The system dynamics is then governed by the Hamiltonian $H = -\frac{\Omega}{2}\sigma_x$ (where $\vec{\sigma}$ are Pauli matrices) combined with the decay of the off-diagonal matrix elements of the density matrix ρ with rate γ_p. Formally, this is described by the following master equation:

$$\frac{d\rho}{dt} = i\left[\frac{\Omega}{2}\sigma_x, \rho\right] - \frac{\gamma_p}{4}\left[\sigma_z, [\sigma_z, \rho]\right]. \tag{4.2}$$

Suppose the system starts in the $|0\rangle$ state, i.e., $P_0\left(t=0\right) = 1$. We analytically solve the master equation and obtain the probability of being in the $|0\rangle$ state as a function of time:

$$P_0\left(t\right) = \frac{1}{2}\left(1 + \frac{\Gamma_+ e^{-\Gamma_- t} - \Gamma_- e^{-\Gamma_+ t}}{\Gamma_+ - \Gamma_-}\right), \tag{4.3}$$

where $\Gamma_\pm = \frac{1}{2}\left(\gamma_p \pm \sqrt{\gamma_p^2 - 4\Omega^2}\right)$. We may also use the approximate form:

$$P_0\left(t\right) \approx \begin{cases} \frac{1}{2}\left(1 + \cos\left(\Omega t\right) e^{-\gamma_p t/2}\right) & \text{, for } \Omega \gg \gamma_p \\ \frac{1}{2}\left(1 + \exp\left(-\frac{\Omega^2}{\gamma_p} t\right)\right) & \text{, for } \Omega \ll \gamma_p. \end{cases} \tag{4.4}$$

For $\Omega \gg \gamma_p$, the two-level system undergoes Rabi oscillations with an amplitude decay rate $\gamma_p/2$. This scenario approximately describes the evolution of Center 1 (blue curve in Figure 4.4b): there the amplitude decay comes from a combination of T_2^* decay and of the dephasing due to the imperfect zero of the doughnut. On the other hand, for $\Omega \ll \gamma_p$,

the oscillation dynamics is inhibited, and the system remains in the initial state $|0\rangle$ with a slow spin-relaxation rate Ω^2/γ_p, which is inversely proportional to γ_p. This scenario, which we refer to as a quantum Zeno-like effect [74], approximately describes the evolution of Center 2 (green curve in Figure 4.4). In particular, the scheme succeeds if the spin-relaxation rate in Center 2 over the course of a π-pulse on Center 1 is much less than unity: $1 - P_0(t) \approx (1/2)(\Omega^2/\gamma_p) * (\pi/\Omega) = \pi\Omega/(2\gamma_p) \ll 1$. In other words, for times $t \ll \gamma_p/\Omega^2$ the center is "frozen" in the ground state.

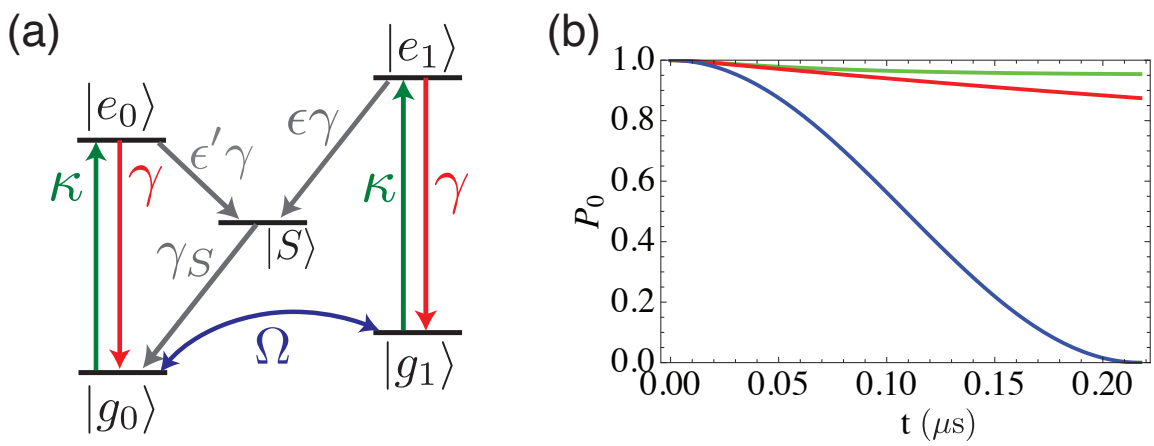

Figure 4.5: | **a, 5-level system used to model inhibition of electronic-spin Rabi oscillations.** $\gamma \approx 1/(13\text{ ns}) = (2\pi)12.2$ MHz, $\gamma_S \approx 1/(300\text{ ns})$, and $\Omega = (2\pi)2.3$ MHz. **b,** Calculated inhibition of electronic-spin Rabi oscillations: the blue curve has $\kappa = 0$ and shows an uninhibited Rabi π-pulse (analogous to Center 1 evolution shown as the blue curve in Figure 4.4b); the green (red) curve has $\kappa = \gamma$ and $\epsilon = 0.3$ ($\epsilon = 0$), $\epsilon' = 0$ and demonstrates the inhibition of the Rabi oscillations. The green curve is analogous to Center 2 evolution shown as the green curve in Figure 4.4b. The fact that the red curve stays close to 1 confirms that the quantum Zeno-like effect due to dephasing (and not the optical pumping from $|g_1\rangle$ to $|g_0\rangle$) plays a dominant role in suppressing Rabi oscillations of Center 2. The value (here ≈ 0.9) of the red curve at the final time π/Ω can be used as a rough estimate of preservation of nuclear spin coherence on Center 2 in future experiments.

In reality, the experimental situation is more complicated than this simple two-level model. Specifically, we must account for processes in which the spin is first flipped to

state $|1\rangle$ and subsequently repolarized to state $|0\rangle$. We therefore model the experiment by considering the five-level system shown in Figure 4.5a. The five states are the ground states $|g_0\rangle$ with $m_s = 0$ and $|g_1\rangle$ with $m_s = 1$, the excited states $|e_0\rangle$ with $m_s = 0$ and $|e_1\rangle$ with $m_s = 1$, as well as the singlet $|S\rangle$. In addition to the coherent evolution with Rabi frequency Ω, the system is subject to incoherent excitation (caused by the green laser) from the ground to the excited states with rate κ. Moreover, the excited states decay down to the triplet with rate $\gamma \approx 1/(13\text{ ns}) = (2\pi)12.2$ MHz [126]. At the same time, the state $|e_1\rangle$ decays down to the singlet with rate $\epsilon\gamma$, where we take $\epsilon = 0.3$, while the singlet decays to $|g_0\rangle$ with rate $\gamma_S \approx 1/(300\text{ ns})$. After extracting $\Omega = (2\pi)2.3$ MHz from the uninhibited Rabi oscillations of Center 1 (Figure 4.4b) and $\kappa \approx \gamma$ (on Center 2) from the fluorescence saturation curve (not shown), we know all the parameters and can compute the resulting evolution of Center 2 over time π/Ω, which is sufficient for a π pulse on the uninhibited Center 1. We begin with Center 2 in the state $|g_0\rangle$, keep the microwave and the green light on for time t, then allow the population to relax to $|g_0\rangle$ and $|g_1\rangle$, and plot in green in Figure 4.5b the resulting population P_0 of $|g_0\rangle$ for Center 2 as a function of t. In agreement with the green curve in Figure 4.4b, we see that the population stays within a few percent of the initial population of unity, while Center 1 (with $\kappa \approx 0$) does a Rabi π pulse (blue curve). The reason why the blue curve in Figure 4.4b does not show a perfect π-pulse is because the doughnut zero is imperfect and because T_2^* is finite.

To confirm that the observed inhibition indeed comes largely from Zeno-like effects and not from re-pumping of the electronic spin from $|g_1\rangle$ to $|g_0\rangle$ via the singlet, we plot in red in Figure 4.5b the equivalent of the green curve except with $\epsilon = 0$, i.e. we turn off the $|g_1\rangle \rightarrow |g_0\rangle$ pumping process. We observe that the population still stays mostly in

$|g_0\rangle$, confirming that it is indeed Zeno-like dynamics that are largely responsible for the inhibition. In fact, for our parameters ($\kappa \gg \Omega$), the red curve has a simple analytical form

$$P_0(t) = \frac{1}{2}\left(1 + e^{-\frac{\gamma}{\kappa+\gamma}\frac{\Omega^2}{\kappa}t}\right). \tag{4.5}$$

Since both $|g_0\rangle$ and $|g_1\rangle$ are excited with rate κ, the coherence between these two levels decays with rate κ, so κ plays the role of the dephasing rate γ_p from our two-level model above. The prefactor $\gamma/(\kappa+\gamma)$ in front of Ω^2/κ is the population that is in the ground state triplet, while the remainder is in the excited state and is unaffected by Ω since the corresponding transition in the excited state is highly off-resonant (and was, thus, not included in the model). Under this approximation, the transition probability for Center 2 over time π/Ω is $1-P_0(t) \approx [\gamma/(\kappa+\gamma)][\pi\Omega/(2\kappa)]$, which for our parameters is ≈ 0.1, which is much smaller than unity, as desired. This value can be further reduced by going to larger green laser powers or smaller Rabi frequencies. In addition, if strain and an off-axis magnetic field are included, population transfer from $|e_0\rangle$ to the singlet ${}^1A_1$ is possible, allowing a further suppression of coherent spin manipulation via the microwave field.

In Figure 4.4a we verify this suppression experimentally by studying a single isolated NV center using the pulse sequences S1 and S2. Our analysis requires knowledge of the populations ($\rho_{0,0}$, $\rho_{1,1}$, $\rho_{S,S}$) of the $m_s = 0$, $m_s = \pm 1$ and ${}^1A_1$ manifolds right after state preparation. To determine these quantities, we record the fluorescence f

$$f(\tau_d) = f^0\rho_{0,0}(\tau_d) + f^1\rho_{1,1}(\tau_d)$$

of a single NV center for two different times $\tau_d \ll T_S$ and $\tau_d \gg T_S$; where τ_d is the time defined in S1 and S2 of Figure 4.4a; $T_S = 300$ ns is the lifetime of the singlet ${}^1A_1$; and f^{m_S} are the fluorescence rates for the corresponding states, which can be determined

experimentally. Since the singlet ${}^1A_1$ nearly always decays non-radiatively into the $m_s = 0$ state [126] we can extract the populations $\rho_{i,i}$, which are shown in Figure 4.4a, from measuring the fluorescence at $\tau_d \ll T_S$ and $\tau_d \gg T_S$ and using the relation $\rho_{0,0} + \rho_{1,1} + \rho_{S,S} = 1$.

To investigate the mechanism for the observed inhibition of coherent spin transitions in the presence of a resonant microwave field, we fit the extracted population of the $m_s = 0$, $m_s = 1$ manifold and ${}^1A_1$ state to the solution of a master equation, which additionally includes the hyperfine levels of ${}^{15}N$. The fit parameters include the optical excitation rate κ, the branching ratio ϵ from the $|e_1\rangle$ to the ${}^1A_1$ state, and the branching ratio ϵ' from the $|e_0\rangle$ to the ${}^1A_1$ state.

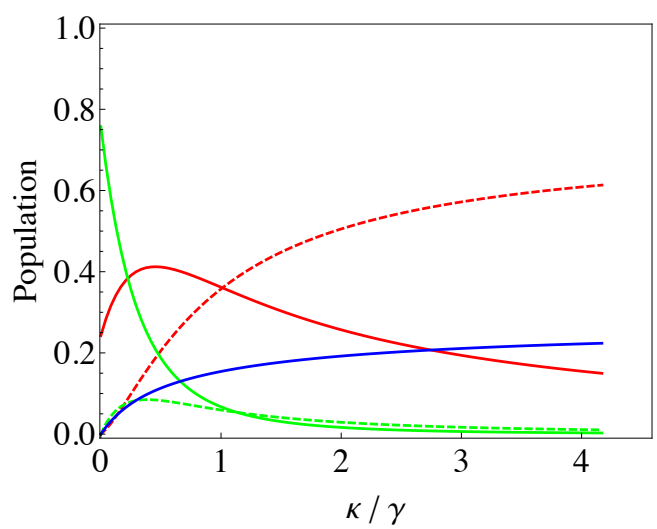

Figure 4.6: | **Estimated population** in the $|g_0\rangle$ (solid red), $|e_0\rangle$ (dashed red), $|g_1\rangle$ (solid green), $|e_1\rangle$ (dashed green) and ${}^1A_1$ (blue) state as a function of optical excitation power. The calculations are based on the master equation found in Figure 4.5a.

To evaluate the individual contribution for each of these three effects, we calculate the population in $|g_0\rangle$, $|e_0\rangle$, and ${}^1A_1$ using the transition rates found in Figure 4.4a, which are

shown in Figure 4.6. From this calculation, we conclude that inhibition of spin transitions at large optical pumping powers is mainly due to population hiding in the $|e_0\rangle$ state; while suppression at small optical pumping is mostly caused by the quantum Zeno effect. For the typical parameters of our experiment (Figure 4.4b), both effects contribute to the suppression of coherent spin transitions.

One eventual goal of this demonstrated inhibition is to allow quantum information stored in a nuclear spin degree of freedom (coming from the nitrogen or a nearby carbon-13) to be controllably manipulated in each NV center. Provided that the electron state of the illuminated NV center (Center 2) is kept in $|m_s = 0\rangle$, the state of the corresponding nuclear spin would be preserved [67], while the nuclear spin associated with Center 1 can be prepared, coherently manipulated, or detected with sub-wavelength resolution. The performance of this technique can be directly evaluated from our measurements. Specifically, the error induced on the nuclear spin associated with illuminated Center 2 is proportional to $1 - P_0 \approx 0.1 \ll 1$. This small error indicates that the state of the nuclear spin associated with Center 2 can be well preserved while we manipulate Center 1.

4.9 Conclusions and outlook

As shown in these demonstration experiments, the far-field optical resolution for spin imaging and coherent manipulation is no longer limited by diffraction. We expect the resolution and speed of the spin-RESOLFT technique to be significantly improved by technical upgrades such as increasing the contrast between the intensity of the doughnut crest and that of the central minimum, i.e., perfecting the doughnut zero [122]. In addition, implementing relatively large values of Γt_D, where $\Gamma \sim 100$ MHz near optical saturation and t_D

is on the order of the electronic spin lifetime T_1 (which ranges from 10 ms [63] to longer than a second in ultrapure diamond [72]), should allow more than a 1000 fold improvement of resolution below the diffraction barrier, making it feasible to attain sub-nanometer optical spin detection and manipulation, including sensitive measurement of magnetic fields. Finally, the low levels of light required for our technique will also facilitate the parallelization of this imaging process by replacing the scanning doughnut beam with moving arrays of lines or doughnuts of vanishing intensity. This modification should enable fast camera-based spin imaging over a large field of view.

The capability to optically detect and manipulate individual spins with sub-diffraction resolution opens the door to a number of powerful applications in both the physical and life sciences. For example, spin-RESOLFT could be used for high fidelity addressing of individual spin qubits in an array composed from NV centers separated by distances in the range of 10-30 nm. In such a case, nearby electronic spins could be coupled directly via magnetic or optical dipole-dipole interactions, thereby enabling high fidelity two-qubit operations. By encoding qubits into nuclear spins nearby to specific NV centers, and using spin-RESOLFT for sub-diffraction addressing of electronic spins and control of electron-nuclear systems, both readout and coherent manipulation could be enabled on nanometer scales, thereby opening a new route to a room temperature scalable quantum information processor (a more detailed discussion of this approach can be found in Appendix B). More specifically, the demonstrated suppression of electronic Rabi oscillations (Fig. 4.4b) allows for preparation, detection, and coherent manipulation of one nuclear spin (associated with the NV center in the zero of the green doughnut-shaped beam) without affecting qubits encoded in the nuclear spins of surrounding centers [67, 81]. Likewise, intriguing

applications in bioscience can be foreseen for spin-RESOLFT, which combines high sensitivity magnetometry with sub-diffraction imaging resolution. Examples include the use of NV-diamond nanocrystals in living cells as photostable fluorescent biomarkers and sensors of nanoscale magnetic fields, e.g., for direct imaging of activity in neuronal networks and mapping the local concentration of reactive oxygen species and intra-cellular ions. In addition, by exploiting long-lived ground electronic spin states, spin-RESOLFT has the potential for reaching extraordinary imaging and sensing resolution with modest laser power levels, which may be of interest for a diversity of super-resolution imaging applications involving, in particular, biological systems. Finally, we expect that our approach can be applicable to a wide variety of spin systems, from trapped atoms and ions [127] to quantum dots, which may enable a diverse range of interesting applications in quantum science and engineering.

Chapter 5

Conclusions and Outlook

The precise control of quantum systems is an extraordinary challenge that often requires elaborate experimental techniques. In this thesis I presented an alternative approach to quantum information and quantum metrology based on the manipulation of spins in diamond at room temperature. The techniques that I described rely on both state of the art optical and microwave control of the electronic and nuclear spin associated with NV centers. By precisely understanding the Hamiltonian of our system we were able to utilized quantum control to accurately tailor interactions between our spin and the environment. Specifically, using a dissipative optical effect in combination with dynamical decoupling we were able to isolate the NV spin from external perturbations with unprecedented accuracy allowing us to protect a NV quantum register for seconds from decoherence. On the other hand, by tailoring the decoupling sequence such that the evolution of the NV spin is insensitive to external magnetic fields but remains sensitive to local temperature, it was possible to realize a bio-compatiable nanoscale temperature sensor of unparalleled accuracy. Moreover, combining the optical polarization properties of the NV with a Laguerre-

Gaussian mode enabled the imaging of individual spins with a resolutions well below the optical diffraction limit. In addition, saturation of the optical transition in combination with the 'quantum Zeno' effect further enabled us to coherently manipulate selected spins in an ensemble of nominally indistinguishable spins with nanoscale resolution.

5.1 Room-temperature quantum bit memory exceeding one second

The experiments presented in Chapter 2 of this thesis demonstrate multi second storage times for quantum information at room temperature as well as high fidelity spin readout. This approach is based on an efficient decoupling of the memory nuclear spin from the control electronic spin by optically induced motional averaging combined with dynamical decouple to suppress homonuclear dipole-dipole interactions in the bath.

High fidelity readout of a qubit is central to many quantum error correction schemes and hence the realization of a scalable quantum information processor architecture. While in this work we have demonstrated readout fidelities above 90% simple technical improvements should in principle allow for a further increase beyond the threshold required for quantum error correction [128]. Specifically, measurement induced nuclear spin flips could be completely eliminated by alignment of the external magnetic field parallel to the effective magnetic field induced by hyperfine interactions. Even in the case of imperfect alignment a simple increase in the external magnetic field or a reduction of the hyperfine interaction will quadratically reduces the nuclear depolarization rate. Additionally, coherent flips between the memory and other ^{13}C spins can be reduced by further diluting the

^{13}C spin bath or increasing the number of MREV decoupling pulses. Finally nuclear depolarization can be further suppressed by enhancing the ionization rate though an increase of the laser intensity. Eventually the ^{13}C nuclear depolarization rate will be limited by spin lattice relaxation, which has been found in bulk NMR measurements to exceed 36 h.

Being able to preserve quantum information on a time scale of seconds is instrumental to many quantum communication and computation proposals relying on NV centers. NV based quantum repeaters are one particular example where long storage times are esential. Unfortunately, most practically realizable NV quantum repeaters suffer from low bit rates and hence require storage times on the order of seconds. The results demonstrated here combined with current state of the art NV-photon entanglement schemes pave the way towards a first realization of quantum networks. Another inspiring potential application for a long lived room temperature quantum memory is the implementation of 'quantum money', a pioneering concept introduced by Stephen Wiesner in 1970 that marks the beginning of quantum encryption. Of course for such an application a further improvement in coherence is required.

Finally, a long lived room temperature quantum memory could also facilitate the development of a NV based room temperature quantum computer. While there are many different routes towards this goal (some of which have been described in this thesis), they all benefit from a long-lived quantum memory. One particular proposed architecture that crucially relies on such a memory utilizes a shallow implanted array of individual NV-qubits in a bulk diamond. The spacing in such a NV array can be a few hundred nanometers enabling optical readout of the individual NV centers. Two qubit operations between distanced NV centers (defined as qubit-A and B) can be performed by mediation over a third NV center

attached to an AFM-tip. In this specific protocol, the AFM is first brought into proximity with qubit-A, which is then swapped via magnetic dipole-dipole interaction with the NV center attached to the AFM. By moving the tip to the location of qubit-B a two-qubit gate can be performed again meditated by dipole-dipole interaction. Finally, by moving the AFM back to the first position, qubit-A can be stored back in the initial NV register. Since this process requires time consuming movements of an AFM tip, long qubit storage times are essential.

In this thesis, the demonstrated spin coherence times are well beyond one second promoting NV centers as a competitive qubit with storage times comparable to those of trapped ions. An additional increase of the coherence time beyond the second regime could potentially be achieved by further reducing the hyperfine interaction, prolonging T_2 quadratically. Similarly, a linear extension of the coherence time can be achieved by increasing the ionization rate. A different approach that scales even more favorably than laser induced motional averaging relies on dynamical decoupling of the electronic from the nuclear spin.

5.2 Nanometer scale thermometry in a living cell

While NV centers have been hailed as a powerful nanoscaled magnetic field sensor, we showed in Chapter 3 that they are also exceptional nanoscale thermometers. Our approach relies on the temperature dependence of the NV's spin transition and the ability to employ quantum control for an accurately measurement of this transition frequency. This spectroscopic approach makes use of a novel dynamical decoupling sequence that eliminates quasi-static magnetic field fluctuations but remains highly sensitive to the exact value of the zero-field splitting.

One of the interesting aspects of our NV based thermometer is the capability of measuring temperature over a large range, approximately from 200 to 600 K. The ability to measure temperature over such a wide range might be of great interest for the design of integrated electronic circuits as heat dissipation on sub-micrometer length scales is often a limiting factor in their performance. By placing individual nanodiamonds at different locations of interest, temperature could be recorded at several points simultaneously, giving this approach a competitive advantage over conventional scanning thermometry microscopy where only one point at a time can be investigated.

Yet, another exceptional aspect of our technique to nanoscale thermometry is the insensitivity of our device to the local chemical environment. This combined with the large covered temperature range of our sensor might enable the nanoscale calorimetric studies, which could be of great interest for the study of heterogenous exothermic chemical reactions. To investigate dynamics on faster time scales the sensitivity needs to be augmented from 10 mK/$\sqrt{\text{Hz}}$ to μK/$\sqrt{\text{Hz}}$ by resorting to larger numbers of NV centers with longer coherence times or spin squeezed states [6].

As demonstrated in Chapter 3.3 a sub-micrometer scale temperature profiles can be accurately controlled by combining our temperature sensors with the local laser induced heating of gold nanostructures. Since the kinetics of chemical reactions are strongly dependent on temperature it is possible to use our temperature control technique to tailor chemical reactions at a nanoscale. In a proof-of-principle experiment ohmic heating of lithographically fabricated nano structures has been employed to induce the growth of ZnO nano-wires with spatial resolution below 100 nm [99, 104].

The bio-compatibility of this technique is another appealing aspect of nanodiamond

based sensing. In Chapter 3.3 we have demonstrated that nanodiamonds can be inject into the cytosol of living cells. Due to the small size and the chemical inertness of the nanodiamonds this process leaves the cells mainly unharmed.

One obvious application of nanoscale temperature sensing in biological cells is the measurement of local metabolic activities in a single cell. This could provide a new powerful tool for biologists interested in studying questions related to mitochondrial activities [129, 130]. On a larger scale, this technique could also be employed to investigate the structure of tumors. Specifically, tumors are known to be heterogeneous structures and it is believed that spatially different areas of a tumor exhibit different activity. This local differences in activity could then be mapped by measuring variations in temperature and hence the metabolic rates. While this is a very intriguing application for any meaningful measurements an improvement in absolute temperature sensitivity is required. Such a boost in absolute sensitivity could be achieved by resorting to low strain nanodiamonds or by reading out a large ensemble of diamonds opposed to a single ones. Finally, NV imaging can readily be combined with two photon absorption microscopy [107, 108].

Utilizing temperature control may also benefit the study of larger biological systems. For example, Caenorhabditis elegans (C. elegans), a microscopic worm, is a model organism for a variety of different developmental biological questions. Specifically, in an early developmental phase the cell division cycles in C. elegans eggs are highly synchronized. Moreover, the rate at which the cell dividison occurs is strongly temperature dependent. Yet, it is not known what feedback mechanism coordinates the synchronization of this cell division [131]. Using our technique it is possible to locally increase the temperature of a single cell while leaving the other cells at a lower unaltered temperature. We may then in-

fer whether there is a distinct cell that synchronizes the division of the other cells, whether there is a majority voting between the cells or any other mechanism by measuring the cell division rate as a function of local heating.

Finally, the combination of laser heating and an accurate temperature measurement might open the door towards an approach for cancer treatment. This might be of great interest when minimizing damage to nearby health tissue is essential. The here developed technique can help to ensure that healthy tissue surrounding the cancer is not heated above a harmful level, while the cancer cells them self are thermally ablated. First clinical trails using laser induced thermal ablated for the treatment of breast cancer are currently underway [88, 89, 90, 109].

5.3 Far-field optical imaging and manipulation of individual spins with nanoscale resolution

Chapter 4 of this thesis discussed a novel optical far-field technique that enables spin detection with nanometer resolution. Our sub-diffraction imaging technique relies on the non-linear saturation properties of NV centers in combination with a Laguerre-Gaussian mode. Using this approach, imaging resolution has been achieved that is comparable to those reached by conventional Stimulated Emission Depletion (STED) microscopy but at several order of magnitudes smaller power levels. The key is a combination of efficient optical pumping of the NV spin and a long intrinsic spin T_1-time. Such low intensities are crucial for many applications in imaging of biological cells where photo toxicity may hamper the use of traditional STED. Specifically, with the development of smaller nanodi-

amonds that contain photostable NV centers, NV based labeling might become a competitive alternative to quantum dot based techniques further promoting NV super-resolution microscopy.

As demonstrated in this thesis, it is further possible to combine our sub-diffractional imaging technique with nanoscale magnetic field sensing, which is of great importance for both in-vivo and in-vitro measurements. Delivering nanodiamonds into living cells and subsequently measuring magnetic field noise offers an alternative approach for the characterization of local chemical concentrations like paramagnetic oxygen with nanoscale resolution (Fig. 5.1).

Nanoscale field sensing can also be used for the structural analysis of macromolecules. Here the idea is that, for example, the structure of a protein can be inferred by sensing the exact spatial position of different nuclear spins within a single protein. Each individual nuclear spin can be localized by measuring the hyperfine interaction between the nuclear spin and different NV centers at different locations. Since the dipolar field of a nuclear spin falls off with the third power of the distance the NV centers need to be localized within less than a few nanometers separation from the nuclear spin of interest. Such an approach would require resolution for NV imaging in the nanometer range, which could possibly be accomplished with our technique (see Fig 5.1).

Finally, by combining our nanoscale spin imaging technique with NV based temperature sensing both nanoscale magnetic mapping and temperature measurements are possible. For this it is of particular importance that nanoscale imaging can be achieved at low laser power to reduce systematic errors due to laser heating of the specimen.

In Chapter 4.7 of this thesis we also introduced a new method that allows for the ma-

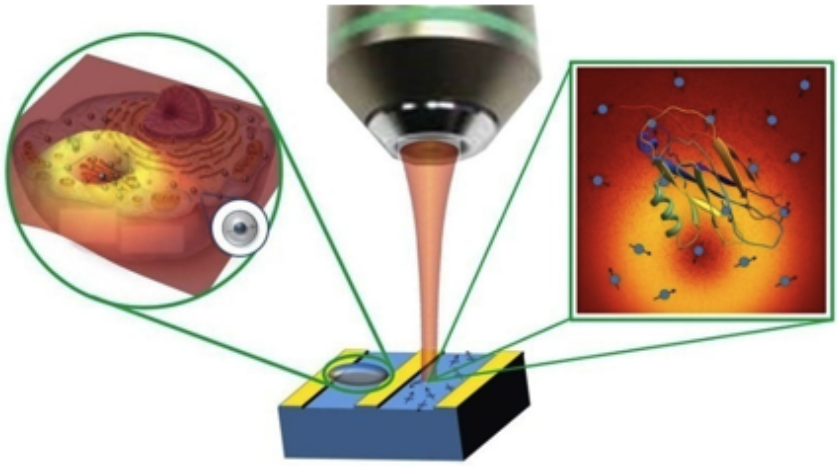

Figure 5.1: | **Nanoscale magnetic field sensing.** Schematic image describing magnetic field sensing combined with STED for measurement of molecular concentrations in living cells (left inset) as well as structural analysis of single proteins (right inset). The yellow areas represents a coplanar waveguide for microwave manipulation of the NV spin. The blue box represents a bulk diamond that hosts the NV centers used for the measurements in the right inset.

nipulation of individual NV centers without inducing evolution on other nominally identical nearby spins. Our approach bases on the suppression of coherent evolution of these nearby NV spins by illuminating them with a strong optical field combined with a Laguerre-Gaussian laser mode. The physical mechanism of this suppression is related to the 'quantum Zeno effect' and efficiently prevents the electronic spin from undergoing a transition from m_s=0 to m_s=$\pm$1. Utilizing the NV center as a quantum register with the electronic spin as control and the nuclear spin as memory qubit we can use our sub-diffractional spin control technique for quantum informations processing. This architecture makes use of a densely spaced two dimensional array of NV registers ($\sim$ 20 nm) that are coupled with each other via magnetic dipole-dipole interaction. In order to perform single or two qubit manipulation on a subset of the NV registers our technique can be utilized to transfer in-

formation from the nuclear spins to the electronic spin only for the selected NV centers while leaving the other spins untouched. Once the quantum information is transferred to the electronic spin it can be manipulated with global microwave pulses and coupled to other NV electronic spins by magnetic dipole interaction. To ensure high fidelity control of the electronic spin for NV separations of a few tens of nanometers it is necessary to achieve imperfections in the Laguerre-Gaussian mode that have an intensity minima to maxima ratio smaller than 10^{-5}, which is within the experimentally possible limitations. Improvements in the mode quality can further be achieved by making use of adaptive optics to correct for aberrations. Finally, bright decay of the nuclear spin associated with optical illumination can be reduced by simultaneously illuminate all the NV centers with an optical beam at 750 nm for depletion of the excited state.

Appendix A

Repetitive Readout of a Single Electronic Spin via Quantum Logic with Nuclear Spin Ancillae

A.1 Introduction

Robust readout of single quantum information processors plays a key role in the realization of quantum computation and communication as well as in quantum metrology and sensing. We implement a method for the improved readout of single spins in solid state systems. We make use of quantum logic operations on a system composed of a single electronic spin and several proximal nuclear spin ancillae to repetitively readout the state of the electronic spin. Using coherent manipulation of a single nitrogen vacancy (NV) center in room temperature diamond, full quantum control of an electronic-nuclear system composed of up to three spins is demonstrated. We take advantage of a single nuclear spin

memory to obtain a ten-fold enhancement in the signal amplitude of the electronic spin readout. Finally, we demonstrate a two-level, concatenated procedure to improve the readout using a pair of nuclear spin ancillae, representing an important step towards realization of robust quantum information processors using electronic and nuclear spin qubits. Our technique can be used to improve the sensitivity and the speed of spin-based nanoscale diamond magnetometers.

Efforts have recently been directed towards the manipulation of several qubits in quantum systems, ranging from isolated atoms and ions to solid-state quantum bits [132, 28]. These small-scale quantum systems have been successfully used for proof-of-concept demonstrations of simple quantum algorithms [133, 134, 15, 135]. In addition, they can be used for potentially important practical applications in areas such as quantum metrology [132]. For example, techniques involving quantum logic operations on several trapped ions have been applied to develop an improved ion state readout scheme, resulting in a new class of atomic clocks [136, 137]. We demonstrate a similar technique to enhance the readout of a single electronic spin in the solid state.

Our method makes use of quantum logic between a single electronic spin and nuclear spin qubits in its local environment for repetitive readout. While such nuclear spins are generally the source of unwanted decoherence in the solid-state, recent theoretical [138, 139, 140] and experimental [141, 63, 68, 123, 142, 143, 144] work has demonstrated that when properly controlled, the nuclear environment can become a very useful resource, in particular, for long-term quantum memory.

Our experimental demonstration makes use of a single negatively-charged nitrogen-vacancy (NV) center in diamond. The electronic ground state of this defect is an electronic

spin triplet ($S = 1$) and is a good candidate for a logic qubit, on account of its remarkably long coherence times [72] and fast spin manipulation using microwave fields [145]. Furthermore, the center can be optically spin polarized and measured by combining confocal microscopy techniques with spin-selective rates of fluorescence [141]. In practice, the NV spin readout under ambient, room temperature conditions is far from perfect. This is because laser radiation at 532 nm for readout re-polarizes the electronic spin before a sufficient number of photons can be scattered for the state to be reliably determined.

A.2 Quantum logic for improved readout fidelity

Our approach is to correlate the electronic spin logic qubit with nearby nuclear spins [146], which are relatively unperturbed by the optical readout, prior to the measurement process [67]. Specifically, we use one or more ^{13}C ($I = 1/2$) nuclear spins in the diamond lattice, coupled to the NV electronic spin via a hyperfine interaction, as memory ancillae qubits. For example, a single ^{13}C nuclear spin has eigenstates $|\uparrow\rangle_{n_1}$ (aligned) or $|\downarrow\rangle_{n_1}$ (anti-aligned) with the local magnetic field. The composite electronic-nuclear system is first prepared in a fiducial state, $|0\rangle_e|\downarrow\rangle_{n_1}$, using a sequence of optical, microwave and radiofrequency (RF) pulses. Next, the electronic spin is prepared in an arbitrary state $|\Psi\rangle_e = \alpha|0\rangle_e + \beta|1\rangle_e$, where $|0,1\rangle_e$ denote electronic state with $m_s = 0, 1$. Before readout, we perform a sequence of gate operations resulting in the entangled electron-nuclear state $|\Psi\rangle_e\,|\downarrow\rangle_{n_1} \rightarrow \alpha\,|0\rangle_e\,|\downarrow\rangle_{n_1} + \beta\,|1\rangle_e\,|\uparrow\rangle_{n_1}$. The optical measurement process projects this state into either $|0\rangle_e\,|\downarrow\rangle_{n_1}$ or $|1\rangle_e\,|\uparrow\rangle_{n_1}$. When optically excited these two states fluoresce at different rates dependent on the value of m_S. Within a typical measurement period, less than one photon is counted before the electron spin is repolarized to $|0\rangle_e$, which indicates

that the uncertainty of the electronic spin state measurement is quite large.

The nuclear spin can thus reveal the former electronic state because of the correlations established before the electronic spin was reset. To achieve this repetitive readout, we perform a controlled-not operation, which maps $|0\rangle_e |\downarrow\rangle_{n_1} \rightarrow |0\rangle_e |\downarrow\rangle_{n_1}$ and $|0\rangle_e |\uparrow\rangle_{n_1} \rightarrow |1\rangle_e |\uparrow\rangle_{n_1}$, and repeat the optical measurement. Fluorescence counting of these two states can be added to prior measurements to decrease the uncertainty for electronic spin state discrimination. If optical readout does not destroy the orientation of the nuclear spin, the uncertainty in the determination of the electronic spin can be reduced via repetitive measurements. In this way the overall signal-to-noise of the measurement process of our logic qubit can be increased. After multiple readout cycles and many quantum logic operations, the nuclear spin orientation will finally be destroyed. However, it is possible to further improve the readout scheme by using a pair of ancillary nuclear spins and imprinting the electronic state into a GHZ-like state $|\Psi\rangle_e |\downarrow\rangle_{n_1} |\downarrow\rangle_{n_2} \rightarrow \alpha |0\rangle_e |\downarrow\rangle_{n_1} |\downarrow\rangle_{n_2} + \beta |1\rangle_e |\uparrow\rangle_{n_1} |\uparrow\rangle_{n_2}$. In such a case, the state of the first nuclear spin after repetitive readout sequences can be periodically "refreshed" using the information stored within the second nuclear spin. These schemes are closely related to a quantum non-demolition (QND) measurement [147, 148], as the nuclear spin population operators $\hat{I}_z^{n1,n2}$ do not evolve throughout the electronic spin readout and constitute "good" QND observables. While imperfect optical NV electronic spin detection precludes an ideal QND measurement, our scheme nevertheless allows substantial improvement in the spin readout.

To implement the repetitive readout technique we use a single NV center in diamond coupled to nearby ^{13}C nuclear spins. These nuclear spins can be polarized, fully controlled and provide a robust quantum memory even in the presence of optical radiation necessary

for electronic spin-state readout [63, 67]. This is achieved through a combination of optical, microwave, and RF fields (Fig. A.1).

To control a single nuclear spin, we choose a NV center with a well-resolved ^{13}C hyperfine coupling near 14 MHz. The degeneracy of the $|m_s = \pm 1\rangle_e$ spin states is lifted by applying a $B_0 = 30$ gauss magnetic field along the NV axis. Under these conditions, the transitions of the electronic spin (**e**) within the subspace of $\{|0\rangle_e, |1\rangle_e\}$ can be selectively addressed, conditioned on a certain nuclear state. The model Hamiltonian for this system (Fig. A.1a) is,

$$H = (\Delta + \gamma_e B_0)\hat{\mathcal{S}}_z + \gamma_C B_0 \hat{I}_z^{n1} + A\hat{\mathcal{S}}_z \hat{I}_z^{n1} \tag{A.1}$$

where $\Delta = 2\pi \times 2.87$ GHz is the zero field splitting, A is the hyperfine interaction, and γ_e and γ_C are the electronic and nuclear spin gyromagnetic ratios. $\hat{\mathcal{S}}_z = \frac{1}{2}\hat{\mathbf{1}} + \hat{S}_z$ is a pseudo-spin one-half operator for the electronic spin subspace, $\hat{\mathbf{1}}$ is the identity matrix, and $\hat{I}_z^{n1}$ and $\hat{S}_z$ are the spin 1/2 angular momentum operators. Coherent oscillations between the $|0\rangle_e$ and $|1\rangle_e$ states, conditioned on a single proximal nuclear spin ($\mathbf{n}_1$) in $|\downarrow\rangle_{n_1}$ (or $|\uparrow\rangle_{n_1}$), are selectively driven by the microwave field MW1 (or MW2). To control nuclear spin $\mathbf{n}_1$ a resonantly tuned RF field to address the levels $|1\rangle_e |\downarrow\rangle_{n_1}$ and $|1\rangle_e |\uparrow\rangle_{n_1}$, which are energetically separated due to the hyperfine interaction (Fig. A.1a), is used. Following the initialization of spin **e**, spin $\mathbf{n}_1$ is polarized by applying MW1 and RF π pulses, which transfers the polarization from spin **e** to spin $\mathbf{n}_1$. Rabi oscillations of spin $\mathbf{n}_1$ are demonstrated (Fig. A.1e) by preparing spin **e** in the $|1\rangle_e$ state irrespective of the state of spin $\mathbf{n}_1$ (using MW1 and MW2 π-pulses) and increasing the RF pulse length. This data indicates that we can achieve spin $\mathbf{n}_1$ preparation (polarization) and readout with combined fidelity $F \equiv \langle\downarrow|\rho'|\downarrow\rangle \geq 75\%$, where ρ' is the reduced density operator for spin $\mathbf{n}_1$.

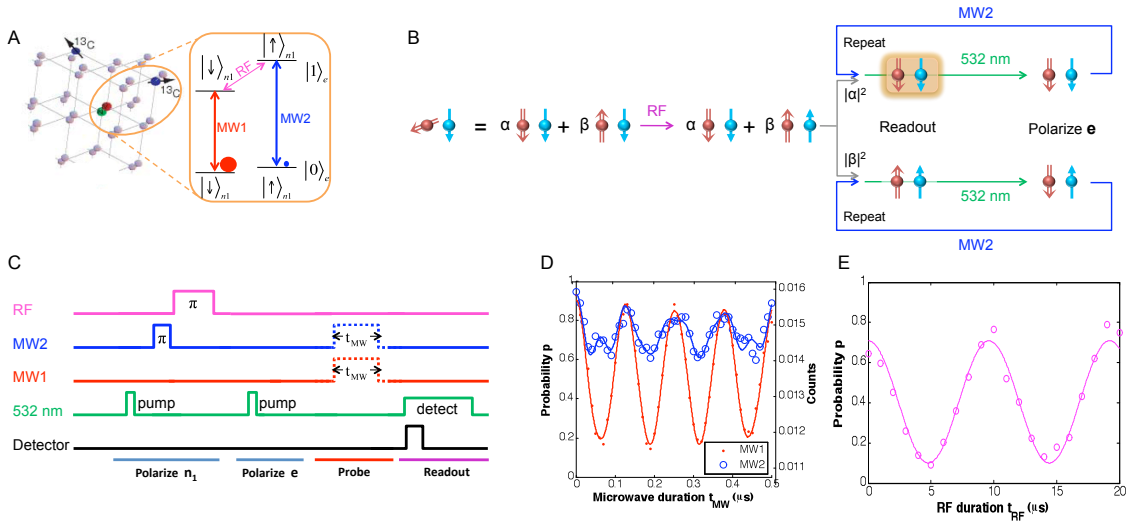

Figure A.1: | **Repetitive readout of an electronic spin.** (**A**) Illustration of the NV center and its proximal ^{13}C nuclear spins. Inset: Energy levels of the coupled spin system formed by the NV electronic spin (**e**) and the first proximal ^{13}C nuclear spin (**n**$_1$). With a static magnetic field applied along the NV axis, spin **n**$_1$ keeps the same quantization axis when spin **e** is $|0\rangle_e$ or $|1\rangle_e$. When spin **n**$_1$ is $|\downarrow\rangle_{n_1}$ (or $|\uparrow\rangle_{n_1}$), the microwave field MW1 (or MW2) resonantly drives spin **e** between $|0\rangle_e$ and $|1\rangle_e$, which can implement the C$_{n_1}$NOT$_e$ gate. When spin **e** is $|1\rangle_e$, the radio-frequency RF field resonantly drives spin **n**$_1$ between $|\downarrow\rangle_{n_1}$ and $|\uparrow\rangle_{n_1}$, which can implement the C$_e$NOT$_{n_1}$ gate. (**B**) Illustration of repetitive readout. The red down (up) arrow represents the electronic spin state $|0\rangle_e$ ($|1\rangle_e$), and blue down (up) arrowrepresents the nuclear spin state $|\downarrow\rangle_{n_1}$ ($|\uparrow\rangle_{n_1}$). (**C**) Experimental pulse sequences that polarize spin **n**$_1$ to $|\downarrow\rangle_{n_1}$ and spin **e** to $|0\rangle_e$, followed by various probe operations, before fluorescence readout of spin **e**. (**D**) Measured electronic spin Rabi oscillations driven by MW1 and MW2 fields, for polarized spin **n**$_1$. The small wiggles for MW2 are due to off-resonant driving of the majority population in the $|\downarrow\rangle_{n_1}$ state. The data is in agreement for finite detunings and microwave power (solid curves). The right vertical axis shows the average counts for a single readout. The left vertical axis shows the probability in the $|0\rangle_e$ state, obtained from the average counts. (**E**) Measured nuclear spin Rabi oscillation driven by the RF field.

A.3 Repetitive Readout with one nuclear spin

We now turn to the demonstration of the repetitive readout technique. As illustrated in Fig. A.1d, the direct readout of electronic spin is imperfect. We define n^0 and n^1 as the total number of photons detected for the $|0\rangle_e$ and $|1\rangle_e$ states, respectively, during a single measurement interval. The signal is defined as the difference in average counts between the two spin states: $A_0 = n^0 - n^1 \approx 0.005$ (Fig. A.1d). Experimentally, photon shot-noise dominates the fluctuations in the counts. Because of this shot noise and the low average count ($n^0 \approx 0.016$), we need to average over $N \sim 10^5$ experimental runs to obtain the data in Fig. A.1d.

To improve the signal, we use two spins: **e** and $\mathbf{n}_1$. Both spins are first polarized to the initial state $|0\rangle_e |\downarrow\rangle_{n_1}$. Next, we perform a unitary operation $U(t)$, which prepares the superposition state $|\Psi_1\rangle = (\alpha |0\rangle_e + \beta |1\rangle_e) |\downarrow\rangle_{n_1}$ that we would like to measure. Instead of immediately reading out the electronic spin, we use a controlled-not gate ($\mathrm{C}_e\mathrm{NOT}_{n_1}$, achieved by an RF π pulse) to correlate spin **e** with spin $\mathbf{n}_1$(Fig. A.2a). We then optically readout/pump spin **e**, leaving the spin system in the post-readout state: $\rho_{\text{post}} = |0\rangle \langle 0|_e \otimes \left(|\alpha|^2 |\downarrow\rangle \langle\downarrow| + |\beta|^2 |\uparrow\rangle \langle\uparrow|\right)_{n_1}$. The state of spin $\mathbf{n}_1$ via the electronic spin **e** by performing a controlled-not operation ($\mathrm{C}_{n_1}\mathrm{NOT}_e$, achieved by an MW1 or MW2 π pulse) is then readout. This completes a one-step readout of spin $\mathbf{n}_1$, which can be repeated.

As a direct illustration of the enhanced readout technique, Fig. A.2c shows the accumulated signal for Rabi oscillations of the electronic spin obtained by adding M subsequent repetitive readouts for each experimental run. This procedure results in a ten-fold enhancement of spin signal amplitude.

In order to further quantify the performance of this technique, the noise added with

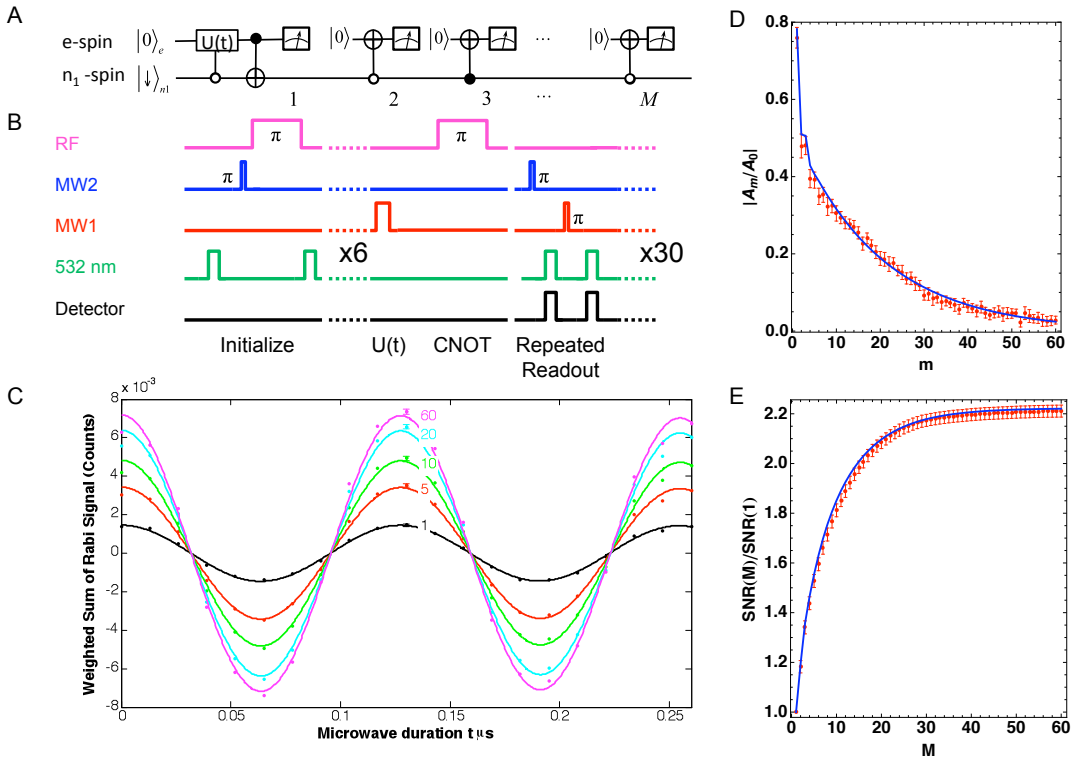

Figure A.2: | **Realization of repetitive readout.** (**A**) Quantum circuit for M-step repetitive readout scheme assisted by spin $\mathbf{n}_1$. (**B**) Operations and pulse sequences for $M = 60$. The initial state $|0\rangle_e |\downarrow\rangle_{n_1}$ is prepared with six-step pumping of spins **e** and $\mathbf{n}_1$. The MW1 pulse of duration t induces the Rabi rotation $U(t)$ of spin **e**, whose parity information is imprinted to spin $\mathbf{n}_1$ with an RF π pulse (i.e., the $\mathrm{C}_e\mathrm{NOT}_{n_1}$ gate). After fluorescence readout of spin **e**, $(M-1)$-repetitive readouts of spin $\mathbf{n}_1$ are performed by MW1 or MW2 π pulses (i.e., $\mathrm{C}_{n_1}\mathrm{NOT}_e$ gates) followed by fluorescence readout. Note the m=1 readout is not preceded by a MW1 pulse. (**C**) Cumulative signal obtained from repetitive readout measurements, summed from $m = 1$ to M, for $M = 1, 5, 10, 20, 60$ repetitions. Constant background counts are subtracted. (**D**) Amplitudes $|A_m|$ for Rabi oscillation measurements obtained from the m-th readout normalized to the signal amplitude without repetitive readout (A_0). (**E**) Improvement in SNR using the repetitive readout scheme. Blue curves in (D) and (E) are simulations with imperfection parameters estimated from independent experiments.

each additional repetitive readout must be considered. The repetitive readout spin signal is defined as a weighted sum of difference counts A_m associated with mth readout: $S_w(M) = \sum_{m=1}^{M} w_m A_m$. The average values of A_m are determined experimentally by measuring the difference in average counts associated with Rabi oscillations for each m-th repeated readout. The w_m allow us to weight the contribution of each repetitive readout to the overall signal. The noise corresponding to the repetitive readout signal is $\Delta S_w(M) = \sqrt{\sum_{m=1}^{M} w_m^2 \sigma_m^2}$. Here σ_m is the uncertainty of the measurement of A_m. Experimentally, this uncertainty is found to be independent of m.

The signal-to-noise figure of merit is defined as $SNR(M) = S_w(M)/\Delta S_w(M)$. The w_m weights are chosen by noting that the larger values of A_m allow us to extract more information given the fixed uncertainty of each measurement, and we should emphasize these readouts more. The optimal choice of weights corresponds to $w_m = |A_m|/\sigma_m^2$ and the optimized SNR is given by:

$$\text{SNR}_{opt}(M) = \sqrt{\sum_{m=1}^{M} \left| \frac{A_m}{\sigma_m} \right|^2} \tag{A.2}$$

In the ideal QND case, each repetitive readout would yield the same $|A_m|$ and the SNR would scale with $\sqrt{M}$. For our experiment, the SNR saturates (Fig. A.2e) due to the decay of the normalized amplitudes (Fig. A.3d). Nevertheless, the experimental data shown in Fig. A.2e indicate the enhancement of SNR by more than 220%.

In assessing this result, it is noted that various imperfections can affect the repetitive readout, which leads to the imperfect first readout $|A_1| / |A_0| < 1$, the sharp decrease in $|A_2|$, and the subsequent exponential reduction $|A_m| = |A_2|\eta^{(m-2)}$ with $\eta \approx 0.95$. These behaviors can be attributed to three major imperfections: errors from microwave pulses (about 7% error probability for each π pulse); imperfect optical pumping of the

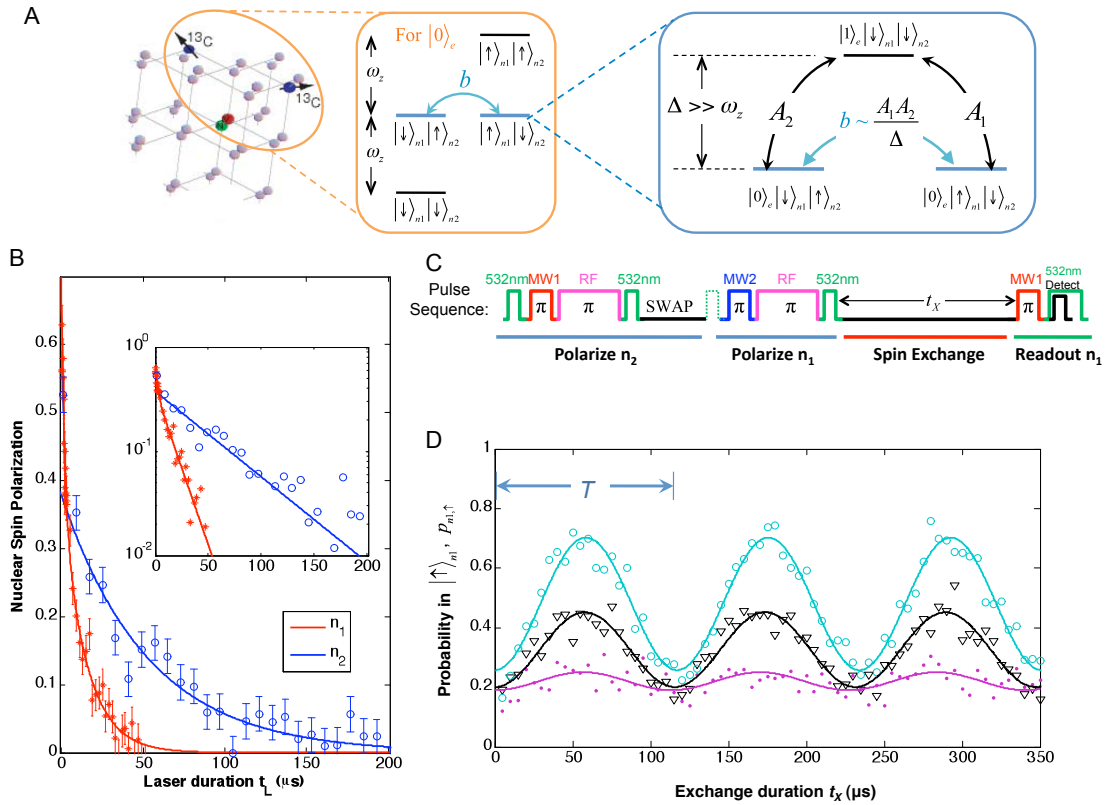

Figure A.3: | **Coherence and control of two nuclear spins.** (**A**) The coupled spin system formed by the NV electronic spin (**e**) and two proximal ^{13}C nuclear spins ($\mathbf{n}_1$ and $\mathbf{n}_2$). Middle inset: Energy levels for spins $\mathbf{n}_1$ and $\mathbf{n}_2$ when spin **e** is in the $|0\rangle_e$ state. Right inset: Schematic of flip-flop between spins $\mathbf{n}_1$ and $\mathbf{n}_2$, which is electron-mediated by the second-order hopping via $|1\rangle_e\,|\downarrow\rangle_{n_1}\,|\downarrow\rangle_{n_2}$. (**B**) Measured depolarization of spins $\mathbf{n}_1$ and $\mathbf{n}_2$ under optical illumination. For the duration of optical illumination t_L longer than 1 μs, the polarizations for spins $\mathbf{n}_1$ and $\mathbf{n}_2$ decay exponentially with characteristic times $\tau_{n_1} = 13\,(1)$ μs and $\tau_{n_2} = 53\,(5)$ μs, respectively. For t_L less than 1 μs, the decay is slightly faster, which is likely associated with dynamics of the spin-fluctuator model that describe optically induced depolarization of single nuclei [67]. These decay times are much longer than the optical readout/pump time of the electronic spin (about 350 ns). Inset: Log-linear plot. (**C**) Operations and pulse sequence to probe dynamics between spins $\mathbf{n}_1$ and $\mathbf{n}_2$. (**D**) Measured spin flip-flop dynamics between spins $\mathbf{n}_1$ and $\mathbf{n}_2$. For three different preparations of the initial state ($|\downarrow\rangle_{n_1}\,|\uparrow\rangle_{n_2}$ (cyan), $|\downarrow\rangle_{n_1}$ and n_2 in thermal state (black), and $|\downarrow\rangle_{n_1}\,|\downarrow\rangle_{n_2}$ (purple)), the observed population, $p_{n_1,\uparrow}(t)$, oscillates with the same period $T = 117\,(1)$ μs. These observations verify the theoretical prediction, with flip-flop coupling strength $b = 4.27\,(3)$ kHz.

electronic spin after each readout; and most substantially, the depolarization of the nuclear spin memory under optical illumination

A.4 Imperfections and optically induced depolarization

To quantify the latter process, we study the decay times for ^{13}C nuclear spins in the presence of optical illumination. For an illumination time t_L longer than 1 μs, the nuclear spin polarization decays exponentially, with a characteristic time $\tau_{n_1} = 13\,(1)$ μs (Fig. A.3b). Since τ_{n_1} is much longer than the time for optical readout and optical spin polarization of the NV electronic spin (350 ns), repetitive readout of **e** is possible. (In the absence of optical illumination, the ^{13}C nuclear spin decay times are $\gg 1$ ms [141, 63].) Despite the relatively long τ_{n_1}, after many cycles the nuclear spin depolarizes. This degrades the repetitive optical readout for larger m, yielding the overall exponential decay in the amplitude $|A_m|$ with increasing m.

A.5 Repetitive readout with two nuclear spins

As an indication of how this limit can be circumvented, the use of two ancillary nuclear spins is considered. The state of spin **e** may be correlated with a more distant spin $\mathbf{n}_2$, in addition to proximal spin $\mathbf{n}_1$. As the decay time of spin $\mathbf{n}_2$ is longer than that of spin $\mathbf{n}_1$ due to a weaker interaction with spin **e**, the information stored in spin $\mathbf{n}_2$ persists after spin $\mathbf{n}_1$ has been depolarized under optical illumination. This remaining $\mathbf{n}_2$ polarization can then be transferred to spin $\mathbf{n}_1$ and repetitively readout again.

Control of two nuclear spins is achieved by using the strongly coupled nuclear spin $\mathbf{n}_1$

as a probe for the second nearby ^{13}C nuclear spin $\mathbf{n}_2$, which cannot be directly observed via the NV center. By placing the NV electronic spin in $|0\rangle_e$ state, the hyperfine coupling is removed. This enables proximal ^{13}C nuclear spins with similar Zeeman energy to flip-flop and exchange spin population. Fig. A.3d shows that the nuclear population, $p_{n_1,\uparrow}(\tau)$, oscillates between $p_{n_1,\uparrow}(0) \approx 0.2$ and $p_{n_1,\uparrow}(T/2) \approx 0.5$ with a period of $T = 117\,(1)$ μs (Figs. 3a & 3c). The relatively high contrast of these oscillations suggests an interaction with a second nuclear spin ($\mathbf{n}_2$), as the two nuclei "flip-flop" between the states $|\uparrow\rangle_{n_1}|\downarrow\rangle_{n_2}$ and $|\downarrow\rangle_{n_1}|\uparrow\rangle_{n_2}$. Such excitation exchange requires a similar Zeeman splitting for the two spins, indicating that the second nucleus is also a ^{13}C. We note that the nuclear spin-spin interaction strength determined by our measurements, $b = \pi/T = 4.27\,(3)$ kHz, is several times that of a bare dipolar coupling (2 kHz for two ^{13}C nuclei separated by the nearest neighbor distance, $1.54\,\mathring{A}$) signifying that their interaction is mediated by the NV electronic spin (see inset of Fig. A.3a), which is described by the interaction hamiltonian $H_{int} = b(I_{1+}I_{2-} + I_{1-}I_{2+})$. This interaction can be used to effectively control the state of the second nucleus and of the entire three-spin system. Specifically, a half period of nuclear spin oscillation, $T/2$, constitutes a SWAP operation between the two nuclear spins. This operation can be used, e.g., to polarize the second nuclear spin (Figs. 3c, 3d). In addition, by modifying the initial state of spin $\mathbf{n}_1$, we can prepare the initial state of the two nuclei in any of the four possible configurations: $\{\uparrow\uparrow, \uparrow\downarrow, \downarrow\uparrow, \downarrow\downarrow\}$. Further control is provided by putting the electronic spin into the $|1\rangle_e$ state, in which case the flip-flop dynamics between spins $\mathbf{n}_1$ and $\mathbf{n}_2$ disappears. This is because spins $\mathbf{n}_1$ and $\mathbf{n}_2$ typically have very distinct hyperfine splittings that introduce a large energy difference ($\Delta E \gg b$) between $|\uparrow\rangle_{n_1}|\downarrow\rangle_{n_2}$ and $|\downarrow\rangle_{n_1}|\uparrow\rangle_{n_2}$ and quench the interaction. Therefore, we can implement a controlled-

SWAP operation between spins $\mathbf{n}_1$ and $\mathbf{n}_2$, enabling full control over spin $\mathbf{n}_2$.

A.6 Limitations

We further observe that spin $\mathbf{n}_2$ has decay time $\tau_{n_2} = 53\,(1)\ \mu$s (Fig. A.3b inset) under optical illumination. Compared with spin $\mathbf{n}_1$, spin $\mathbf{n}_2$ is less perturbed by the optical transitions between different electronic states, as it has a weaker hyperfine coupling to the electron [67].

To demonstrate concatenated readout experimentally, both nuclear spins are initialized in the state $|\downarrow\rangle_{n_1}|\downarrow\rangle_{n_2}$ and a single NV electronic spin that we would like to detect is prepared in a superposition state $(\alpha\,|0\rangle + \beta\,|1\rangle)_e$. First, the operation (C$_e$NOT$_{n_1}$-SWAP-C$_e$NOT$_{n_1}$) is used to prepare the GHZ-type state $|\Psi\rangle = \alpha\,|0\rangle_e\,|\downarrow\rangle_{n_1}\,|\downarrow\rangle_{n_2} + \beta\,|1\rangle_e\,|\uparrow\rangle_{n_1}\,|\uparrow\rangle_{n_2}$. Next, we optically readout/pump spin **e**, leaving the system in state $\rho'_{\text{post}} = |\alpha|^2\,|0\downarrow\downarrow\rangle\langle 0\downarrow\downarrow| + |\beta|^2\,|0\uparrow\uparrow\rangle\langle 0\uparrow\uparrow|$. $M-1$ repetitive readouts of spin $\mathbf{n}_1$ are then performed, in the manner described above, until spin $\mathbf{n}_1$ is depolarized. At this point, spin $\mathbf{n}_2$ is still directly correlated with the first measurement of the **e** spin. This information can be transferred to spin $\mathbf{n}_1$ by a nuclear SWAP gate. Thus, the parity information can be measured again by performing a second round of M-step repetitive readout. These operations are summarized in the quantum circuit (Fig. A.4a) and pulse sequences (Fig. A.4b).

Experimentally, the "revival" in the signal amplitude $|A_m|$ after the SWAP is demonstrated (Fig. A.4c), which leads to an associated jump in the SNR curve (Fig. A.4d) for $M' = 61$. This shows that the second nuclear spin can be used to further enhance the readout efficiency. While ideally the repetitive readout scheme assisted by two nuclear spins should improve the absolute SNR more than a single nuclear spin, in the present experi-

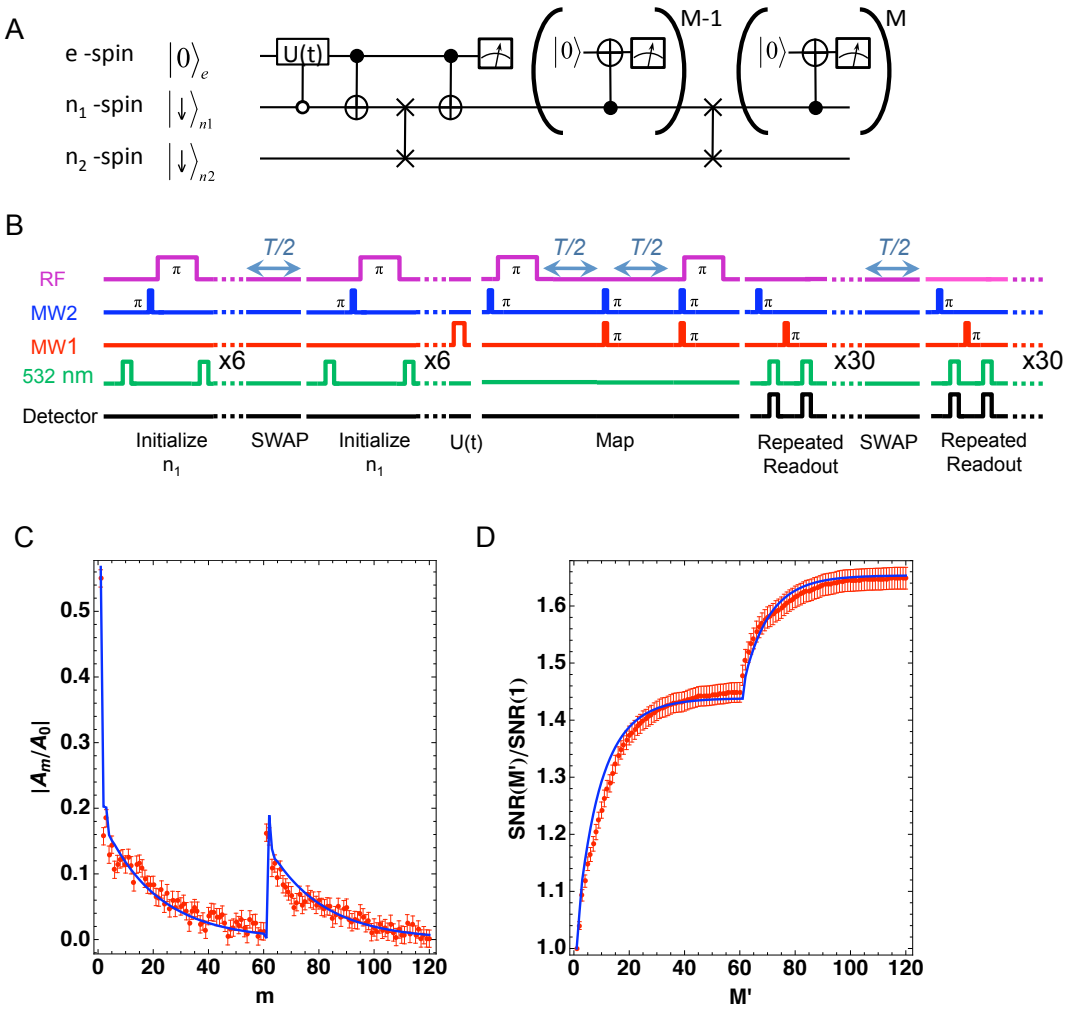

Figure A.4: | **Demonstration of two-level concatenated readout procedure.** (**A**) Quantum circuit for concatenated M-step repetitive readout scheme assisted by both spins $\mathbf{n}_1$ and $\mathbf{n}_2$. (**B**) Operations and pulse sequences for $M = 60$. Ideally, the GHZ-like state $\alpha\,|0\rangle_e\,|\downarrow\rangle_{n_1}\,|\downarrow\rangle_{n_2} + \beta\,|1\rangle_e\,|\uparrow\rangle_{n_1}\,|\uparrow\rangle_{n_2}$ with the parity information of spin **e** imprinted on both spins $\mathbf{n}_1$ and $\mathbf{n}_2$ is created before the first readout. After the first round of M-step repetitive readout, spin $\mathbf{n}_1$ is depolarized, but spin $\mathbf{n}_2$ maintains its polarization. The spin state of spin $\mathbf{n}_2$ is swapped to spin $\mathbf{n}_1$, which is then detected during the second round of M-step repetitive readouts. (**C**) Normalized amplitude $|A_m|\,/\,|A_0|$ obtained from the m-th readout. The blue curves in (C) and (D) are simulations with imperfection parameters estimated from independent experiments.

mental realization this is not yet so, as more errors are accumulated for the two nuclear spin scheme due to initialization and pulse imperfections. These errors reduce the optical signal amplitudes for the readout assisted by two nuclear spins, compromising the overall SNR improvement. Nevertheless, the experiments clearly demonstrate that it is in principle possible to further boost the relative SNR using additional nuclear spins.

A.7 Conclusion

While we have demonstrated an enhancement for coherent Rabi oscillations, any set of pulses acting on the electronic spin (e.g., a spin echo sequence) can be implemented. This should have immediate applications to NV-based nano-magnetometry [100, 101]. As the duration of the entire repetitive readout sequence ($\sim 150\mu s$ in Fig. A.2b) is shorter than the typical echo duration in pure diamond, SNR improvements directly translate into enhanced sensitivity and increased speed of nanoscale diamond magnetometer [52]. This may have important applications in probing time-varying processes in biophysical systems. The repetitive readout can also be used to achieve single-shot readout of NV centers. At room temperature, with optimized collection efficiency, an improvement in spin signal on the order of a few hundred is needed to achieved single-shot readout. Potentially this improvement can be obtained by using nuclei more robust to optical depolarization, such as the nitrogen nuclear spin of the NV center in isotopically pure ^{12}C diamond [72] and by using advanced control techniques [149, 150] to suppress the imperfections from microwave pulses. Furthermore, resonant optical excitations ($\lambda \approx 637$ nm) can be used for NV centers at cryogenic temperatures. Here the resolved spin structure of optical excited-states [126, 145, 151] can be exploited to readout the electronic spin much more efficiently with

reduced perturbation to the nuclear spin [67]. Under these conditions, a ten-fold spin signal improvement may be sufficient to enable single-shot readout of the NV electronic spin. In turn, this can be employed to perform robust, adaptive QND measurements of nuclear spin qubits which will be of direct use for distributed quantum networks [146, 63]. Our experiments demonstrate that manipulation of several nuclear spin ancillae surrounding a central electronic spin can be used to implement useful quantum algorithms in solid-state systems.

Appendix B

Scalable Architecture for a Room Temperature Solid-State Quantum Information Processor

B.1 Introduction

The realization of a scalable quantum information processor has emerged over the past decade as one of the central challenges at the interface of fundamental science and engineering. Here, we propose and analyze an architecture for a scalable, solid-state quantum information processor capable of operating at room temperature. Our approach is based upon recent experimental advances involving Nitrogen-Vacancy color centers in diamond. In particular, we demonstrate that the multiple challenges associated with operation at ambient temperature, individual addressing at the nanoscale, strong qubit coupling, robustness against disorder and low decoherence rates can be simultaneously achieved under realis-

tic, experimentally relevant conditions. The architecture uses a novel approach to quantum information transfer and includes a hierarchy of control at successive length scales. Moreover, it alleviates the stringent constraints currently limiting the realization of scalable quantum processors and will provide fundamental insights into the physics of non-equilibrium many-body quantum systems.

B.2 Motivation for NV based quantum information processor

The majority of realistic approaches to quantum information processing impose stringent requirements on the qubit environment, ranging from ultra-high vacuum to ultra-low temperature [152, 153, 154]. Such requirements, designed to isolate the qubit from external noise, often represent major experimental hurdles and may eventually limit the potential technological impact of a quantum information processor (QIP). For these reasons, developing a realistic framework for a feasible solid-state quantum processor capable of operating at room temperature is of both fundamental and practical importance. Nitrogen-Vacancy (NV) color centers in diamond stand out among other promising qubit implementations [27, 155, 156, 157] in that their electronic spins can be individually polarized, manipulated and optically detected under room-temperature conditions. Each NV center constitutes an individual two-qubit quantum register as it also contains a localized nuclear spin. The nuclear spin, which has an extremely long coherence time as seen in Chapter 2, can serve as a memory qubit, storing quantum information, while the electronic spin can be used to initialize, read out, and mediate coupling between nuclear spins of adjacent

registers. Magnetic dipole interactions allow for coherent coupling between NV centers spatially separated by tens of nanometers. While in principle, a perfect array of NV centers would enable scalable quantum information processing, in practice, the finite creation efficiency of such centers, along with the requirements for parallelism, necessitate the coupling of registers separated by significantly larger distances.

Recent advances involving the quantum manipulation of NV defects have allowed researchers to achieve sub-diffraction limited resolution, single-shot readout and dipole-coupling mediated entanglement between neighboring NV electronic spins [158, 81, 44, 72, 159, 160, 122, 66, 65, 47, 161]. Despite such substantial developments, it remains unclear whether these individual pieces, each of which invariably require a unique set of experimental conditions, can be seamlessly unified into a scalable room-temperature architecture [162]. Thus, the development of an architectural blueprint that combines the associated experimental facets while demonstrating that such a combination can enable high fidelity quantum operations is of crucial importance.

In what follows, we describe and analyze a feasible architecture for a room-temperature diamond-based QIP. Our approach makes use of an array of single NV centers, created through ion implantation and subsequent annealing [72, 163]. To overcome the challenge of coupling remote NV registers, we develop a novel method that enables coherent long-range interactions between NV centers, mediated by an optically un-addressable "dark" spin chain data bus (DSCB) [164]. For concreteness, within our architecture, we will consider the specific implementation of such a DSCB by utilizing implanted Nitrogen impurities (P1 centers) with spin 1/2, as shown in Fig. B.1a. [158, 165]. We analyze realistic imperfections and decoherence mechanisms, concluding that the implementation of this ar-

chitecture is feasible with current experimental technology. Moreover, we demonstrate the possibility of high fidelity remote coupling gates, whose error rates fall below the threshold for quantum error correction in a 2D surface code [166].

B.3 The NV Qubit Register

Single NV registers contain a spin triplet electronic ground state ($S = 1$) and can be optically pumped and initialized to the $|0\rangle_e$ spin state, which has no magnetic dipole coupling with other NV registers or impurities. After optical initialization, the electronic spin of each register remains in the $|0\rangle_e$ state, unless coherently transferred to the $|1\rangle_e$ state by a resonant microwave (MW) pulse, as depicted in Fig. B.1a [44, 72, 159, 160]. The nuclear spin associated with Nitrogen atoms ($I = 1/2$ for ^{15}N) possesses an extremely long coherence time (^{13}C nuclear spins could also in principle be utilized) and will serve as the memory qubit in our system [63, 68]; manipulation of the nuclear spin is accomplished with RF pulses [150]. The Hamiltonian governing the electronic and nuclear spins of the NV register is

$$H_{e,n} = \Delta_0 S_z^2 + \mu_e B S_z + \mu_n B I_z + A S_z I_z, \tag{B.1}$$

with zero-field splitting $\Delta_0 = 2.87$GHz, electronic spin gyromagnetic ratio $\mu_e = -2.8$ MHz/Gauss, nuclear spin gyromagnetic ratio $\mu_n = -0.43$ kHz/Gauss, and hyperfine coupling $A = 3.0$ MHz [44]. The application of a magnetic field along the NV-axis ($\hat{z}$) ensures full addressability of the two-qubit system, resulting in the energy levels shown in Fig. B.1a. A universal set of two-qubit quantum operations can easily be achieved with only MW and RF controls, as shown in Fig. B.1b [150].

Furthermore, it is possible to selectively readout the state of the NV register; for ex-

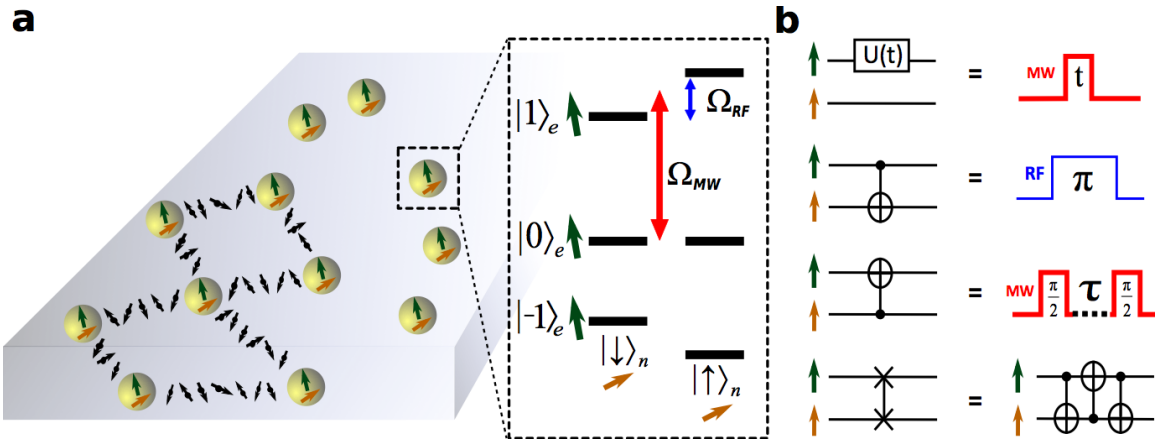

Figure B.1: | **Schematic representation of individual NV registers within bulk diamond** (**a**) Each NV register contains a memory nuclear spin $I = 1/2$ (yellow) and an electronic spin $S = 1$ (green). Dark spins (black) represent an optically un-addressable spin chain which coherently couples spatially separated NV registers. The NV level structure (in a high B field) is shown. The electronic spin is coherently manipulated by a resonant microwave (Ω_{MW}); the nuclear spin is manipulated through an RF pulse (Ω_{RF}). (**b**) A universal set of two-qubit gates can easily be achieved with only MW and RF controls [150]. Electronic spin manipulation can be accomplished with a MW field, where t represents the duration of the MW pulse. A $\mathrm{C}_e\mathrm{NOT}_n$ gate between electronic and nuclear spin can be achieved by exploiting the hyperfine coupling. In a similarly fashion, a $\mathrm{C}_n\mathrm{NOT}_e$ gate can be accomplished. Finally, combining the $\mathrm{C}_e\mathrm{NOT}_n$ and $\mathrm{C}_n\mathrm{NOT}_e$ gates allows for the execution of a SWAP gate.

ample, to readout the nuclear qubit of a register, we apply a $C_n NOT_e$ gate to couple the electronic and nuclear spins, thereby allowing for readout of the electronic spin based on fluorescence detection. Our approach to scalability will ultimately involve a hierarchical design principle which ensures a spatial separation between NV registers of order the optical wavelength; while this will, in principle, enable individualized readout, additional use of a red Laguerre-Gaussian (LG) beam can further enhance readout fidelities [122]. Indeed, the readout of individual registers may be complicated by the strong fluorescence background from neighboring NV centers. To suppress this background fluorescence, a red donut beam can be used, with its minimum located at the particular NV center being read out [122]. While the fluorescence signal from the NV register located at the minimum persists, the remaining illuminated registers will be dominated by the stimulated emission induced by the red donut beam. In addition to suppressing the background noise, the red donut beam can also suppress the nuclear decoherence of the remaining NV registers, by reducing the amount of time these registers spend in the excited electronic state [167, 105]

Moreover, this approach may be particularly applicable in the case where NV registers are separated by sub-optical-wavelength distances. After each round of fluorescence detection, the electronic spin is polarized to the $|0\rangle_e$ state, while the I_z component of the nuclear spin, a quantum non-demolition observable, remains unchanged [147]. Therefore, it is possible to repeat this readout procedure multiple times in order to improve the readout fidelity [66, 65]. A strong magnetic field $B_{z,0} \sim 1$ Tesla along the NV axis should be used to decouple the electronic and nuclear spins in order to achieve high fidelity single shot readout of NV registers [65]. In addition to sub-wavelength readout, optical donut beams also introduce the possibility of selectively manipulating individual NV registers with sub-

wavelength resolution. In this case, we envision the use of a green LG donut beam; while un-illuminated NV centers may respond to a resonant MW pulse, illuminated registers, as discussed in Chapter 4.7, undergo a strong optical cycling transition which suppresses their response to microwave pulses due to the quantum Zeno effect [168, 105].

B.4 Qubit control based on Laguerre-Gaussian beams

In the previous section, we mentioned two possible approaches to using Laguerre-Gaussian (LG) donut beams to further enhance our scalable architecture. First, we discussed the possibility of using a red LG donut to enhance the readout fidelity. Second, we discussed the possibility of using a green LG donut to enable subwavelength coherent control. Here, we provide a detailed discussion of the associated errors and error suppression in both cases.

A red LG beam, which is detuned from the optical transition will only induce stimulated decay of an NV center, but will never induce optical cycling. In this way, those illuminated NVs situated in the red LG circumference will be dominated by stimulated emission, leaving only the desired readout NV (in the donut center) to emit spontaneously for fluorescent detection. Moreover, such a red LG donut will also help suppress the undesired decoherence of neighboring NV registers. Indeed, it is favorable to induce the fast stimulated decay of such neighboring centers since this will suppress the NV-excited state lifetime, thereby limiting the effective dephasing of the nuclear spin memory. In particular, we can estimate the decoherence of the nuclear spin qubit of a neighboring register during optical readout. With a highly focused green Gaussian laser beam, the probability to excite a neighboring NV center can be very small. In particular, for a beam waist of 200nm, the

optical intensity at 500nm (e.g. the separation between plaquettes) is only 3×10^{-6} of the beam center. Thus, the error probability associated with an unintended excitation is roughly $p_1 \sim 3 \times 10^{-6}$ for each readout attempt. Next, the stimulated emission induced by the red LG beam can reduce the excited state lifetime from 10ns to $\tau' = 0.1$ns (or less). Assuming that the excited state has a large hyperfine coupling $A' = 40(2\pi)$MHz, yields an effective error probability, $p_2 = (A'\tau')^2 = 0.03$ for each unintended optical excitation. In combination, the overall error probability associated with each attempted readout is $p_1 p_2 \sim 10^{-7}$. Even after thousands of readout repetitions, the error probability of neighboring NVs can be controlled to below 0.1% and hence can be safely neglected in our discussion. Thus, our above error analysis demonstrates that the use of a red LG beam for stimulated emission can indeed provide a further enhancement in our readout fidelity.

Furthermore, the use of green Laguerre-Gaussian optical donut beams may enable the subwavelength selective manipulation of individual NV registers. Here, we consider the dominant imperfection in such subwavelength control: The residual optical excitation rate κ_0 for an unilluminated NV register in the dark donut center (due to imperfect destructive interference). We estimate that the error probability for the selected (e.g. resonant and unilluminated) NV register is: $p_{err,\text{selected}} \approx \frac{\kappa_0}{\Omega_i}$, which characterizes the undesired optical excitation probability during time $1/\Omega_i$. Such an error must be optimized in the context of off-resonant cross-talk; however, given good interference contrast $\kappa_0/\kappa = 10^{-6}$, $p_{err,\text{selected}}$ can easily be rendered sub-percent. The notion of subwavelength register control also naturally suggests the importance of microcoil engineering as a necessary ingredient for our architecture; indeed, there has been tremendous recent progress demonstrating the possible optimization of planar microcoil arrays [169].

B.5 Arbitrary Two-Qubit Gates within the NV Register

While the dark spin chain data bus enables long-range quantum logic between spatially separated NV electronic spins, universal two-qubit gates between the nuclear spin quantum memories require additional local logic between nuclear and electronic spins, as outlined in Fig. B.1b. Here, we specify in detail, the implementation of such local logic gates. A strong MW pulse (with $\Omega_{MW} \gg A$) can perform an arbitrary electronic spin rotation independent of the nuclear spin state. This can be mapped to a nuclear spin rotation by implementing a SWAP gate between the nuclear and electronic spins. Such a SWAP gate can be decomposed into three controlled-NOT gates: $\mathrm{C}_e\mathrm{NOT}_n$ $\mathrm{C}_n\mathrm{NOT}_e\mathrm{C}_e\mathrm{NOT}_n$. A $\mathrm{C}_e\mathrm{NOT}_n$ gate can be accomplished by utilizing an RF π-pulse (with $\Omega_{RF} \ll A$), which flips the nuclear spin conditioned on the electronic spin being in $|1\rangle_e$. Finally, a hyperfine-driven controlled-phase gate enables the remaining $\mathrm{C}_n\mathrm{NOT}_e$ gate (up to single Hadamards on the electronic spin). This demonstrates that a universal set of local two-qubit gates between NV electronic and nuclear spins can easily be achieved with only MW and RF controls [150]. Such arbitrary local logic is crucial to enable the preparation of nuclear spin quantum information and forms an important portion of DSCB mediated remote coupling (Fig. B.3c).

B.6 Approach to Scalable Architecture

One of the key requirements for fault-tolerant quantum computation is the ability to perform parallel gate operations. In our approach, this is achieved by considering a hierarchy of controllability. The lowest level of the hierarchy consists of an individual optically addressable plaquette with horizontal and vertical spatial dimensions $\sim 100 - 500$nm, con-

taining a single computational NV register, as shown in Fig. B.2a. The plaquette dimensions are chosen such that register control and readout can be achieved using conventional far-field or sub-wavelength optical techniques [44, 63, 122, 105, 170]. The second level, termed a super-plaquette ($\sim 10\mu$m $\times 10\mu$m), consists of a lattice of plaquettes whose computational registers are coupled through DSCBs. At the highest level of the hierarchy, we consider an array of super-plaquettes, where individual super-plaquettes are controlled by confined microwave fields [171]. In particular, micro-solenoids can confine fields to within super-plaquettes, allowing for parallel operations at the super-plaquette level. For example, as depicted in Fig. B.2 independent microwave pulses can allow for simultaneous operations on the electronic spins of all computational NV registers within all super-plaquettes. In order to control registers at the super-plaquette boundaries, we define a dual super-plaquette lattice (Fig. B.2a). Localized microwave fields within such a dual lattice can provide a smooth transition between the boundaries of neighboring super-plaquettes.

Taking advantage of the separation of length scales inherent to optical control and microwave confinement provides a mechanism to achieve parallelism; indeed, the hierarchical control of plaquettes, super-plaquettes, and super-plaquette arrays allows for simultaneous single- and two-qubit gate operations, which are fundamental to fault-tolerant computation. One of the key difference in the currently proposed architecture as compared to previous proposals [156] is that the design here does not rely on optically resolved transitions, which are only accessible at cryogenic temperatures.

The required 2D array of NV centers can be created via a two-step implantation process. We envision first implanting single nitrogen atoms along particular rows within each plaquette, as shown in Fig. B.2b.; subsequent annealing occurs until the creation of an NV

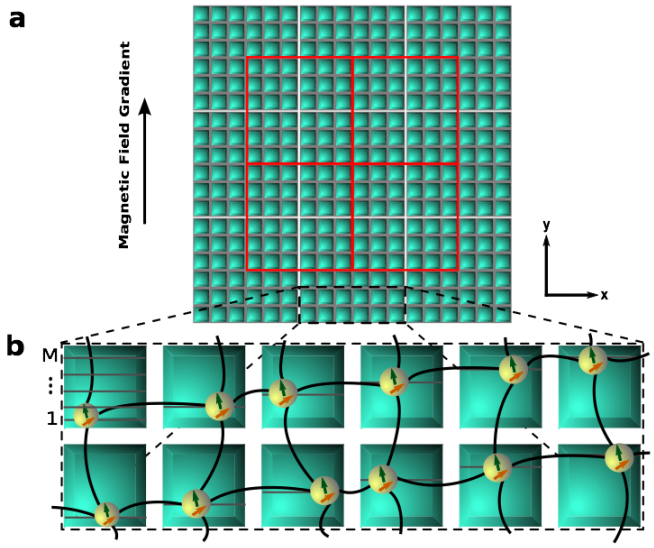

Figure B.2: | **Architecture for a room-temperature solid-state quantum computer** (**a**) A two-dimensional hierarchical lattice allowing for fully parallel operations. Individual plaquettes are outlined in grey with each containing a single computational NV register. Super-plaquettes are outlined in white; each super-plaquette is separately manipulated by micro-solenoid confined microwave fields. A dual super-plaquette lattice outlined in red ensures information transfer across super-plaquette boundaries. (**b**) NV registers, consisting of an electronic (green) and nuclear (yellow) spin are depicted within a staggered up-sloping array which is row-repetitive. Since each NV register occupies a unique row within the super-plaquette, the magnetic field gradient in the $\hat{y}$ direction allows for individual spectroscopic addressing of single registers. Coherent coupling of spatially separated NV registers in adjacent plaquettes is mediated by a dark spin chain data bus (curved line).

center, after which a second nitrogen implantation step generates the spin chain data bus. The selective manipulation of individual registers within our 2D array is enabled by the application of a spatially dependent external magnetic field $B_z(y) = (\alpha y + B_{z,0})\hat{z}$; this 1D magnetic field gradient is sufficiently strong ($\alpha \sim 10^5$T/m) to allow for spectroscopic microwave addressing of individual NV registers, each of which occupies a unique row in the super-plaquette, as shown in Fig. B.2b [171, 172, 173].

B.7 Dark Spin Chain Data Bus

To coherently couple two spatially separated NV centers, we consider two distinct approaches. First, we consider an approach, which is appropriate for spin-state transfer along the direction of the magnetic field gradient, in which individual addressing of spins is possible. This allows for an adiabatic sequential SWAP between neighboring qubits and, consequently, between the ends of the chain. Alternatively, in the situation where individual addressing of spins is not possible (i.e. direction transverse to the field gradient), we show that global control pulses achieve effective Hamiltonian evolution, which enables quantum state transfer through the spin chain. In both cases, we show that perfect state transfer and remote coupling gates are possible even when the intermediate spin chain is completely unpolarized (infinite spin temperature).

We begin by analyzing the adiabatic sequential SWAP in a spin-$1/2$ chain. This approach is suitable to couple registers in plaquettes that are vertically adjacent, relying upon the individual addressability of qubits and utilizing the magnetic dipole coupling between spin-chain elements. As shown in [82], under the secular approximation, the magnetic

dipole coupling between a pair of neighboring spins can be reduced to Ising form

$$H_{int} = 4\kappa S_z^1 S_z^2 + \sum_{i=1,2} (\omega_0 + \delta_i) S_z^i, \tag{B.2}$$

where κ is the relevant component of the dipole tensor, ω_0 captures the electronic Zeeman energy, and δ_i characterizes both the hyperfine term (nuclear spin dependent) and the magnetic field gradient. From the Ising Hamiltonian, an XX interaction between qubits can be distilled by driving with $H_{drive} = \sum_{i=1,2} 2\Omega_i S_x^i \cos[(\omega_0 + \delta_i)t]$, leading to (under the rotating wave approximation, in the rotating frame, and in a rotated basis with $(x, y, z) \to (z, -y, x)$)

$$H_{int} = \kappa(S_1^+ S_2^- + S_1^- S_2^+) + \Omega_1 S_z^1 + \Omega_2 S_z^2. \tag{B.3}$$

The spin-flip process in H_{int} is highly suppressed in the limit of $|\Omega_1 - \Omega_2| \gg \kappa$, while the same process is dominant in the case of $|\Omega_1 - \Omega_2| \ll \kappa$. Hence, by slowly ramping the Rabi frequencies Ω_1 and Ω_2 through one another, adiabatic SWAP of the quantum states of the two impurities can be achieved through rapid adiabatic passage, as shown in Fig. B.3a. Generalizing to arbitrary length spin chains yields $H_{int} = \sum_i \kappa(S_i^+ S_{i+1}^- + S_i^- S_{i+1}^+) + \sum_i \Omega_i S_z^i$, whereby the sequential adiabatic SWAP of quantum states along the spin chain can be achieved by successively tuning individual Rabi frequencies across one another. During the adiabatic SWAP of a single pair of spins, higher order interactions, such as those resulting from next-to-nearest neighbors, will be suppressed due to the differences in Rabi frequencies. By including the magnetic dipole coupling between the electronic spin of the NV register and the spin chain quantum channel, we arrive at an effective mixed spin chain with the DSCB connecting the two electronic spins of the vertically separated NV registers.

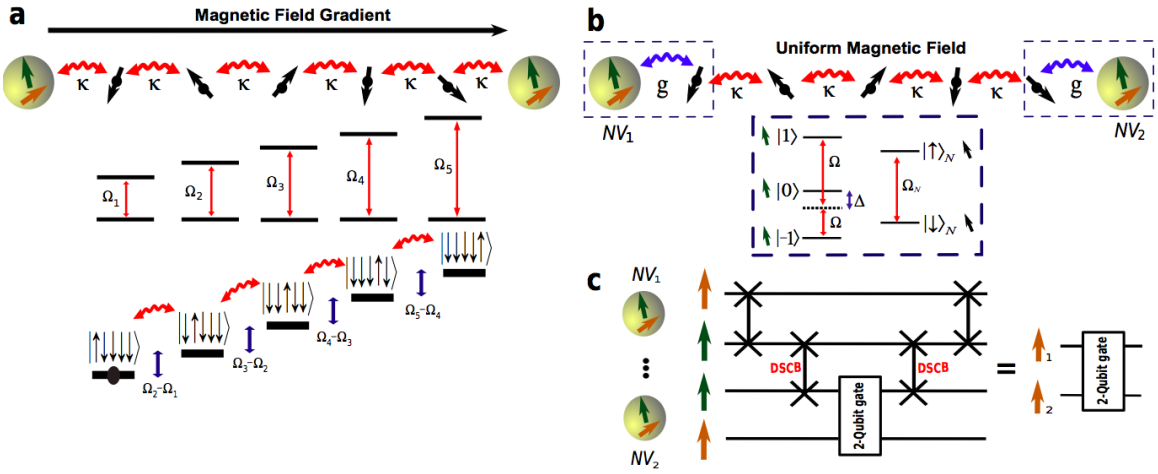

Figure B.3: | **Coherent coupling of NV registers via dark spin chain data bus (DSCB)** (**a**) Adiabatic sequential SWAP along the vertical direction. Adiabatic SWAP between two nearest neighbor spins is achieved by slowly ramping the Rabi frequencies Ω_i and Ω_j through one another. (**b**) Free fermion state transfer in the horizontal direction. The coupling strength between the end qubits and the spin chain is g, while the interchain coupling strength is κ. Schematic representation of the level structure of the NV electronic spin and a dark impurity spin is shown in the dashed box. The coupling g is controlled by driving the NV in two-photon resonance, with Rabi frequency Ω and detuning Δ. (**c**) Schematic circuit diagram outlining the protocol to couple two separated nuclear memory qubits.

Crucially, such an adiabatic sequential SWAP is robust against variations in the coupling strength κ, which can be induced by the imprecise implantation of impurities that form the spin-$1/2$ chain; in particular, even for the case of varying $\kappa_{i,i+1}$, perfect adiabatic SWAP occurs so long as the rate at which Ω_i and Ω_{i+1} are ramped through one another is sufficiently small. Within the proposed architecture, the impurities forming the horizontal spin chain will not induce operational errors during the vertical adiabatic sequential SWAP since the design principle allows for selective spin echoing (Fig. B.4).

Next, we consider a second method, termed free fermion state transfer (FFST) developed in [174], to coherently couple NV registers. In contrast to the adiabatic sequential SWAP, the method utilizes only global control over impurities and effective Hamiltonian evolution. The relaxation of the requirement of individual control over elements of the dark spin chain renders this second method applicable for coherent coupling between NV registers in horizontally adjacent plaquettes, transverse to the direction of the field gradient. In particular, the protocol achieves coherent coupling through an unpolarized, infinite temperature spin chain, employing purely Hamiltonian evolution under

$$\begin{aligned} H_{FFST} = g(S^+_{NV_1}S^-_1 + S^+_{NV_2}S^-_N + \text{ h.c.}) \\ + \sum_{i=1}^{N-1} \kappa(S^+_i S^-_{i+1} + S^-_i S^+_{i+1}) \end{aligned} \tag{B.4}$$

as shown in Fig. B.3b. This Hamiltonian, obtained in analogy to (eq. B.3), results in coherent interactions between NV centers, which is best understood via an analogy to eigenmode tunneling in a many-body system. Specifically, the spin chain described by H_{FFST} can be viewed as a system of non-interacting fermions. As described in [174], by tuning the NV centers into resonance with a single fermionic eigenmode, an effective three-state system can be realized. Mediated by this fermionic eigenmode, the electronic states of two remote

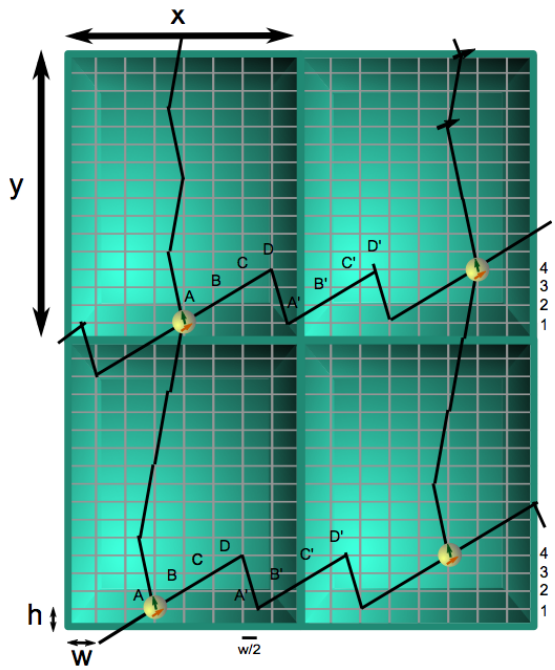

Figure B.4: | **Architectural Design** Plaquettes, outlined in green, are chosen with $y \approx 600$nm and $x \approx 550$nm; the individual plaquette-lattice spacing is chosen with $h \approx 5$nm and $w \approx 22$nm. The magnetic field is oriented along the NV axis which is normal to the depicted computational plane and the gradient is along the $\hat{y}$ direction. The distance between all nearest neighbor pairs in the horizontal direction is ≈ 22.5nm ($\sqrt{h^2 + w^2} = \sqrt{(4h)^2 + (w/2)^2}$) and the $\hat{x}$ spacing between spin D and spin A' is given by $w/2$. In the chosen plaquette-lattice neighboring plaquettes are coupled by ≈ 25 Nitrogen impurities (black spins) in the $\hat{x}$ direction and by ≈ 30 Nitrogen impurities in the $\hat{y}$ direction. The zig-zag pattern of impurity implantation in the $\hat{y}$ direction ($w/2$ horizontal distance) ensures that all spin chain links are of identical length, thereby allowing for parallel sequential SWAP operations along $\hat{y}$.

NV centers can be coherently swapped. Coupled with arbitrary two-qubit gates between the nuclear and electronic spin (Fig. B.1b), an electronic SWAP gate enables universal computation between spatially remote nuclear spin memories, as shown in Fig. B.3c. Crucially, such a SWAP gate is insensitive to the polarization of the intermediate dark spins and high-fidelity quantum state transfer can be achieved, provided that the fermionic mode is delocalized and that the coupling, g, of the NV qubit to the spin chain is controllable. By utilizing the three-level NV ground-state structure (Fig. B.3b), it is possible to fully control the NV-chain coupling. This tunability also ensures that FFST is fundamentally robust to experimentally relevant coupling-strength disorder, which could be induced by implantation imprecision. Indeed, by separately tuning the NV-chain coupling on either side of the DSCB, it is possible to compensate for both disorder-induced asymmetry in the fermionic eigenmode as well as altered statistics of the eigenenergies (Supplementary Methods of [82]) [174, 175, 176].

B.8 Controlling Qubit-Chain Coupling in the NV Architecture

To achieve an effective Hamiltonian of the form given by Eq. B.4, it is essential to control the coupling strength between the NV register and the neighboring impurity. Here, we utilize the three levels of the NV electronic spin [177] to effectively control g, as shown in Fig. B.3b, whereby the Hamiltonian (under microwave driving) can be written as

$$\begin{aligned} H = & -\Delta(|1\rangle\langle 1| + |-1\rangle\langle -1|) \\ & -\Omega(|0\rangle\langle 1| + |0\rangle\langle -1| + \text{h.c.}) - \Omega_N S_x^N + 4\kappa S_z^{NV} S_z^N, \end{aligned} \tag{B.5}$$

where Ω represents the Rabi frequency on the NV register, Δ represents the associated detuning, and Ω_N represents the Rabi frequency on the Nitrogen impurity. In this case, since the NV two-photon detuning is zero, it is convenient to define bright and dark states, $|B\rangle = \frac{|1\rangle+|-1\rangle}{\sqrt{2}}$ and $|D\rangle = \frac{|1\rangle-|-1\rangle}{\sqrt{2}}$; further, in the resulting two-level picture, the associated dressed states are $|+\rangle \approx |B\rangle + \frac{\sqrt{2}\Omega}{\Delta}|0\rangle$ and $|-\rangle \approx |0\rangle - \frac{\sqrt{2}\Omega}{\Delta}|B\rangle$, in the limit $\Omega \ll \Delta$. Hence, rewriting the Hamiltonian in this limit yields

$$\begin{aligned} H = & -\Delta|D\rangle\langle D| - (\Delta + \frac{2\Omega^2}{\Delta})|+\rangle\langle +| \\ & + \frac{2\Omega^2}{\Delta}|-\rangle\langle -| - \frac{1}{2}\Omega_N(|+\rangle_N\langle +| - |-\rangle_N\langle -|) \\ & + 2\kappa(|B\rangle\langle D| + |D\rangle\langle B|)(|+\rangle_N\langle -| + |-\rangle_N\langle +|), \end{aligned} \tag{B.6}$$

where $|\pm\rangle_N = \frac{|\uparrow\rangle_N \pm |\downarrow\rangle_N}{\sqrt{2}}$ correspond to the two S_x^N-eigenstates of the Nitrogen impurity. The coupling term can be further re-expressed as

$$\begin{aligned} & 2\kappa\left\{(|+\rangle\langle D| + |D\rangle\langle +|) - \frac{\sqrt{2}\Omega}{\Delta}(|-\rangle\langle D| + |D\rangle\langle -|)\right\} \\ & * (|+_N\rangle\langle -_N| + |-_N\rangle\langle +_N|). \end{aligned} \tag{B.7}$$

Thus, by working within the NV subspace $\{|D\rangle, |-\rangle\}$, it is possible to completely control the coupling between the NV register and Nitrogen impurity, $g \sim \kappa\frac{\Omega}{\Delta}$, by tuning the Rabi frequency and detuning. It is possible to work in the required two-state subspace by ensuring that $\kappa \ll \Delta$ and hence, that the $|+\rangle$ state remains unpopulated, with corresponding off-resonant error κ^2/Δ^2.

Furthermore, we evince a possible scheme to coherently map the quantum information that is stored in the nuclear memory into the desired electronic subspace. For example, consider mapping $|0\rangle \otimes (\alpha|\uparrow\rangle + \beta|\downarrow\rangle)$ to $(\alpha|-\rangle + \beta|D\rangle) \otimes |\uparrow\rangle$, where the first (tensor) factor corresponds to the electronic state and the second corresponds to the nuclear state

of a single NV. The proposed mapping can be achieved in a two-step process. First, by simultaneously performing a $\pi-$pulse on the transitions $|0\rangle \otimes |\downarrow\rangle \rightarrow |-1\rangle \otimes |\downarrow\rangle$ and $|0\rangle \otimes |\downarrow\rangle \rightarrow |1\rangle \otimes |\downarrow\rangle$ with oppositely signed Rabi frequencies, one can map $|0\rangle \otimes |\downarrow\rangle$ to $|D\rangle \otimes |\downarrow\rangle$. Next, one utilizes an RF pulse to flip the nuclear spin, which yields $|D\rangle \otimes |\downarrow\rangle \rightarrow |D\rangle \otimes |\uparrow\rangle$. Finally, turning Ω on in an adiabatic fashion ensures that the state preparation populates only $|D\rangle$ and $|-\rangle$, thereby mapping the quantum information into the desired electronic subspace.

B.9 Specific Implementation of Architecture

In this section, we offer a specific implementation of the architectural design principle and discuss the various ingredients required to achieve DSCB-mediated coherent coupling between spatially separated NV registers. In particular, we consider the refocusing of non-nearest neighbor interactions along the horizontal spin chain.

The effective Hamiltonian evinced in equation(eq. B.4) has nearest neighbor form; although next-nearest-neighbor interactions will represent a correction, we show that such interactions can be refocused within the current architectural design, and further, that in principle, interactions beyond next-nearest-neighbor can also be refocused. In particular, the horizontal spin chain (N total spins) is arranged in a staggered saw-tooth fashion, as shown in Fig. B.5. Within such an architecture, nearest neighbor coupling terms correspond to all pairs of adjacent spins, each separated by $\approx$ 20nm, with corresponding interaction Hamiltonian

$$H_N = \sum \kappa_N (S_A^+ S_B^- + S_B^+ S_C^- + S_C^+ S_D^- + S_D^+ S_{A'}^-) + \text{h.c.} \tag{B.8}$$

where the sum runs over all nearest neighbor pairs in a given dark spin chain. Thus, next-to-nearest neighbor terms for each spin correspond to the subsequent strongest interaction

$$H_{NN} = \sum \kappa_{NN}(S_A^+ S_C^- + S_B^+ S_D^-)$$
$$+\kappa_{NN'}(S_C^+ S_{A'}^- + S_D^+ S_{B'}^-) + \text{h.c.} \tag{B.9}$$

where the prime denotes the next link in the saw-tooth chain as shown in Fig. B.5. In addition to the impurity spins, FFST incorporates the electronic spin of the NV register into a mixed spin chain. It is important to note that the spin-flip Hamiltonians H_N and H_{NN} are derived from the secular approximated Ising coupling by the application of driving fields as per (eq. B.3). Since each row $(1, 2, 3, 4)$ is separately addressable by virtue of the magnetic field gradient (applying four frequencies per row to ensure that all Jahn-Teller and nuclear spin states are addressed), it is possible to apply a spin-echo procedure to refocus the next-nearest-neighbor terms. In particular, by flipping the spins in rows 1 and 2 (Fig. B.5) after time $T_d/2$ where T_d is a small fraction of the desired evolution duration, the next-nearest-neighbor interactions are refocused since each term contains spins from only row 1 or 2. However, half of the nearest neighbor interactions are also refocused, leaving effective evolution under the Hamiltonian $H_{eff1} = \sum \kappa_N(S_A^+ S_B^- + S_C^+ S_D^-) + \text{h.c.}$ Analogously, by flipping the spins in rows 2 and 3, effective evolution under the Hamiltonian $H_{eff2} = \sum \kappa_N(S_B^+ S_C^- + S_D^+ S_{A'}^-) + \text{h.c.}$ is achieved, again with H_{NN} refocused. Combining the evolution according to H_{eff1} and H_{eff2} yields the desired nearest-neighbor Hamiltonian with next-to-nearest neighbor interactions refocused. However, since H_{eff1} and H_{eff2} do not commute, it will be necessary to employ piecewise evolution according to the Trotter-Suzuki formalism [178]. Further refocusing of higher order non-nearest neighbor interactions can also be achieved by extending the number of rows corresponding to the

saw-tooth design; such an extension allows for the isolation of each specific pair of nearest neighbor interactions, thereby achieving the desired nearest-neighbor evolution through a Trotter sequence.

B.10 Implementation, Operational Errors and Gate Fidelities

The specific implementation of the DSCB can be achieved with implanted Nitrogen impurity ions. Dipole coupling between neighboring Nitrogen electronic spins forms the DSCB, while dipole coupling between the NV and Nitrogen electronic spins forms the qubit-DSCB interaction; non-secular terms of this magnetic dipole coupling are highly suppressed due to the spatially dependent external magnetic field $B_z(y)$, resulting in the effective interaction found in (eq. B.2). In addition, the Nitrogen impurities possess a strong hyperfine coupling, the principal axis of which can take on four possible orientations due to tetrahedral symmetry [179, 180, 181]. Dynamic Jahn-Teller (JT) reorientation of the Nitrogen impurity's hyperfine principal axis results in two particular considerations, namely, the addressing of additional JT frequencies yielding a denser super-plaquette frequency spectrum and the JT-governed spin-lattice relaxation (SLR) time T_1^N (Supplementary Methods of [82]). Since T_1^N is characterized by an Arrhenius rate equation [180] at ambient temperatures, a combination of a static electric field and slight cooling by ≈ 50K allows for a substantial extension of the relaxation time to ~ 1s; hence, in the following consideration of operational errors, we will assume that we are limited by T_1^{NV}, the spin-lattice relaxation time of the NV center.

We now consider various imperfections, which may introduce operational errors. In particular, we consider the errors associated with the sequential SWAP mediated coupling between vertically adjacent registers and the FFST between horizontally adjacent registers. We begin by discussing the analytic error estimate associated with each method, after which, we summarize the results of full numerical simulations (see also Supplementary Methods of [82]).

First, we consider the accumulated infidelity associated with the adiabatic sequential SWAP,

$$p_{err}^{SS} \approx N(p_{off}^{SS} + p_{adia} + p_{dip} + p_{T1}^{SS} + p_{T2}^{SS}). \tag{B.10}$$

The first term, $p_{off}^{SS} \sim \left(\frac{\Omega_i}{\Delta_g}\right)^2$, represents off-resonant excitations and cross-talk induced by microwave manipulations with Rabi frequency Ω_i. Here, Δ_g characterizes the gradient-induced splitting achieved within the super-plaquette frequency spectrum (Supplementary Methods of [82]). The second term, p_{adia}, corresponds to the non-adiabatic correction resulting from an optimized adiabatic ramp profile [182, 183, 184]. The third term, $p_{dip} \sim \left(\frac{\kappa}{\Omega_i}\right)^2$, is directly obtained from (eq. B.3) and corresponds to additional off-resonant errors. The fourth error term, p_{T1}^{SS} corresponds to the depolarization error induced by the finite NV T_1 time, while the final error term, p_{T2}^{SS} corresponds to the infidelity induced by dephasing. Since each error term is considered within the context of a single adiabatic SWAP, the total error contains an additional factor of N, representing the chain length, which is plaquette size dependent (e.g. $N \approx 5$ for 100nm and $N \approx 20$ for 500nm).

We can similarly consider the accumulated infidelity associated with FFST,

$$p_{err}^{FFST} \approx p_{off}^{FFST} + p_f + p_g + p_{T1}^{FFST} + p_{T2}^{FFST}. \tag{B.11}$$

In direct analogy to p_{err}^{SS}, the first term in p_{err}^{FFST} corresponds to the excitation of an NV reg-

ister by off-resonant microwave fields. The second term, p_f, corresponds to the undesired coupling with off-resonant fermionic modes. Since the coupling strength is characterized by $g/\sqrt{N}$ [174], while the splitting of the eigenenergy spectrum $\sim \kappa/N$, such an off-resonant error induces an infidelity $\sim (\frac{g/\sqrt{N}}{\kappa/N})^2$. The third error term, p_g, results from the protocol designed to control, g, the NV-chain coupling (see Materials and Methods of [82] for details). Finally, directly analogous to p_{err}^{SS}, the fourth and fifth terms correspond to errors induced by the operational time, t_{FFST}, which causes both depolarization and dephasing.

Finally, we perform numerical simulations, taking into account the Nitrogen JT frequencies, to characterize the infidelity of both the adiabatic sequential SWAP and FFST within the NV architecture, as depicted in Fig. B.5. The results of these calculations are in excellent agreement with the above theoretical predictions. In particular, these simulations reveal that, for sufficiently long $T_1^{NV} \sim 100$ms, operational infidelities in both DSCB methods can be kept below 10^{-2}.

These simulations clearly show that the T_1 time of the NV electronic spin is of critical importance in obtaining high-fidelity quantum operations. While at room temperature T_1 appears to vary depending on the particular sample and on the specific properties of the local NV environment, such as strain, values on the order of 10 ms are generally obtained [63, 179]. However, the spin-lattice relaxation mechanism governing T_1 is most likely related to an Orbach process [185, 186], which is strongly temperature dependent. In such a case, modest cooling of the sample by ≈ 50K, is likely to extend T1 by more than an order of magnitude, thereby making high fidelity gates possible.

Given that such numerical estimations suggest the possibility of achieving high fidelity

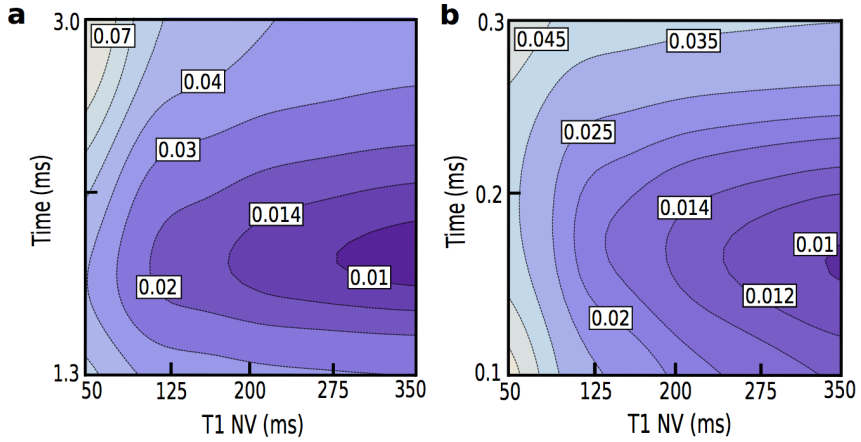

Figure B.5: | **Numerical simulation of the DSCB fidelity** (**a**) The operational infidelity associated with the adiabatic sequential SWAP for $N = 18$. The simulations account for the Jahn-Teller orientation of Nitrogen impurities and utilize the optimized adiabatic ramp profile [182]. Simulations utilize an optimized coupling strength of 8.71kHz (18.1nm spacing). Full numerical integration of the time dependent Schrödinger equation produces infidelity contour plots as a function of total SWAP time and T_1^{NV}. (**b**) Numerical simulations of the operational infidelity associated with FFST for $N = 7$. Non-nearest neighbor interactions are assumed to be refocused through dynamic decoupling. Simulations, which utilize an optimized coupling strength of 12.6kHz (16nm spacing), are based upon a full diagonalization and also account for the Jahn-Teller orientation of Nitrogen impurities. Infidelity contour plots are again shown as a function of total SWAP time and T_1^{NV}.

two-qubit operations between remote NV registers, the proposed architecture seems well suited to the implementation of topological quantum error correction. In particular, we imagine implementing a 2D surface code, which requires only nearest-neighbor two-qubit gates and single qubit preparation and measurement [187, 166, 188]. Recent progress in optimizing this surface code has yielded an error threshold of $\epsilon \approx 1.4\%$ [189], which is above the estimated infidelity corresponding to both the adiabatic sequential SWAP and FFST; thus, in principle, implementation of such a 2D surface code can allow for successful topological quantum error correction, and hence, fault tolerant quantum computation.

B.11 Discussion

The above considerations indicate the feasibility of experimentally realizing a solid-state quantum computer capable of operating under ambient conditions at or near room temperature. We emphasize that a majority of the elements required for the realization of individual qubits in our architecture have already been demonstrated. In our approach, these techniques are supplemented by both a new mechanism for remote register coupling between NV centers as well as a hierarchical design principle, which facilitates scalability. The remote coupling mechanisms discussed can naturally be implemented via Nitrogen ion implantation in ultra-pure diamond crystals and are robust to realistic imperfections and disorder [174]. Moreover, single errors during quantum state transfer are localized to individual transport channels and do not have a propagating effect on the remaining computation.

While we hope that the proposed architecture evinces the feasibility of room temperature quantum information processing, the implementation and integration of the various

proposed elements still require significant advances in areas ranging from engineering to materials science. Crucially, recent results have demonstrated substantial progress toward overcoming challenges such as the optimization of planar microcoil arrays [190, 191] and efficient beam steering in micromirror systems [192]. Furthermore, by eliminating requirements for cryogenic temperatures, our blueprint aims to make the realization of a scalable quantum computer significantly more practical.

The present work opens a number of new directions which can subsequently be explored. In particular, while we have considered the direct errors associated with DSCB mediated coupling, it is instructive to note that the fidelity of such quantum gates can often be significantly improved using techniques from optimal control theory [76, 193]. For example, such methods of optimal control, while negating the detrimental effects of decoherence, can also simultaneously allow for the implementation of high-fidelity gates despite both frequency and coupling disorder as induced by ion implantation errors. Indeed, the ability to precisely guide the quantum evolution via optimal control, even when the system complexity is exacerbated by environmental coupling, provides an alternative solution to improve single and two-qubit gate fidelities [194]. In addition, it is well known that the local strain field surrounding each NV center can significantly alter the register's properties; hence, through a detailed understanding of electric field induced strain, it may be possible to improve the coherence properties of the qubit. Moreover, the long coherence times of individual P1 centers, each of which harbor an associated nuclear spin, suggest the possibility of utilizing these dark spins as computational resources in and of themselves [195]. Beyond these specific applications, a number of scientific avenues can be explored, including for example, understanding and controlling the non-equilibrium dynamics of disordered spin

systems.

Appendix C

Supporting material of previous sections

C.1 Supporting material of Chapter 2

In this part of the thesis we present some of the details associated with the technical aspects of the results presented in Chapter 2. First, we give a detailed model for the nuclear dephasing and depolarization mechanism based on numerical simulations. Then we study the effects of homonuclear decoupling sequences on the nuclear coherence. Finally, we recapitulate the basic principles of process tomography and apply it to our experiments to derive Fig. 2.8. More additional material can be found in the online supplementary information of [196].

C.1.1 Detailed model nuclear coherence and depolarization

While the simplified model introduced in Section 2.4 captures the basic idea of the motional averaging in our system the discussed two level scheme is an oversimplification in the case of NV centers. To discuss the effects of an applied optical drive to the full extent

we choose a different approach. For this we incorporate 11 levels for the electronic state and the two levels for the ^{13}C nuclear spin as shown in Fig. C.1. Using a master equation we can simulate the nuclear decoherence. For the numerical solution of the master equation we assumed a secular approximation for the nuclear and electronic spin leaving us with an effective Hamiltonian for the hyperfine interaction $H_{hyp} = \left(A_{\parallel} I_z + A_{\perp} I_x\right) S_z$, which is justified since $A << g_e \mu_B B$. Moreover, we neglect any coherence between different electronic states since all our fields are classical.

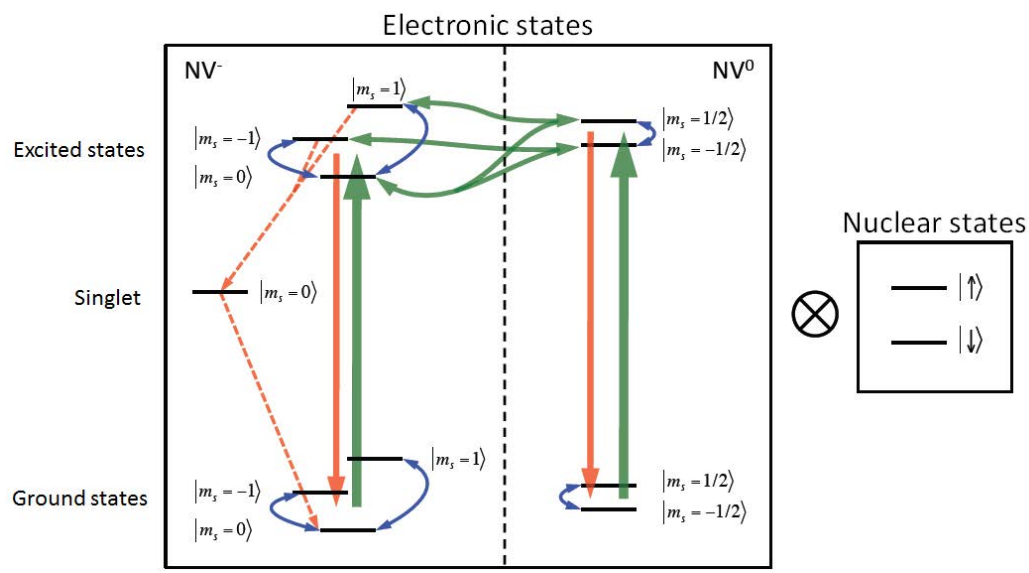

Figure C.1: | **Schematic level diagram** for an NV center (left box) and a ^{13}C nuclear spin (right box) under illumination with green laser light. The green arrows indicate optical transitions addressed by our green laser pulse, red arrows show electronic decay and blue arrows indicate depolarization of the electronic spin. The transition rates for NV$^-$ employed in our model are taken from [126] with the decay rate from the electronic excited state to the ground state $\tilde{\gamma} = \frac{1}{13\ ns}$, the decay rate from the singlet to $m_s = 0$ of the electronic ground state $\Gamma = \frac{1}{300\ ns}$ and the decay rate from the electronic excited state with $m_s = \pm 1$ to the singlet $\tilde{\gamma}_b = 0.3\tilde{\gamma}$. Moreover we assumed the decay rate of the excited state of NV^0 to be on the same order as for NV$^-$. The deionization rate from NV$^-$ to NV^0 is taken to be $\gamma_1 = \frac{I/I_{sat}}{70\ ns}$ and the ionization rate $\gamma_2 = 2\gamma_1$. The depolarization time for the electronic spin for NV$^-$ is taken to be $T_{1e}^{NV-} = 8ms$ and for the case of NV^0 $T_{1e}^{NV0} = 6us$ [41]. All the remaining rates are takes to be zero.

A solution of the master equation for the nuclear coherence time is shown in Fig. C.2a. As expected the coherence time scales linearly as a function of laser intensity when exceeding optical saturation. Furthermore at small laser intensities ($I \sim I_{sat}/1000$, with I_{sat} the saturation intensity) the coherence time has a local maximum originating from repolarization of the electronic spin without deionizing the NV center. This is possible to a certain extent since the (de)ionization process is a two photon process but the repolarization rate is linear in laser intensities for $I << I_{sat}$.

Even though the simplified two level model is able to qualitatively explain the linear scaling of the coherence as a function of laser intensity it does not quantitatively reproduce the T_2 (dashed-dotted black line). The deviation from the two level model originates from the fact that at large laser intensities other states beside the $m_s = 0$ and $m_s = \pm 1/2$ can be occupied.

Next we compare the solution of the master equation with the slope extracted from the experimental data in Fig. 2.7b). The slope is shown in Fig. C.2a by a dashed red line. The experimental data is in excellent agreement with the simulation based on the transition rates given in the caption of Fig. C.1 .

Since we know that this master equation allows us to quantitatively reproduce T_{2n} we can use the master equation to estimate a value for the perpendicular component of the hyperfine interaction $A_\perp$. Optimizing our fit we can find $A_\perp$ to be on the order of $(2\pi)1.8$ kHz as shown in Fig. C.2b. Except for laser intensities $<< I_{sat}$ the simulated T_{1n} times agree well with the measured data. Plugging $A_\perp = (2\pi)1.8$ kHz into the two level model in (eq. 2.2) yields a theoretical curve (black dashed-dotted line) showing a significant discrepancy with the measured data. If we neglect the contact term [40] of the hyperfine

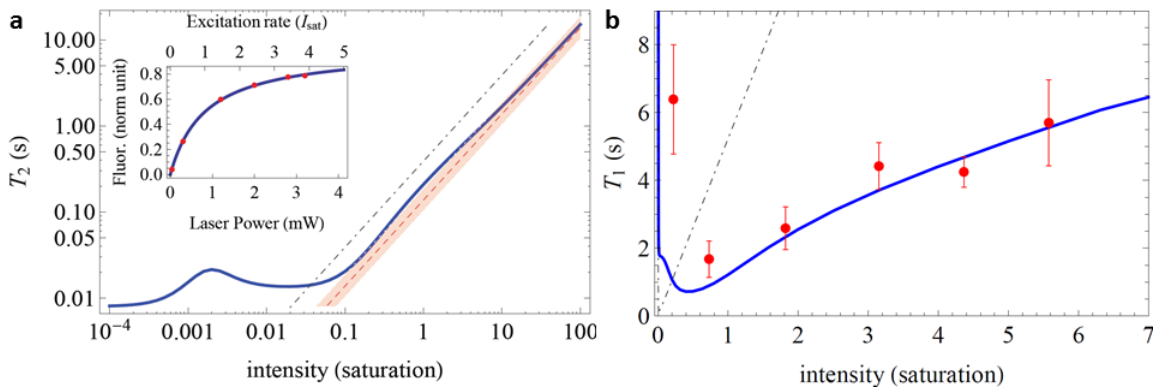

Figure C.2: | **Coherence and T_{1n} time of the ^{13}C nuclear spin** Solution of a master equation (blue) employing the level scheme and transition rates shown in Fig. C.1. **a** The initial slope extracted from the measured data is represented by the red dashed line with error bars (red area). To convert the measured slope from Fig. 2.7 from laser power (mW) to intensity in units of I_{sat} the saturation curve shown in the inset is used. The dahsed-dotted black line is the (eq. 2.6) with $A_{\parallel} = (2\pi)2.7$ kHz. **b** The red points show the measured nuclear T_{1n} times. The dashed-dotted black line is the solution of (eq. 2.2) with γ same as is the inset of **a** and $A_{\perp} = (2\pi)1.8$ kHz. The simulated blue line uses $A_{\perp}$ as a fitting parameter.

interaction A and assume only dipolar interaction we can estimate the distance between the electronic spin and the nuclear spin to be approximately 1.7 nm.

Nevertheless, our simplified two level model from (eq. 2.6) and (eq. 2.2) allows us by rescaling the hyperfine interaction and the (de)ionization rate γ to find effective rates that quantitatively reproduce the T_{1n} and T_{2n} times. As shown in Fig. 2.4 and 2.7e) using the rates $A_{\parallel}^{\text{eff}} = (2\pi)3.3$ kHz, $A_{\perp}^{\text{eff}} = (2\pi)1.0$ kHz and $\gamma = (2\pi)150 \times P_{\text{Laser}}$ kHz/mW reproduce the measured T_{1n} and T_{2n} as function of the laser power P_{Laser}.

C.1.2 Nuclear decoherence under dynamical decoupling

Figure 2.7d shows that the nuclear coherence time is significantly extended under the application of MREV-8, which suppresses the nuclear dipole-dipole interaction. Here we

provide further details on MREV-8 and identify the sources of residual decoherence.

MREV-8 dynamical decoupling

The Waungh, Huber and Haberlen four-pulse sequence (WHH), shown in Fig C.3a, decouples nuclear dipole-dipole interactions [197]. In our experiment we use the MREV-8 sequence, shown in Fig C.3b, which is an eight-pulse sequence made up of WHH cycles of alternating phase.

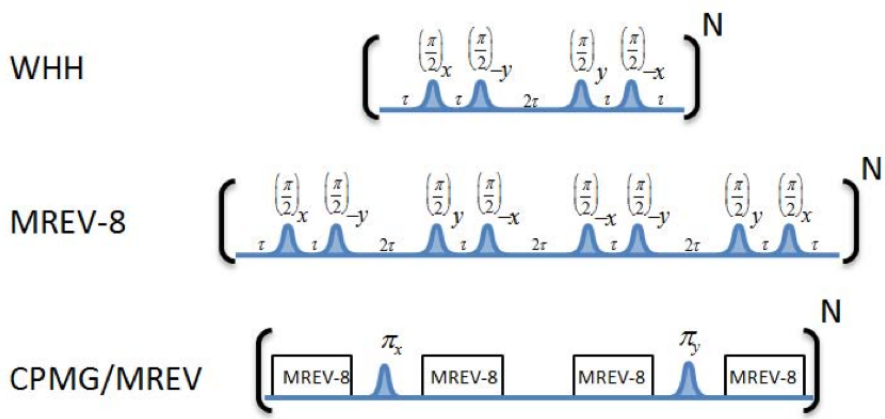

Figure C.3: | **Pulse sequences for decoupling** WHH sequence, showing four RF pulses around the indicated axes for dipole-dipole decoupling. MREV-8 sequence used for increased robustness against pulse errors in WHH. CPMG/MREV sequence adds decoupling from external magnetic field due to additional π-pulses.

The effect of MREV-8 on the dipole-dipole interaction can be understood using average Hamiltonian theory [197]. We describe the effects of the pulses by moving to an interaction picture (i.e. the toggling frame) with respect to the Hamiltonian defined by the $\pi/2$ rotations. Provided the characteristic frequencies ω of H satisfy $\omega t \ll 1$ we can perform a Magnus expansion, and describe the total time evolution during the cycle is described by

an effective Hamiltonian,

$$H_{\text{eff}} = H^{(0)} + H^{(1)} + H^{(2)} + ... \tag{C.1}$$

where the first few terms are

$$H^{(0)} = \sum_{j=1}^{M} H_j, \tag{C.2}$$

$$H^{(1)} = \frac{-i\tau}{2M} \sum_{k>j}^{M} \sum_{j=1}^{M} \left[H_k, H_j\right]. \tag{C.3}$$

Here, M is the total number of time intervals of length τ between pulses as shown in Fig C.3, and H_j is the interaction picture Hamiltonian in the toggling frame in interval j. The zeroth order effective Hamiltonian is just the average over the cycle in the toggling frame, and the nth terms in the expansion consist of nested commutators of order n.

Our goal is to find the effect of MREV-8 on the nuclear dipole-dipole interaction within secular approximation,

$$H_{\text{D}} = \sum_{j>k} D_{jk} \left(3I_j^z I_k^z - \mathbf{I}_j \cdot \mathbf{I}_k\right), \tag{C.4}$$

where the dipolar coupling frequency is $D_{jk} = \hbar^2 \gamma_n^2 \left[1 - 3\cos^2(\theta_{ij})\right] / r_{ij}^3$, and the memory nuclear spin is indexed by $j = 0$. The effective, average Hamiltonian is obtained in terms of the zeroth order effective spin operators under MREV-8,

$$I_x^{(0)} = \frac{2}{3} I_x \qquad I_y^{(0)} = \frac{1}{3} I_y \qquad I_z^{(0)} = \frac{1}{3}\left(I_x + I_z\right). \tag{C.5}$$

Applying (eq. (C.5)) to each nuclear spin, one immediately finds that the average dipole-dipole Hamiltonian is $H_D^{(0)} = 0$. Furthermore, from the first order term in the Magnus expansion of (eq. C.2) one finds that there is no first order correction, i.e. $H_D^{(1)} = 0$. Thus the leading order correction from the dipolar interaction is$(D\tau)^2 D \sim 10^{-4}$ Hz. Due to this

very high suppression we expect that nuclear dipolar coupling alone cannot account for the residual decoherence when MREV-8 is applied. Next we discuss the sources of residual decoherence in the limits of low and high laser power.

Effect of MREV-8 on decoherence from NV ionization

At low laser power, nuclear decoherence is dominated by the (de)ionization of the NV electronic spin as described by the fluctuator model in Section 2.4. Here we find the effect of MREV-8 on this source of decoherence; for simplicity we consider a simple two-state model. Within this model, the Hamiltonian of the nuclear memory spin is

$$H_A = f(t)\left[A_\parallel I_z + A_\perp\left(I_x\cos\phi + I_y\sin\phi\right)\right], \tag{C.6}$$

where $f(t)$ describes telegraph noise with switching rate γ. In the absence of MREV-8 it is straightforward to calculate the resulting decoherence. A Fermi's golden rule calculation yields the depolarization rate in the limit $\gamma \gg \omega_L$,

$$\Gamma_1 = \frac{1}{8\gamma}A_\perp^2, \tag{C.7}$$

which is set by the coefficients of I_x and I_y. We calculate the dephasing rate within the Gaussian approximation, justified since $A_\parallel\tau \ll 1$, yielding

$$\Gamma_\phi = \frac{1}{8\gamma}A_\parallel^2, \tag{C.8}$$

which is set by the coefficient of I_z.

Next we find how MREV-8 modifies the decoherence from NV ionization. Here we cannot apply average Hamiltonian theory because the Hamiltonian fluctuates rapidly between $\pi/2$ pulses. Nonetheless, we can make use of the fast switching rate, since in the

relevant limit $\gamma\tau \gg 1$, the fluctuations $f(t)$ are uncorrelated between one interval and the next. As a result, the total decoherence rate during one cycle is simply the incoherent average of the decoherence rates during each interval. The total dephasing rate is thus $\Gamma_\phi = \frac{1}{M}\sum_j^M \Gamma_{\phi,j}$ and the depolarization rate is $\Gamma_1 = \frac{1}{M}\sum_j^M \Gamma_{1,j}$, where the rates during each interval j are obtained from the Hamiltonian H_j in the toggling frame, and using the same calculations as described above in the absence of MREV-8. When MREV-8 is applied we obtain

$$\Gamma_\phi = \frac{1}{24\gamma}\left[A_\parallel^2 + 2A_\perp^2 \sin^2\phi\right], \tag{C.9}$$

$$\Gamma_1 = \frac{1}{24\gamma}\left[A_\perp^2 + 2\left(A_\parallel^2 + A_\perp^2\cos^2\phi\right)\right]. \tag{C.10}$$

The coefficients which previously led to pure dephasing or depolarization become mixed due to the $\pi/2$ rotations of MREV-8.

The total transverse decoherence rate $\Gamma_2 = 1/T_2$ includes contributions from both dephasing and depolarization, and can be approximated by $\Gamma_2 = \frac{1}{2}\Gamma_1 + \Gamma_\phi$. From the above results the total decoherence rates with and without MREV-8 are

$$\Gamma_2 = \frac{1}{8\gamma}\left[A_\parallel^2 + \frac{1}{2}A_\perp^2\right] \qquad \text{(without MREV-8)} \tag{C.11}$$

$$\Gamma_2 = \frac{1}{8\gamma}\left[\frac{2}{3}A_\parallel^2 + \frac{1}{2}A_\perp^2\left(1 + \frac{2}{3}\sin^2\phi\right)\right] \qquad \text{(with MREV-8)} \tag{C.12}$$

From the fit of our T_1 data (see Fig. 2.4d) we found $A_\perp/2\pi \sim 1.0$ kHz and $\gamma/2\pi \sim 300$ kHz. Using this value of γ, our T_2 data (see Fig. 2.7) this yields $A_\parallel/2\pi \sim 3.3$ kHz. Inserting these values into (eq. C.11) and (eq. C.12) we find that the slope of T_2 versus laser power, at low power, is expected to be a factor $\sim 3/2$ larger when MREV-8 is applied. This simple estimate predicts that the decoherence from NV ionization is only slightly affected by MREV-8, in qualitative agreement with the data (see Fig. 2.7). However, the data shows

that the impact of MREV-8 on the decoherence at low power is even smaller than the above prediction. This implies that in practice the total decoherence is slightly larger than obtained by incoherently averaging over each time interval, and as a result MREV-8 has almost no impact on the decoherence at low power.

Residual decoherence due to finite detuning

Lastly, we consider the residual decoherence under MREV-8 at high laser power where the ionization-induced decoherence is suppressed by motional averaging. As discussed above, decoherence due solely to the dipolar interaction is strongly suppressed by MREV-8, in particular the terms in the effective Hamiltonian to zeroth and first order in $D\tau$ vanish. However, the presence of small but finite detuning of our RF pulses leads to slightly imperfect dipolar cancelation; for the longest times measured, this small detuning is sufficient to reintroduce the dipolar Hamiltonian through cross terms. This combined effect appears at first and higher orders in the effective Hamiltonian and sets the limit on T_2 in the present experiment.

Before discussing the combined effect of detuning and dipolar coupling, we consider the possibility of decoherence due to the detuning alone, in the absence of the dipolar interaction. The frequency resolution of our RF pulses is ~ 10 Hz, which means that a finite detuning of this order is expected. Constant detuning has no direct consequence since it is echoed out by the CPMG sequence in which MREV-8 is embedded. However, slow drifts in the detuning on the order of this frequency resolution could in principle lead to decoherence. From a measurement of $\delta(t)$ we estimate the rms fluctuation amplitude of $\delta_{\mathrm{rms}}/2\pi \sim 10$ Hz and correlation time of $T_c \sim 350$ s. Estimating the impact of MREV-8

using the zeroth order term in (eq. C.2), we modify this by $\delta_{\rm rms} \to \delta_{\rm rms}/3$. Using these values and estimating $T_2 \sim \sqrt[3]{12N^{2/3}T_c(2\pi/\delta_{\rm rms})^2}$ for pure dephasing we find $T_2 \sim 27$ s from the detuning fluctuations. This suggests that slow detuning fluctuations are not directly the cause of the observed residual decoherence.

We now turn to the combined effect of finite detuning and dipolar coupling which appears to dominate the residual decoherence observed at high laser power. Dipolar coupling is described by (eq. C.4), and the Hamiltonian due to finite detuning δ is

$$H_\delta = -\delta \sum_j I_z^j \tag{C.13}$$

in the frame rotating at the RF frequency. Applying the Magnus expansion of (eq. C.2) the nth term in the effective Hamiltonian contains frequencies of order

$$\omega_n = \left[(\delta + D)\tau\right]^n (\delta + D). \tag{C.14}$$

For the longest coherence times measured, the interval between $\pi/2$ pulses is $\tau_{\rm max} \sim 20$ ms, which yields $\delta\tau_{\rm max} \sim 1$. Accordingly, we can no longer truncate the Magnus expansion to low order; specifically, the terms $(\delta\tau)^n D$ contribute to high order. This is the most important term, because terms involving only δ are echoed out by CPMG. Thus the effective decoherence time is set by the value of τ for which $\delta\tau \sim 1$. We have performed a simple numerical calculation to support this conclusion. In Fig. C.4 we show the signal calculated using parameters provided in the caption. We obtain an effective $T_2 \sim 2$ s, in good agreement with the experiment.

Limits to coherence time

The lifetime of our proposed nuclear spin quantum memory is limited by a combination of optically induced dephasing, Γ_{opt} (eq. 2.6), and interactions with the remaining spins in

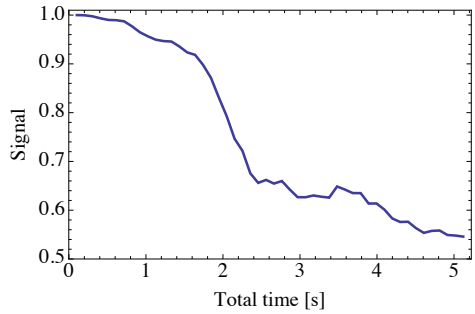

Figure C.4: | Signal calculated numerically for 5 bath nuclear spins distributed around the central nuclear spin, assuming 0.01% ^{13}C nuclear spins in the diamond lattice. We assumed constant detuning $\delta/2\pi = 10$ Hz, and averaged over 50 random placements of the surrounding.

the surrounding ^{13}C environment, Γ_{bath}. Since Γ_{opt} is proportional to A^2, a slight reduction in strength of the hyperfine interaction increases the coherence time significantly. Upon reducing the ^{13}C concentration by an order of magnitude, it is possible to initialize and readout a nuclear spin coupled with strength, $A \sim (2\pi)0.5$ kHz. Furthermore, lowering the ^{13}C concentration will also result in a reduction of the nuclear-nuclear induced decoherence, that scales quadratically with the ^{13}C concentration.

C.1.3 Process tomography and fidelity

In this section we will in detail discuss how the performance of our memory is measured. For this we will explain the way we characterize the system's evolution using process tomography. Finally, we discuss our quantum memory in terms of fidelity.

To analyze the performance of our quantum memory we are interested in the full evolution of the ^{13}C nuclear spin during the storage process. One way to fully characterize the

system's evolution $\mathcal{E}(\rho)$ is given by the Kraus map

$$\mathcal{E}(\rho) = \sum_{i,j=0}^{d^2-1} \chi_{i,j}(t) A_i \rho A_j^\dagger, \tag{C.15}$$

with ρ being the density matrix describing our ^{13}C nuclear memory, A_i a basis of operators acting on ρ and $d = 2$ the dimension of our system. The matrix χ is positive hermitian, time dependent and fulfills the trace-preservation relation $\mathbb{1} = \sum_{i,j} \chi_{i,j} A_i A_j^\dagger$.

For $d = 2$ we have to determine 12 parameters which determine χ. Process tomography is a tool to measure these parameters by preparing the nuclear spin in 4 different basis states ($|\downarrow\rangle$, $|x\rangle$, $|y\rangle$ and $|\uparrow\rangle$, with $|x\rangle = (|\downarrow\rangle + |\uparrow\rangle)/\sqrt{2}$ and $|y\rangle = (|\downarrow\rangle + i|\uparrow\rangle)/\sqrt{2}$) followed by a state tomography after a certain storage time (Fig. C.5)

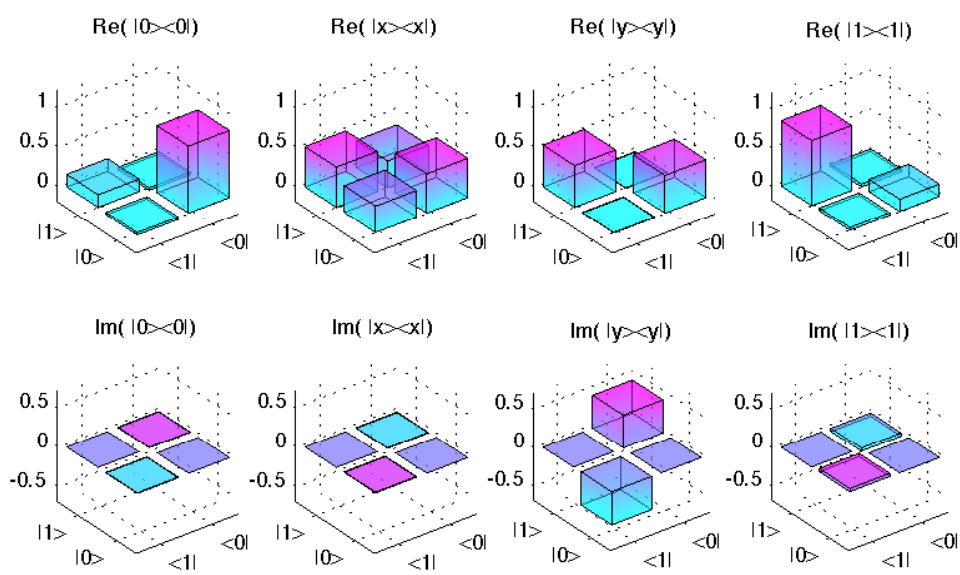

Figure C.5: | **State tomography** The states shown in the figure are $|\downarrow\rangle$, $|x\rangle$, $|y\rangle$ and $|\uparrow\rangle$ after 1 s of storage time.

For the given states, we can reconstruct a matrix $\tilde{\chi}$ that fulfills the Kraus map from (eq. C.15). In the basis $A_i = \{\mathbb{1}, \sigma_x, \sigma_y, \sigma_z\}$ the matrix $\tilde{\chi}$ can be reconstructed by using the

linearity of $\mathcal{E}$ and the identity

$$\begin{aligned}
\rho_1' &= \mathcal{E}(|\downarrow\rangle\langle\downarrow|)\ ;\ \rho_4' = \mathcal{E}(|\uparrow\rangle\langle\uparrow|) \\
\rho_2' &= \mathcal{E}\left(|x\rangle\langle x| - i|y\rangle\langle y|\right) - \frac{(1-i)}{2}(\rho_1' + \rho_4') \\
\rho_3' &= \mathcal{E}\left(|x\rangle\langle x| + i|y\rangle\langle y|\right) - \frac{(1+i)}{2}(\rho_1' + \rho_4') \\
\tilde{\chi} &= \frac{1}{4}\begin{pmatrix} \mathbb{1} & \sigma_x \\ \sigma_x & -\mathbb{1} \end{pmatrix}\begin{pmatrix} \rho_1' & \rho_2' \\ \rho_3' & \rho_4' \end{pmatrix}\begin{pmatrix} \mathbb{1} & \sigma_x \\ \sigma_x & -\mathbb{1} \end{pmatrix},
\end{aligned} \tag{C.16}$$

which are outlined in [198].

However, the $\tilde{\chi}$ matrix derived this way does not necessarily describe a physical process since a noisy signal may produce a $\tilde{\chi}$ that does not satisfy hermiticity and completeness. To find a χ that satisfies these requirements we apply a most likelihood procedure. This allows us to find a χ which is most likely to produce the observed experimental signal p (a description of this procedure is given in [199]). In the most likelihood estimation we parametrized χ by $\chi(\overrightarrow{q})$ to ensure non-negativity and hermiticity[200].

$$\chi(\overrightarrow{q}) = \frac{Q^\dagger Q}{Tr\left[Q^\dagger Q\right]}, \text{ with } Q = \begin{pmatrix} q_1 & 0 & 0 & 0 \\ q_5 + iq_6 & q_2 & 0 & 0 \\ q_{11} + iq_{12} & q_7 + iq_8 & q_3 & 0 \\ q_{15} + iq_{16} & q_{13} + iq_{14} & q_9 + iq_{10} & q_4 \end{pmatrix} \tag{C.17}$$

Using this parametrization for χ we can now minimize the square residual function defined by

$$\begin{aligned}
S(\overrightarrow{q}) = &\sum_{a=1}^{d^2}\sum_{b=1}^{d^2-1}\left(p_{a,b} - \sum_{n,m=0}^{d^2-1}\chi_{n,m}(\overrightarrow{q})\langle\varphi_b|A_n|\phi_a\rangle\langle\phi_a|A_m^\dagger|\varphi_b\rangle\right)^2 \\
&+ \lambda\left(\sum_{m,n,k=0}^{d^2-1}\chi_{n,m}(\overrightarrow{q})Tr\left(A_m A_k A_n\right) - \delta_{k,0}\right),
\end{aligned} \tag{C.18}$$

where $p_{a,b}$ denotes the measurement outcome for a state prepared in $|\phi_a\rangle$ ($|\phi_a\rangle = \{|\downarrow\rangle, |\uparrow\rangle, |x\rangle, |y\rangle\}$) and projected on $|\varphi_b\rangle$ ($|\varphi_b\rangle = \{|\downarrow\rangle, |x\rangle, |y\rangle\}$). The second part of the formula constrains $\chi(\overrightarrow{q})$ to be completely positive, with λ a parameter to describe the degree of positivity (a way to find a good starting point $\overrightarrow{q}_0$ is described in ref. [200]).

Using this most likelihood procedure we can find a χ matrix

$$\chi = \begin{pmatrix} 0.81 & -.02i & -0.01-0.01i & -0.01i \\ 0.02i & 0.02 & 0 & 0.02+0.01i \\ -0.01+0.01i & 0 & 0.14 & 0 \\ 0.01i & 0.02-0.01i & 0 & 0.03 \end{pmatrix}. \tag{C.19}$$

that is associated with our experimental observations. By using a Monte Carlo simulation we can estimate the error bars associated with the χ matrix found from our most likelihood procedure

$$\delta\chi = \begin{pmatrix} 0.08 & 0.01+0.04i & 0.01+0.01i & 0.01+0.02i \\ 0.01-0.04i & 0.06 & 0.01+0.01i & 0.01+0.01i \\ 0.01-0.01i & 0.01-0.01i & 0.04 & 0.01+0.01i \\ 0.01-0.02i & 0.01-0.01i & 0.01-0.01i & 0.04 \end{pmatrix}. \tag{C.20}$$

For this χ matrix all the off diagonal elements are zero within the error bars indicating that $\{\mathbb{1}, \sigma_x, \sigma_y, \sigma_z\}$ is a eigen-basis. In this form the Kraus operators have the physical interpretation of quantum channels. That the largest contribution in χ with $(81 \pm 8)\%$ is associated with the identity $\mathbb{1}$ as expected for a memory. The error channels are $(14 \pm 4)\%$ for phase-bit flip error σ_y, $(2\pm6)\%$ for bit flip σ_x and $(3\pm4)\%$ for phase flip σ_z error. In the case of only a depolarization channel one would expect an equal distribution between σ_x, σ_y and σ_z. This mismatch can be explained by taking a finite detuning in the RF transition frequency and the fixed chirality of the MREV-8 sequence into consideration.

As discussed in [147] diagonalizing χ allows us to extract a master equation under the assumption that the noise environment is Markovian. The average fidelity calculated based on the solution of the master equation is shown in Fig. C.6. The results of the extracted master equation are in agreement with the recorded data (blue points) within statistical errors.

The process fidelity F_p associated with the Kraus map χ is defined [199] by $F_p = \mathrm{Tr}(\chi \cdot \chi_{id}) = \chi_{00}$, where χ_{id} is the process matrix representing the identity. Using the relationship [201] between process fidelity F_p and average fidelity $\overline{F} = (d \cdot F_p + 1)/(d+1)$ we find $\overline{F} = (87 \pm 5)\ \%$.

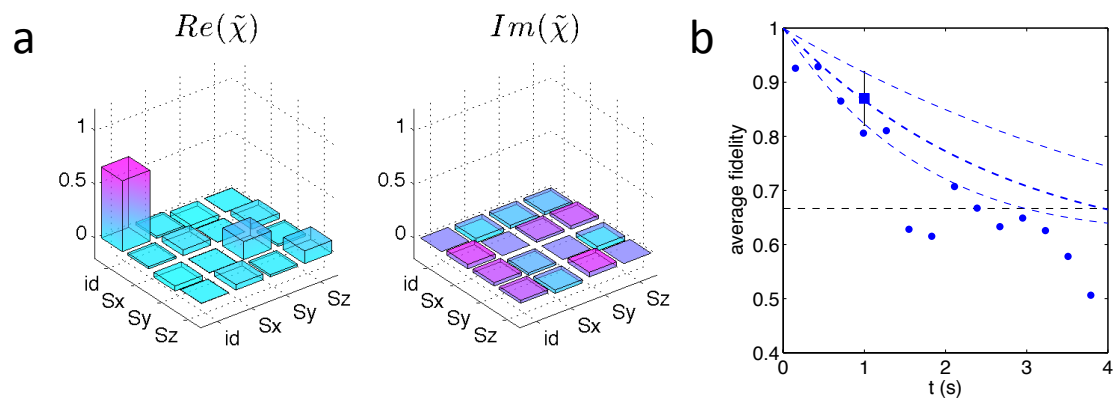

Figure C.6: | **Estimated $\tilde{\chi}$ matrix (a)** Initial reconstruction of the $\tilde{\chi}$ matrix. **(b)** The blue points are the measured average fidelity from Fig 2.8a. The blue square represents the average fidelity calculated from the χ matrix. The blue dashed line is the average fidelity extracted from the master equation corresponding to blue square.

C.2 Supporting material of Chapter 4

In this section of the appendix we provide supporting material related to Chapter 4. Specifically, we derive an analytical expression for the limit of the spin imaging resolution

when taking imperfections in the Laguerre-Gaussian mode into account. Furthermore, we discuss how our sub-diffractional imaging technique allows for a nanoscale measurement of magnetic fields. We also elaborate on the normalization procedure applied in Chapter 4 to demonstrate individual coherent spin control. Further supporting material can be found in the supplementary of [105].

C.2.1 Imaging resolution under imperfections of the Laguerre-Gaussian mode

In the derivation of (eq. 4.1) the ultimate resolution is determined by the maximum values of the pumping rate $\Gamma = \gamma\epsilon$ and the repolarization time $T_D \sim T_1$, as derive in Chapter 4.4. While in principle this would lead to an $\sqrt{\epsilon\gamma T_1}$ improvement in resolution relative to the diffraction limit in practice imperfections in the Laguerre-Gaussian mode are setting a limit. Specifically, in our experiments, the resolution is limited by a small imperfection of the doughnut-zero intensity. We can find the maximum achievable resolution by using a model that includes a back pumping process which brings the electronic spin from the $m_s = 0$ to the $m_s = 1$ state, and finite spin lifetime. Consider the rate equations of our two level system ($m_s = 0$ and $m_s = 1$),

$$\frac{dn_0}{dt} = R_x n_1 - \gamma_{0\to1}(n_1 - n_0) \tag{C.21}$$

and $n_1 = 1 - n_0$. The solution for this equation is,

$$n_1 = \frac{\gamma_1 + R_x}{2\gamma_{0\to1} + R_x}(1 - e^{-(2\gamma_{0\to1}+R_x)t_D}) \tag{C.22}$$

The resolution δr is defined by the FWHM condition $n_2(R_{r/2}, t) = \frac{1}{2}n_2(R_0, t)$. The maximum improvement in resolution relative to the diffraction limit of a confocal microscope

is given by

$$\Delta r/r_C = \sqrt{R_0/\Gamma}\sqrt{1 + 2\gamma_{0\to1}/R_0} \tag{C.23}$$

for an optimal doughnut duration $t_D = \log[(3\gamma_{0\to1} + 2R_0)/(\gamma_{0\to1} + R_0)]/(2\gamma_{0\to1} + R_0)$, where $\gamma_{0\to1}$ is the total rate out of the electronic spin $m_s = 0$. In the limit of long spin lifetime ($\gamma_{0\to1} \ll R_0$), the maximum improvement in resolution is given by $\sqrt{R_0/\Gamma} = \sqrt{\kappa_0/\kappa}$, i.e., the intensity of the doughnut center relative to the maximum doughnut intensity. In our experiments, $\kappa_0/\kappa \approx 1\%$, which is in a good agreement with our 10-fold improvement in resolution relative to the diffraction limit.

To demonstrate the nanoscale resolving power of our spin sensitive far-field optical technique, we imaged NV centers in bulk diamond separated by less than the diffraction limit. Figure C.7a shows a pair of individual NV centers that cannot be resolved using confocal microscopy. However, an optically detected ESR measurement performed in this location displays multiple spectral lines (Figure C.7b), indicating the presence of multiple NV centers with different crystallographic orientations relative to the applied static magnetic field. Using our sub-diffraction spin detection technique and scanning the microwave frequency, we associated each ESR spectral line with the corresponding location of an individual NV center with sub-diffraction limited resolution (Figure C.7c). In particular, sub-diffraction spin imaging scans along the trajectory indicated in Fig. C.7a, taken for each ESR transition frequency, reveal that two NV centers are responsible for the observed ESR spectrum: each NV center has two spectral ESR lines corresponding to the $|0\rangle \to |+1\rangle$ and $|0\rangle \to |-1\rangle$ transitions.

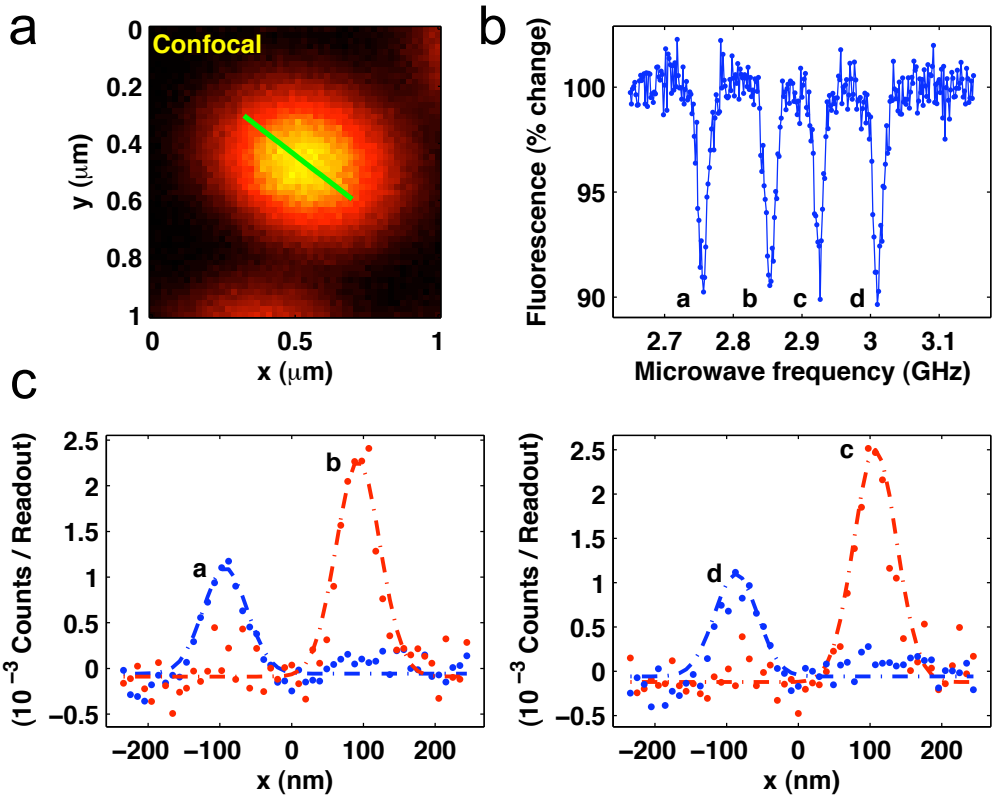

Figure C.7: | **Demonstration of sub-diffraction optical imaging of neighbouring NV centers.** A Closely spaced NV centers cannot be resolved using conventional standard imaging. B Optically-detected ESR spectrum with an applied DC magnetic field of 60 G indicates presence of two NV centers with different crystallographic orientations. C Individual NV centers are imaged with sub-diffraction resolution by scanning along the trajectory indicated in A. Each 1D image is obtained by selectively driving corresponding ESR resonance (A-D) with resonant microwave pulse followed by application of doughnut beam and optical readout. Each ESR spectral signature is thereby uniquely associated with its spatial location. Resonances a,c correspond to $|0\rangle \rightarrow |\pm 1\rangle$ transitions of one NV center, while resonances b,d are corresponding transitions for a second NV center.

C.2.2 Measurements of local magnetic field environment with sub-diffraction resolution

As described, individual NV centers can be resolved, independently manipulated and read-out using our technique. Here we individually measure the response of two NV centers to their local magnetic environment using Rabi and spin-echo techniques. By placing the center of the doughnut over one NV center, the other NV center is polarized and only contributes a constant background to the fluorescence signal. Figure C.8 shows the raw data for Rabi measurements of the two NV centers in Figure 4.3 when the doughnut zero is placed over Center 1 (upper-left panel) and Center 2 (bottom-left panel). When the two curves are added together (green line, right panel), the confocal measurement (taken at the position of Center 1) is recovered (dotted line in Figure C.8).

The observed modulations of the Rabi oscillations shown in Figure 4.3c (and Figure C.8) reveal the different magnetic fields experienced by each NV center. These modulations are caused by hyperfine induced splitting in the NV center's electronic transition ($m_s = 0 \rightarrow 1$) associated with the ^{15}N nuclear spin ($I = \frac{1}{2}$). A simple model for the probability of finding the electronic spin in the $m_s = 0$ state, P_0, assumes that on average the ^{15}N nuclear spin is half of the time in its spin down state and the other half of the time in its spin up state. Thus, P_0 is just the average of the dynamics of two two-level systems with different splittings. For a two-level system with states $|0\rangle$ and $|1\rangle$, Rabi frequency Ω and detuning δ, the probability to find the system in state $|1\rangle$ (starting from state $|0\rangle$) is given by $(\frac{\Omega}{\Omega_e})^2 \sin^2 \Omega_e \tau$, where $\Omega_e^2 = \Omega^2 + \delta^2$. Therefore, P_0 in our case is given by

$$P_0 = \frac{1}{2}\left(2 - \left(\frac{\Omega}{\Omega_1}\right)^2 \sin^2(\Omega_1 \tau/2) - \left(\frac{\Omega}{\Omega_2}\right)^2 \sin^2(\Omega_2 \tau/2)\right) \tag{C.24}$$

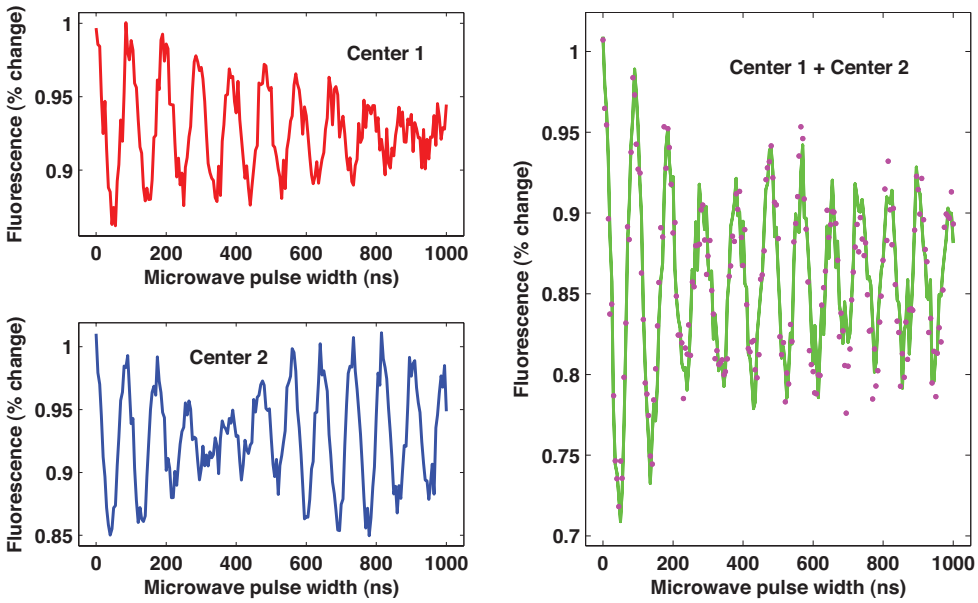

Figure C.8: | **Realization of spin-RESOLFT Rabi measurements**. Rabi oscillations for each NV center were measured by centering the doughnut on one of the NV centers. The addition of the two Rabi oscillation data curves (green line, right panel) corresponds to the confocal measurement of both NV centers as expected (pink dots, right panel).

where $\Omega_1^2 = \Omega^2 + \delta_1^2$ and $\Omega_2^2 = \Omega^2 + \delta_2^2$. If $\Omega \gg \delta$, the modulation frequency is given by $\Delta\Omega = \Omega_2 - \Omega_1 \approx (\delta_1 + \delta_2)(\delta_1 - \delta_2)/2\Omega$. Since $\delta_1 + \delta_2 = 2(f_0 - f)$ and $\delta_2 - \delta_1 = A$, the modulation frequency for an NV center is given by $\Delta\Omega = (\nu_0 - \nu)A/\Omega$, where ν_0 is the frequency of the electronic transition $m_s = 0 \rightarrow 1$, ν is the microwave frequency and $A = 3.05$ MHz[202] is the hyperfine splitting induced by the ^{15}N nuclear spin present on each of our NV centers.

Modulations appear when the microwave frequency is detuned from the central transition $\nu_0^i = \Delta + \gamma_e B^i$, where B^i is the local magnetic field along the NV axis of center i, Δ is the zero-field splitting, and γ_e is the gyromagnetic ratio of the electronic spin. In other words, modulations appear when the two hyperfine transitions are driven with different detunings. The difference in the modulation frequencies of each NV center ($\Delta\Omega_2 - \Delta\Omega_1 = 1.3 - 0.5 = 0.8$ MHz) reveals a difference in the static magnetic field experienced by each NV center of about $\Delta B = 1$ G.

Spin echo measurements can reveal even more subtle differences in the local environment between the two NV centers. In our measurements (Fig. 4.3d), the dominant contribution comes from interactions between the electronic spin of the NV center and the ^{15}N nuclear spin and ^{13}C nuclear spin bath. The spin echo signal can be written as [44] $p(\tau) = \frac{1+S(\tau)}{2}$, where $S(\tau)$ is the pseudo spin which can be written as the multiplication of all individual nuclear spin contributions. The first collapse and first revival of the NV spin echo signal can thus be approximated by

$$S(\tau) = S_{^{15}N}(\tau)\left(e^{-(\tau/\tau_C)^4} + ce^{-((\tau-\tau_R)/\tau_C)^4}\right), \tag{C.25}$$

where we have phenomenologically grouped the effect of all ^{13}C nuclear spins in the exponential decays, and where τ_C is the collapse rate[44] given by $\tau_C = 13\mu\mathrm{s}\sqrt{\frac{5\mathrm{G}}{B}}$, B is the

local magnetic field, τ_R is the revival time, c is the contrast of the first revival. The pseudo spin for the ^{15}N nuclear spin is given by

$$S_{^{15}N}(\tau) = 1 - \frac{|\Omega_{^{15}N,0} \times \Omega_{^{15}N,1}|^2}{|\Omega_{^{15}N,0}|^2 |\Omega_{^{15}N,1}|^2} \sin(\Omega_{^{15}N,0}\tau/2)^2 \sin(\Omega_{^{15}N,1}\tau/2)^2, \tag{C.26}$$

where $\Omega_{^{15}N,m_s}$ is the Larmor frequency of ^{15}N when the electron is in state m_s. The blue lines in Figure 4.3d are fitted to equation (eq. C.25). While Center 2 shows good coherence ($c = 0.86$), Center 1 shows no revival of the signal ($c = 0$). The absence of revival for Center 1 can be due to an unfavorable distribution of nearby pairs of ^{13}C nuclear spins that quickly decohere the electronic spin [23], or due to nearby paramagnetic impurities or other defects. The position of the first revival for Center 2, $\tau_R = 13.5$ μs, is set by the Larmor precession of ^{13}C, $\tau_R^{-1} = \omega_{C13} = \gamma_{C13} B$, corresponding to a local magnetic field of B = 69 G. The high frequency oscillations ($\Omega_{^{15}N,1}$) correspond to the hyperfine interaction between the electronic spin and the ^{15}N nuclear spin, $\Omega_{^{15}N,1} \approx A = 3.05$ MHz. Meanwhile the slow frequency component of the dynamics, $\Omega_{^{15}N,0} = 360$ kHz, corresponds to the Larmor frequency of the ^{15}N nuclear spin when the electron is in state $m_s = 0$. We immediately notice that the slow frequency component is too large to be explained by the bare Larmor frequency of ^{15}N at 69 G, $\gamma_{N15} B = 30$ kHz. This slow frequency component $\Omega_{^{15}N,0}$ is enhanced by virtual transitions between the NV electronic spin and the ^{15}N nuclear spin. To understand this effect, we first introduce the following Hamiltonian that governs the dynamics,

$$H = \Delta S_z^2 - \gamma_e B \cdot S - \gamma_n B \cdot I - S \cdot A \cdot I \tag{C.27}$$

where $\Delta = 2.87$ GHz is the zero field splitting, γ_e (γ_n) is the electronic (nuclear) gyromagnetic ratio, B is the magnetic field and A is the hyperfine tensor. This Hamiltonian leads

to very interesting effects such as enhancement of the g-factor [44] and assisted interaction between nearby nuclei [5]. Here we only analyze the relevant effect for our experiments, the enhancement of the g-factor. In the spirit of second order perturbation theory, we can divide Hamiltonian (eq. C.27) in two parts, the secular part

$$H_0 = \Delta S_z^2 - \gamma_e B_z S_z - \gamma_n B \cdot I - S_z A_z \cdot I \tag{C.28}$$

and the non-secular part

$$V = -\gamma_e (B_x S_x + B_y S_y) - (S_x A_x + S_y A_y) \cdot I. \tag{C.29}$$

By using perturbation theory to second order, we can determine that the enhancement in the interaction between the magnetic field and the nuclear spin can be written as $B \cdot \Delta g \mu_N / \hbar \cdot I$, where μ_N is the nuclear magneton and Δg is the enhanced g-tensor given by

$$\Delta g = -(3|m_s| - 2)\frac{g_n \gamma_e}{\Delta \gamma_n} \begin{pmatrix} A_{xx} & A_{xy} & A_{xz} \\ A_{yx} & A_{yy} & A_{yz} \\ 0 & 0 & 0 \end{pmatrix}$$

In the case of ^{15}N, the hyperfine interaction is isotropic [202] and the enhancement is given by $\Delta g^0 \approx 7.8$ (corresponding to a gyromagnetic increment factor of $2(\gamma_2/\gamma_n)A/\Delta \approx 14$). Therefore, $\Omega_{^{15}N,0} \approx 14\gamma_n B_\perp$ corresponding to a perpendicular field to the NV axis of $B_\perp = 60$ G. This value is in agreement with the component of the magnetic field parallel to the NV axis that leads to the observed splitting in the ESR spectrum (Figure 4.3a), $B_{||} = 36$ G ($B = \sqrt{36^2 + 59^2} \approx 69$ G).

C.2.3 Coherent single spin manipulation

We performed selective coherent spin manipulation on two NV centers with a spatial separation of approximately 150 nm. To verify that Center 1 can undergo coherent Rabi oscillations while Center 2 is kept in the $m_s = 0$ state, two experiments using pulse sequences S3 and S4 in Fig. 4.4 were performed. If Center 2 remains in the $m_s = 0$ state, a constant signal is expected for the difference of the measurements made with these sequences.

In this subtraction procedure we accounted for contrast reduction in the spin-RESOLFT readout of Center 1 by multiplying the results of sequence S4 by $\frac{1}{0.75}$. (This weighting factor is determined from a separate experiment, in which both centers were prepared in the state $m_s = 1$ and imaged with spin-RESOLFT). The signals were normalized relative to the unperturbed Rabi oscillation signal for Center 1.

The observed sub-diffraction suppression of coherent spin transitions can be used to manipulate quantum information stored in the nuclear spins associated with each NV center. Specifically, we can use this sub-diffraction inhibition to prepare, coherently manipulate, and detect the nuclear spin of Center 1 (in the doughnut center) without perturbing the nuclear spins of Center 2 and of other nearby centers. The error induced on the nuclear spin associated with Center 2 during a π-pulse on Center 1 can be estimated from our measurements as $P_e \approx \left(\frac{\gamma}{\kappa+\gamma}\right)\left(\frac{\pi\Omega}{2\kappa}\right)$, where κ is evaluated at Center 2 and where $\gamma \approx \frac{1}{13ns}$ is the decay rate of the optically excited state. In addition to the dephasing described above, this takes into account the fact that application of the green doughnut beam "hides" some population in the excited state. For values of $\kappa \sim \gamma$ and $\Omega = (2\pi)2.3$ MHz, this error would be $p_e \approx 0.1 \ll 1$, indicating that the state of the nuclear spin associated with Center 2 can be well preserved while we manipulate Center 1.

C.2.4 Measurement of individual spin states in coherent manipulation experiments

In Fig. 4.3b, we demonstrate that a green doughnut-shaped laser beam inhibits electronic-spin Rabi oscillations for one of two NV centers separated by 150 nm. As seen in this figure, NV Center 1, which sits at the zero intensity point of the doughnut, undergoes spin Rabi oscillations; while Center 2, sitting outside the center of the doughnut, remains in the $m_S = 0$ state. In order to probe this behavior, two experiments (pulse sequences S3 and S4 in Figure 4.3b) were performed to extract the probability of each center remaining in the initial state $m_s = 0$. Here we present the details of our analysis.

Intuitively, the experimental sequence S3 results in the readout of both spin states simultaneously, while the experimental sequence S4 (involving spin-RESOLFT readout) results in the detection of Center 1 alone.

The fluorescence of Center i is given by $f_i = f_i^0 p_i(0) + f_i^1 p_i(1)$, where $f_i^0(f_i^1)$ is the fluorescence level detected when Center i is in the state $m_s = 0(m_s = 1)$ and $p_i(m_S)$ is the probability of Center i being in state m_S. For the experiments considered in Fig. 4.4b, the measured total level of fluorescence during the readout is $f = f_1 + f_2$. For the experimental sequences S3 and S4,

$$f^{S3} = f_1^0 p_1^{S3}(0) + f_1^1 p_1^{S3}(1) + f_2^0 p_2^{S3}(0) + f_2^1 p_2^{S3}(1) \tag{C.30}$$

$$f^{S4} = f_1^0 p_1^{S4}(0) + f_1^1 p_1^{S4}(1) + f_2^0 p_2^{S4}(0) + f_2^1 p_2^{S4}(1), \tag{C.31}$$

where $p_i^{Sn}(m_S)$ is the probability that Center i is in state m_S after experiment Sn (prior to readout). In experiment S4, the effect of the second doughnnut pulse is to polarize completely the state of Center 2. As a result, $p_2^{S4}(0) = 1$ and $p_2^{S4}(1) = 0$. In addition,

an imperfect doughnut has the undesired effect of partially repolarizing Center 1. This partial repolarization is quantified by a parameter α; so that the probabilities $p_1^{S4}(m_S)$ can be expressed in terms of $p_1^{S3}(m_S)$ (the probabilities resulting from sub-wavelength coherent manipulation experiments) as follows,

$$p_1^{S4}(0) = p_1^{S3}(0) + (1-\alpha)p_1^{S3}(1) \qquad p_1^{S4}(1) = \alpha p_1^{S3}(1). \tag{C.32}$$

Equations (eq. C.30) and (eq. C.31) are then reduced to

$$f^{S3} = (f_1^0 - f_1^1)p_1^{S3}(0) + (f_2^0 - f_2^1)p_2^{S3}(0) \tag{C.33}$$

$$f^{S4} = f_1^0 p_1^{S3}(0) + (1-\alpha)f_1^0 p_1^{S3}(0) + \alpha f_1^1 p_1^{S3}(1) + f_2^0. \tag{C.34}$$

From this set of equations, we extract $p_1^{S3}(0)$ and $p_2^{S3}(0)$ as follows,

$$p_1^{S3}(0) = \frac{f^{S4} - f_1^0(1-\alpha) - \alpha f_1^1 - f_2^0}{\alpha(f_1^0 - f_1^1)} \tag{C.35}$$

$$p_2^{S3}(0) = 1 + \frac{\alpha f_T^{S3} - f_T^{S4}}{\alpha(f_2^0 - f_2^1)} + \frac{(1-\alpha)(f_2^0 + f_1^0)}{\alpha(f_2^0 - f_2^1)}, \tag{C.36}$$

which are plotted in Fig. 4.4b.

In order to evaluate the fluorescence parameters $f_i^{m_S}$ and the parameter α, we performed an auxiliary experiment where the repolarization rates of each center due to the doughnut beam were determined. In this experiment, the doughnut beam was centered at Center 1 and both NV centers were prepared in the $m_S = 1$ state by applying a resonant π pulse, followed by repolarization with a doughnut pulse of variable duration τ and subsequent fluorescent spin dependent state detection using a Gaussian excitation beam (see Figure C.9).

The fluorescence rate f in this experiment is again proportional to the projections $p_{1,2}(0)$ onto the $m_S = 0$ state of both NV centers,

$$f = f_1^0 p_1(0) + f_1^1 p_1(1) + f_2^0 p_2(0) + f_2^1 p_2(1). \tag{C.37}$$

The projection onto the $m_S = 0$ state can be written as $p_i(0) = 1 - \epsilon e^{-R_i \tau}$, where R_i is the rate of repolarization of Center i, τ the duration of the doughnut pulse and ϵ account for the imperfections of the initial π pulse. The probability for Center 1 in sequence S3 is modeled by $p_1^{S3}(0) = \frac{1}{2}\left(1 + e^{-\lambda_1 \tau} \cos \Omega_1 \tau\right)$, where Ω_1 is the Rabi frequency and λ_1 is a parameter that describes the effect of T_2^*. By using the least squares fitting of the fluorescence measurements of experiments S3, S4, and the auxiliary experiments to equations (eq. C.33), (eq. C.34) and (eq. C.37), we obtain the following parameters: $f_1^0 = f_T^0 - f_2^0 = 0.0057(\pm 0.00002)$, $f_1^1 = f_T^1 - f_2^1 = 0.0044(\pm 0.00001)$, and $\alpha = 0.743(\pm 0.018)$, where $f_T^0 = 0.0088(\pm 0.00003)$ and $f_T^1 = 0.0064(\pm 0.00002)$ are the total level of fluorescence when the centers are in their electronic spin $m_S = 0$ and $m_S = 1$, respectively.

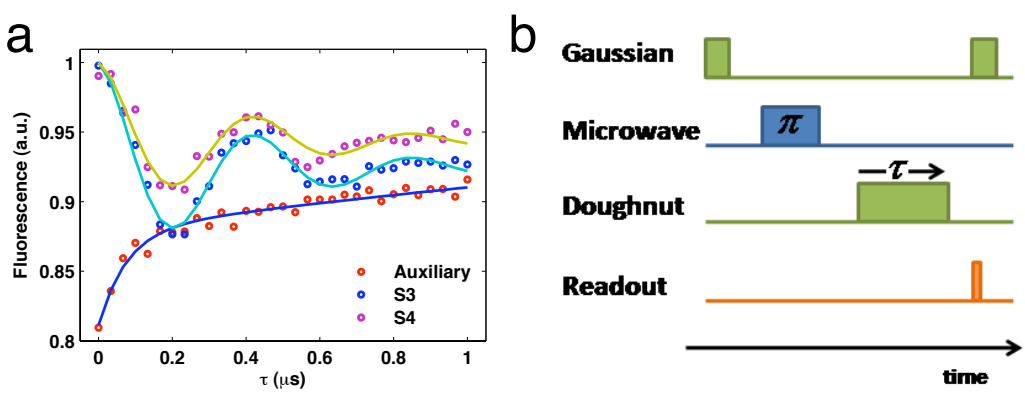

Figure C.9: | **(a) Measured fluorescence signal** for the experimental sequences S3, S4 and auxiliary as a function of the doughnut duration. Solid lines represent fittings using Equations (eq. C.33), (eq. C.34) and (eq. C.37), respectively. (b) Schematic pulse sequence used to record the data for the auxiliary experiment.

Bibliography

[1] T. D. Ladd, F. Jelezko, R. Laflamme, Y. Nakamura, C. Monroe, and J. L. OBrien. Quantum computers. *Nature*, 464(7285):45–53, 2010.

[2] Nobel prize in physics, 2012.

[3] N. F. Ramsey. A molecular beam resonance method with separated oscillating fields. *Phys. Rev.*, 78:695–699, Jun 1950.

[4] D. Sullivan. Time and frequency measurement at nist: The first 100 years. In *Frequency Control Symposium and PDA Exhibition, 2001. Proceedings of the 2001 IEEE International*, pages 4–17. IEEE, 2001.

[5] B. Bloom, T. Nicholson, J. Williams, S. Campbell, M. Bishof, X. Zhang, W. Zhang, S. Bromley, and J. Ye. An optical lattice clock with accuracy and stability at the 10-18 level. *Nature*, 2014.

[6] M. H. Schleier-Smith, I. LEROUX, and V. Vuletic. Spin squeezing on an atomic-clock transition. In *Pushing the Frontiers of Atomic Physics-Proceedings of the Xxi International Conference on Atomic Physics*, page 107. World Scientific, 2009.

[7] D. Budker and M. Romalis. Optical magnetometry. *Nature Physics*, 3(4):227–234, 2007.

[8] J. Cai, F. Jelezko, M. B. Plenio, and A. Retzker. Diamond-based single-molecule magnetic resonance spectroscopy. *New Journal of Physics*, 15(1):013020, 2013.

[9] L. Hall, G. Beart, E. Thomas, D. Simpson, L. McGuinness, J. Cole, J. Manton, R. Scholten, F. Jelezko, J. Wrachtrup, et al. High spatial and temporal resolution wide-field imaging of neuron activity using quantum nv-diamond. *Scientific reports*, 2, 2012.

[10] M. Georgescu, I. S. Ashhab, and F. Nori. Quantum simulation. *Rev. Mod. Phys.*, 86:153–185, Mar 2014.

[11] J. Simon, W. S. Bakr, R. Ma, M. E. Tai, P. M. Preiss, and M. Greiner. Quantum simulation of antiferromagnetic spin chains in an optical lattice. *Nature*, 472(7343):307–312, 2011.

[12] R. Islam, C. Senko, W. Campbell, S. Korenblit, J. Smith, A. Lee, E. Edwards, C.-C. Wang, J. Freericks, and C. Monroe. Emergence and frustration of magnetism with variable-range interactions in a quantum simulator. *Science*, 340(6132):583–587, 2013.

[13] P. W. Shor. Polynomial-time algorithms for prime factorization and discrete logarithms on a quantum computer. *SIAM journal on computing*, 26(5):1484–1509, 1997.

[14] D. P. DiVincenzo et al. The physical implementation of quantum computation. *arXiv preprint quant-ph/0002077*, 2000.

[15] L. DiCarlo, J. Chow, J. Gambetta, L. S. Bishop, B. Johnson, D. Schuster, J. Majer, A. Blais, L. Frunzio, S. Girvin, et al. Demonstration of two-qubit algorithms with a superconducting quantum processor. *Nature*, 460(7252):240–244, 2009.

[16] S. Gulde, M. Riebe, G. P. Lancaster, C. Becher, J. Eschner, H. Häffner, F. Schmidt-Kaler, I. L. Chuang, and R. Blatt. Implementation of the deutsch–jozsa algorithm on an ion-trap quantum computer. *Nature*, 421(6918):48–50, 2003.

[17] N. Gisin, G. Ribordy, W. Tittel, and H. Zbinden. Quantum cryptography. *Rev. Mod. Phys.*, 74:145–195, Mar 2002.

[18] N. Sangouard, C. Simon, H. de Riedmatten, and N. Gisin. Quantum repeaters based on atomic ensembles and linear optics. *Rev. Mod. Phys.*, 83:33–80, Mar 2011.

[19] C. Langer, R. Ozeri, J. D. Jost, J. Chiaverini, B. DeMarco, A. Ben-Kish, R. B. Blakestad, J. Britton, D. B. Hume, W. M. Itano, D. Leibfried, R. Reichle, T. Rosenband, T. Schaetz, P. O. Schmidt, and D. J. Wineland. Long-lived qubit memory using atomic ions. *Phys. Rev. Lett.*, 95:060502, Aug 2005.

[20] W. C. Campbell, J. Mizrahi, Q. Quraishi, C. Senko, D. Hayes, D. Hucul, D. N. Matsukevich, P. Maunz, and C. Monroe. Ultrafast gates for single atomic qubits. *Phys. Rev. Lett.*, 105:090502, Aug 2010.

[21] A. Sørensen and K. Mølmer. Quantum computation with ions in thermal motion. *Phys. Rev. Lett.*, 82:1971–1974, Mar 1999.

[22] D. Leibfried, B. DeMarco, V. Meyer, D. Lucas, M. Barrett, J. Britton, W. Itano, B. Jelenković, C. Langer, T. Rosenband, et al. Experimental demonstration of a robust, high-fidelity geometric two ion-qubit phase gate. *Nature*, 422(6930):412–415, 2003.

[23] A. H. Myerson, D. J. Szwer, S. C. Webster, D. T. C. Allcock, M. J. Curtis, G. Imreh, J. A. Sherman, D. N. Stacey, A. M. Steane, and D. M. Lucas. High-fidelity readout of trapped-ion qubits. *Phys. Rev. Lett.*, 100:200502, May 2008.

[24] C. Monroe and J. Kim. Scaling the ion trap quantum processor. *Science*, 339(6124):1164–1169, 2013.

[25] D. Kielpinski, C. Monroe, and D. J. Wineland. Architecture for a large-scale ion-trap quantum computer. *Nature*, 417(6890):709–711, 2002.

[26] D. Moehring, P. Maunz, S. Olmschenk, K. Younge, D. Matsukevich, L.-M. Duan, and C. Monroe. Entanglement of single-atom quantum bits at a distance. *Nature*, 449(7158):68–71, 2007.

[27] D. Loss and D. P. DiVincenzo. Quantum computation with quantum dots. *Physical Review A*, 57(1):120, 1998.

[28] R. Hanson and D. D. Awschalom. Coherent manipulation of single spins in semiconductors. *Nature*, 453(7198):1043–1049, 2008.

[29] M. H. Devoret, A. Wallraff, and J. Martinis. Superconducting qubits: A short review. *arXiv preprint cond-mat/0411174*, 2004.

[30] A. Morello, J. J. Pla, F. A. Zwanenburg, K. W. Chan, K. Y. Tan, H. Huebl, M. Möttönen, C. D. Nugroho, C. Yang, J. A. van Donkelaar, et al. Single-shot readout of an electron spin in silicon. *Nature*, 467(7316):687–691, 2010.

[31] M. Steger, K. Saeedi, M. Thewalt, J. Morton, H. Riemann, N. Abrosimov, P. Becker, and H.-J. Pohl. Quantum information storage for over 180 s using donor spins in a 28si semiconductor vacuum. *Science*, 336(6086):1280–1283, 2012.

[32] J. T. Muhonen, J. P. Dehollain, A. Laucht, F. E. Hudson, T. Sekiguchi, K. M. Itoh, D. N. Jamieson, J. C. McCallum, A. S. Dzurak, and A. Morello. Storing quantum information for 30 seconds in a nanoelectronic device. *arXiv preprint arXiv:1402.7140*, 2014.

[33] B. E. Kane. A silicon-based nuclear spin quantum computer. *nature*, 393(6681):133–137, 1998.

[34] M. Fuechsle, J. A. Miwa, S. Mahapatra, H. Ryu, S. Lee, O. Warschkow, L. C. Hollenberg, G. Klimeck, and M. Y. Simmons. A single-atom transistor. *Nature Nanotechnology*, 7(4):242–246, 2012.

[35] Y. Chu, N. de Leon, B. Shields, B. J. Hausmann, R. Evans, E. Togan, M. J. Burek, M. Markham, A. Stacey, A. Zibrov, et al. Coherent optical transitions in implanted nitrogen vacancy centers. *Nano letters*, 2014.

[36] D. M. Toyli, C. D. Weis, G. D. Fuchs, T. Schenkel, and D. D. Awschalom. Chip-scale nanofabrication of single spins and spin arrays in diamond. *Nano letters*, 10(8):3168–3172, 2010.

[37] J. Meijer, S. Pezzagna, T. Vogel, B. Burchard, H. Bukow, I. Rangelow, Y. Sarov, H. Wiggers, I. Plümel, F. Jelezko, et al. Towards the implanting of ions and positioning of nanoparticles with nm spatial resolution. *Applied Physics A*, 91(4):567–571, 2008.

[38] J. Meijer, T. Vogel, B. Burchard, I. Rangelow, L. Bischoff, J. Wrachtrup, M. Domhan, F. Jelezko, W. Schnitzler, S. Schulz, et al. Concept of deterministic single ion doping with sub-nm spatial resolution. *Applied Physics A*, 83(2):321–327, 2006.

[39] K. Ohno, F. J. Heremans, L. C. Bassett, B. A. Myers, D. M. Toyli, A. C. B. Jayich, C. J. Palmstrøm, and D. D. Awschalom. Engineering shallow spins in diamond with nitrogen delta-doping. *Applied Physics Letters*, 101(8):082413, 2012.

[40] A. Gali, M. Fyta, and E. Kaxiras. Ab initio supercell calculations on nitrogen-vacancy center in diamond: Electronic structure and hyperfine tensors. *Phys. Rev. B*, 77:155206, Apr 2008.

[41] G. Waldherr, J. Beck, M. Steiner, P. Neumann, A. Gali, T. Frauenheim, F. Jelezko, and J. Wrachtrup. Dark states of single nitrogen-vacancy centers in diamond unraveled by single shot nmr. *Phys. Rev. Lett.*, 106:157601, Apr 2011.

[42] D. Toyli, D. Christle, A. Alkauskas, B. Buckley, C. Van de Walle, and D. Awschalom. Measurement and control of single nitrogen-vacancy center spins above 600 k. *Physical Review X*, 2(3):031001, 2012.

[43] G. Fuchs, V. Dobrovitski, D. Toyli, F. Heremans, and D. Awschalom. Gigahertz dynamics of a strongly driven single quantum spin. *Science*, 326(5959):1520–1522, 2009.

[44] L. Childress, M. G. Dutt, J. Taylor, A. Zibrov, F. Jelezko, J. Wrachtrup, P. Hemmer, and M. Lukin. Coherent dynamics of coupled electron and nuclear spin qubits in diamond. *Science*, 314(5797):281–285, 2006.

[45] N. Bar-Gill, L. M. Pham, A. Jarmola, D. Budker, and R. L. Walsworth. Solid-state electronic spin coherence time approaching one second. *Nature communications*, 4:1743, 2013.

[46] F. Dolde, V. Bergholm, Y. Wang, I. Jakobi, B. Naydenov, S. Pezzagna, J. Meijer, F. Jelezko, P. Neumann, T. Schulte-Herbruggen, J. Biamonte, and J. Wrachtrup. High-fidelity spin entanglement using optimal control. *Nature Communications*, 5(3371):1–9, 2014.

[47] E. Togan, Y. Chu, A. Trifonov, L. Jiang, J. Maze, L. Childress, M. G. Dutt, A. S. Sørensen, P. Hemmer, A. Zibrov, et al. Quantum entanglement between an optical photon and a solid-state spin qubit. *Nature*, 466(7307):730–734, 2010.

[48] H. Bernien, B. Hensen, W. Pfaff, G. Koolstra, M. Blok, L. Robledo, T. Taminiau, M. Markham, D. Twitchen, L. Childress, et al. Heralded entanglement between solid-state qubits separated by three metres. *Nature*, 497(7447):86–90, 2013.

[49] H. Kimble. The quantum internet. *Nature*, 453(7198):1023–1030, 2008.

[50] L. Childress, M. Lukin, A. Sørensen, and J. Taylor. Fault-tolerant quantum communication based on solid-state photon emitters. Technical report, 2004.

[51] L. Childress, A. Sørensen, and M. Lukin. Mesoscopic cavity quantum electrodynamics with quantum dots. *Physical Review A*, 69(4):042302, 2004.

[52] J. Taylor, P. Cappellaro, L. Childress, L. Jiang, D. Budker, P. Hemmer, A. Yacoby, R. Walsworth, and M. Lukin. High-sensitivity diamond magnetometer with nanoscale resolution. *Nature Physics*, 4(10):810–816, 2008.

[53] P. Maletinsky, S. Hong, M. S. Grinolds, B. Hausmann, M. D. Lukin, R. L. Walsworth, M. Loncar, and A. Yacoby. A robust scanning diamond sensor for nanoscale imaging with single nitrogen-vacancy centres. *Nature nanotechnology*, 7(5):320–324, 2012.

[54] M. Grinolds, S. Hong, P. Maletinsky, L. Luan, M. Lukin, R. Walsworth, and A. Yacoby. Nanoscale magnetic imaging of a single electron spin under ambient conditions. *Nature Physics*, 9(4):215–219, 2013.

[55] M. S. Grinolds, M. Warner, K. De Greve, Y. Dovzhenko, L. Thiel, R. L. Walsworth, S. Hong, P. Maletinsky, and A. Yacoby. Subnanometre resolution in three-dimensional magnetic resonance imaging of individual dark spins. *Nature Nanotechnology*, 2014.

[56] A. Sushkov, N. Chisholm, I. Lovchinsky, M. Kubo, P. Lo, S. Bennett, D. Hunger, A. Akimov, R. Walsworth, H. Park, et al. All-optical sensing of a single-molecule electron spin. *arXiv preprint arXiv:1311.1801*, 2013.

[57] H. Mamin, M. Kim, M. Sherwood, C. Rettner, K. Ohno, D. Awschalom, and D. Rugar. Nanoscale nuclear magnetic resonance with a nitrogen-vacancy spin sensor. *Science*, 339(6119):557–560, 2013.

[58] T. Staudacher, F. Shi, S. Pezzagna, J. Meijer, J. Du, C. Meriles, F. Reinhard, and J. Wrachtrup. Nuclear magnetic resonance spectroscopy on a (5-nanometer) 3 sample volume. *Science*, 339(6119):561–563, 2013.

[59] L.-M. Duan and C. Monroe. Quantum networks with trapped ions. *Rev. Mod. Phys.*, 82:1209–1224, Apr 2010.

[60] T. D. Ladd, D. Maryenko, Y. Yamamoto, E. Abe, and K. M. Itoh. Coherence time of decoupled nuclear spins in silicon. *Phys. Rev. B*, 71:014401, Jan 2005.

[61] M. V. Balabas, T. Karaulanov, M. P. Ledbetter, and D. Budker. Polarized alkali-metal vapor with minute-long transverse spin-relaxation time. *Phys. Rev. Lett.*, 105:070801, Aug 2010.

[62] A. M. Tyryshkin, S. Tojo, J. J. Morton, H. Riemann, N. V. Abrosimov, P. Becker, H.-J. Pohl, T. Schenkel, M. L. Thewalt, K. M. Itoh, et al. Electron spin coherence exceeding seconds in high-purity silicon. *Nature materials*, 11(2):143–147, 2012.

[63] M. G. Dutt, L. Childress, L. Jiang, E. Togan, J. Maze, F. Jelezko, A. Zibrov, P. Hemmer, and M. Lukin. Quantum register based on individual electronic and nuclear spin qubits in diamond. *Science*, 316(5829):1312–1316, 2007.

[64] T. Van der Sar, Z. Wang, M. Blok, H. Bernien, T. Taminiau, D. Toyli, D. Lidar, D. Awschalom, R. Hanson, and V. Dobrovitski. Decoherence-protected quantum gates for a hybrid solid-state spin register. *Nature*, 484(7392):82–86, 2012.

[65] P. Neumann, J. Beck, M. Steiner, F. Rempp, H. Fedder, P. R. Hemmer, J. Wrachtrup, and F. Jelezko. Single-shot readout of a single nuclear spin. *Science*, 329(5991):542–544, 2010.

[66] L. Jiang, J. Hodges, J. Maze, P. Maurer, J. Taylor, D. Cory, P. Hemmer, R. Walsworth, A. Yacoby, A. Zibrov, et al. Repetitive readout of a single electronic spin via quantum logic with nuclear spin ancillae. *Science*, 326(5950):267–272, 2009.

[67] L. Jiang, M. V. G. Dutt, E. Togan, L. Childress, P. Cappellaro, J. M. Taylor, and M. D. Lukin. Coherence of an optically illuminated single nuclear spin qubit. *Phys. Rev. Lett.*, 100:073001, Feb 2008.

[68] P. Neumann, N. Mizuochi, F. Rempp, P. Hemmer, H. Watanabe, S. Yamasaki, V. Jacques, T. Gaebel, F. Jelezko, and J. Wrachtrup. Multipartite entanglement among single spins in diamond. *science*, 320(5881):1326–1329, 2008.

[69] G. De Lange, Z. Wang, D. Riste, V. Dobrovitski, and R. Hanson. Universal dynamical decoupling of a single solid-state spin from a spin bath. *Science*, 330(6000):60–63, 2010.

[70] J. T. Barreiro, M. Müller, P. Schindler, D. Nigg, T. Monz, M. Chwalla, M. Hennrich, C. F. Roos, P. Zoller, and R. Blatt. An open-system quantum simulator with trapped ions. *Nature*, 470(7335):486–491, 2011.

[71] H. Krauter, C. A. Muschik, K. Jensen, W. Wasilewski, J. M. Petersen, J. I. Cirac, and E. S. Polzik. Entanglement generated by dissipation and steady state entanglement of two macroscopic objects. *Physical review letters*, 107(8):080503, 2011.

[72] G. Balasubramanian, P. Neumann, D. Twitchen, M. Markham, R. Kolesov, N. Mizuochi, J. Isoya, J. Achard, J. Beck, J. Tissler, et al. Ultralong spin coherence time in isotopically engineered diamond. *Nature materials*, 8(5):383–387, 2009.

[73] A. Burrell, D. Szwer, S. Webster, and D. Lucas. Scalable simultaneous multiqubit readout with 99. 99% single-shot fidelity. *Physical Review A*, 81(4):040302, 2010.

[74] W. M. Itano, D. J. Heinzen, J. J. Bollinger, and D. J. Wineland. Quantum zeno effect. *Phys. Rev. A*, 41:2295–2300, Mar 1990.

[75] V. M. Acosta, E. Bauch, M. P. Ledbetter, A. Waxman, L.-S. Bouchard, and D. Budker. Temperature dependence of the nitrogen-vacancy magnetic resonance in diamond. *Phys. Rev. Lett.*, 104:070801, Feb 2010.

[76] N. Khaneja, R. Brockett, and S. J. Glaser. Time optimal control in spin systems. *Phys. Rev. A*, 63:032308, Feb 2001.

[77] C. J. Terblanche, E. C. Reynhardt, and J. A. van Wyk. C13 spin–lattice relaxation in natural diamond: Zeeman relaxation at 4.7 t and 300 k due to fixed paramagnetic nitrogen defects. *Solid state nuclear magnetic resonance*, 20(1):1–22, 2001.

[78] S. Wiesner. Conjugate coding. *ACM Sigact News*, 15(1):78–88, 1983.

[79] F. Pastawski, N. Y. Yao, L. Jiang, M. D. Lukin, and J. I. Cirac. Unforgeable noise-tolerant quantum tokens. *Proceedings of the National Academy of Sciences*, 109(40):16079–16082, 2012.

[80] P. Spinicelli, A. Dréau, L. Rondin, F. Silva, J. Achard, S. Xavier, S. Bansropun, T. Debuisschert, S. Pezzagna, J. Meijer, et al. Engineered arrays of nitrogen-vacancy color centers in diamond based on implantation of cn- molecules through nanoapertures. *New Journal of Physics*, 13(2):025014, 2011.

[81] P. Neumann, R. Kolesov, B. Naydenov, J. Beck, F. Rempp, M. Steiner, V. Jacques, G. Balasubramanian, M. Markham, D. Twitchen, et al. Quantum register based on coupled electron spins in a room-temperature solid. *Nature Physics*, 6(4):249–253, 2010.

[82] N. Y. Yao, L. Jiang, A. V. Gorshkov, P. C. Maurer, G. Giedke, J. I. Cirac, and M. D. Lukin. Scalable architecture for a room temperature solid-state quantum information processor. *Nature communications*, 3:800, 2012.

[83] Y. Yue and X. Wang. Nanoscale thermal probing. *Nano reviews*, 3, 2012.

[84] E. Lucchetta, J. Lee, L. Fu, N. Patel, and R. Ismagilov. Dynamics of drosophila embryonic patterning network perturbed in space and time using microfluidics. *Nature*, 434(7037):1134–1138, 2005.

[85] S. V. Kumar and P. A. Wigge. H2a. z-containing nucleosomes mediate the thermosensory response in arabidopsis. *Cell*, 140(1):136–147, 2010.

[86] V. M. Lauschke, C. D. Tsiairis, P. François, and A. Aulehla. Scaling of embryonic patterning based on phase-gradient encoding. *Nature*, 493(7430):101–105, 2012.

[87] Y. Kamei, M. Suzuki, K. Watanabe, K. Fujimori, T. Kawasaki, T. Deguchi, Y. Yoneda, T. Todo, S. Takagi, T. Funatsu, et al. Infrared laser–mediated gene induction in targeted single cells in vivo. *Nature methods*, 6(1):79–81, 2008.

[88] T. Vreugdenburg, C. Willis, L. Mundy, and J. Hiller. A systematic review of elastography, electrical impedance scanning, and digital infrared thermography for breast cancer screening and diagnosis. *Breast Cancer Research and Treatment*, 137:665–676, 2013.

[89] A. Schroeder, D. A. Heller, M. M. Winslow, J. E. Dahlman, G. W. Pratt, R. Langer, T. Jacks, and D. G. Anderson. Treating metastatic cancer with nanotechnology. *Nature Reviews Cancer*, 12(1):39–50, 2011.

[90] D. P. O'Neal, L. R. Hirsch, N. J. Halas, J. D. Payne, and J. L. West. Photo-thermal tumor ablation in mice using near infrared-absorbing nanoparticles. *Cancer letters*, 209(2):171–176, 2004.

[91] A. Majumdar. Scanning thermal microscopy. *Annual review of materials science*, 29(1):505–585, 1999.

[92] S. H. Kim, J. Noh, M. K. Jeon, K. W. Kim, L. P. Lee, and S. I. Woo. Micro-raman thermometry for measuring the temperature distribution inside the microchannel of a polymerase chain reaction chip. *Journal of Micromechanics and Microengineering*, 16(3):526, 2006.

[93] J. Yang, H. Yang, and L. Lin. Quantum dot nano thermometers reveal heterogeneous local thermogenesis in living cells. *ACS nano*, 5(6):5067–5071, 2011.

[94] F. Vetrone, R. Naccache, A. Zamarrn, A. Juarranz de la Fuente, F. Sanz-Rodrguez, L. Martinez Maestro, E. Martn Rodriguez, D. Jaque, J. Garca Sol, and J. A. Capobianco. Temperature sensing using fluorescent nanothermometers. *ACS nano*, 4(6):3254–3258, 2010.

[95] K. Okabe, N. Inada, C. Gota, Y. Harada, T. Funatsu, and S. Uchiyama. Intracellular temperature mapping with a fluorescent polymeric thermometer and fluorescence lifetime imaging microscopy. *Nature communications*, 3:705, 2012.

[96] J. Donner, S. Thompson, M. Kreuzer, G. Baffou, and R. Quidant. Mapping intracellular temperature using green fluorescent protein. *Nano letters*, 12(4):2107–2111, 2012.

[97] A. K. Shalek, J. T. Robinson, E. S. Karp, J. S. Lee, D.-R. Ahn, M.-H. Yoon, A. Sutton, M. Jorgolli, R. S. Gertner, T. S. Gujral, et al. Vertical silicon nanowires as a universal platform for delivering biomolecules into living cells. *Proceedings of the National Academy of Sciences*, 107(5):1870–1875, 2010.

[98] X.-D. Chen, C.-H. Dong, F.-W. Sun, C.-L. Zou, J.-M. Cui, Z.-F. Han, and G.-C. Guo. Temperature dependent energy level shifts of nitrogen-vacancy centers in diamond. *Applied Physics Letters*, 99(16):161903–161903, 2011.

[99] C. Jin, Z. Li, R. Williams, K. Lee, and I. Park. Localized temperature and chemical reaction control in nanoscale space by nanowire array. *Nano letters*, 11(11):4818–4825, 2011.

[100] J. Maze, P. Stanwix, J. Hodges, S. Hong, J. Taylor, P. Cappellaro, L. Jiang, M. G. Dutt, E. Togan, A. Zibrov, et al. Nanoscale magnetic sensing with an individual electronic spin in diamond. *Nature*, 455(7213):644–647, 2008.

[101] G. Balasubramanian, I. Chan, R. Kolesov, M. Al-Hmoud, J. Tisler, C. Shin, C. Kim, A. Wojcik, P. R. Hemmer, A. Krueger, et al. Nanoscale imaging magnetometry with diamond spins under ambient conditions. *Nature*, 455(7213):648–651, 2008.

[102] J. Hodges and D. Englund. Time-keeping with electron spin states in diamond. *arXiv preprint arXiv:1109.3241*, 2011.

[103] F. Dolde, H. Fedder, M. Doherty, T. Nöbauer, F. Rempp, G. Balasubramanian, T. Wolf, F. Reinhard, L. Hollenberg, F. Jelezko, et al. Electric-field sensing using single diamond spins. *Nature Physics*, 7(6):459–463, 2011.

[104] P. Cappellaro and M. D. Lukin. Quantum correlation in disordered spin systems: Applications to magnetic sensing. *Physical Review A*, 80(3):032311, 2009.

[105] P. Maurer, J. Maze, P. Stanwix, L. Jiang, A. Gorshkov, A. A. Zibrov, B. Harke, J. Hodges, A. S. Zibrov, A. Yacoby, et al. Far-field optical imaging and manipulation of individual spins with nanoscale resolution. *Nature Physics*, 6(11):912–918, 2010.

[106] G. Xu, S. M. Stevens, F. Kobiessy, H. Brown, S. McClung, M. S. Gold, and D. R. Borchelt. Identification of proteins sensitive to thermal stress in human neuroblastoma and glioma cell lines. *PloS one*, 7(11):e49021, 2012.

[107] F. Helmchen and W. Denk. Deep tissue two-photon microscopy. *Nature methods*, 2(12):932–940, 2005.

[108] T.-L. Wee, Y.-K. Tzeng, C.-C. Han, H.-C. Chang, W. Fann, J.-H. Hsu, K.-M. Chen, and Y.-C. Yu. Two-photon excited fluorescence of nitrogen-vacancy centers in proton-irradiated type ib diamond. *The Journal of Physical Chemistry A*, 111(38):9379–9386, 2007.

[109] M. Tsoli, M. Moore, D. Burg, A. Painter, R. Taylor, S. H. Lockie, N. Turner, A. Warren, G. Cooney, B. Oldfield, et al. Activation of thermogenesis in brown adipose tissue and dysregulated lipid metabolism associated with cancer cachexia in mice. *Cancer Research*, 72(17):4372–4382, 2012.

[110] S. T. Cundiff and J. Ye. Femtosecond optical frequency combs. *Rev. Mod. Phys.*, 75:325–342, Mar 2003.

[111] X. Xu, B. Sun, P. R. Berman, D. G. Steel, A. S. Bracker, D. Gammon, and L. J. Sham. Coherent optical spectroscopy of a strongly driven quantum dot. *Science*, 317(5840):929–932, 2007.

[112] K. Hennessy, A. Badolato, M. Winger, D. Gerace, M. Atatüre, S. Gulde, S. Fält, E. L. Hu, and A. Imamoğlu. Quantum nature of a strongly coupled single quantum dot–cavity system. *Nature*, 445(7130):896–899, 2007.

[113] C. Degen. Scanning magnetic field microscope with a diamond single-spin sensor. *Applied Physics Letters*, 92(24):243111, 2008.

[114] V. Westphal and S. W. Hell. Nanoscale resolution in the focal plane of an optical microscope. *Physical review letters*, 94(14):143903, 2005.

[115] X. Zhuang. Nano-imaging with storm. *Nature photonics*, 3(7):365, 2009.

[116] E. Betzig, G. H. Patterson, R. Sougrat, O. W. Lindwasser, S. Olenych, J. S. Bonifacino, M. W. Davidson, J. Lippincott-Schwartz, and H. F. Hess. Imaging intracellular fluorescent proteins at nanometer resolution. *Science*, 313(5793):1642–1645, 2006.

[117] L. Li, R. R. Gattass, E. Gershgoren, H. Hwang, and J. T. Fourkas. Achieving $\lambda/20$ resolution by one-color initiation and deactivation of polymerization. *Science*, 324(5929):910–913, 2009.

[118] T. F. Scott, B. A. Kowalski, A. C. Sullivan, C. N. Bowman, and R. R. McLeod. Two-color single-photon photoinitiation and photoinhibition for subdiffraction photolithography. *Science*, 324(5929):913–917, 2009.

[119] K. Johnson, J. Thywissen, N. Dekker, K. Berggren, A. Chu, R. Younkin, and M. Prentiss. Localization of metastable atom beams with optical standing waves: nanolithography at the heisenberg limit. *Science*, 280(5369):1583–1586, 1998.

[120] S. W. Hell and J. Wichmann. Breaking the diffraction resolution limit by stimulated emission: stimulated-emission-depletion fluorescence microscopy. *Optics letters*, 19(11):780–782, 1994.

[121] S. W. Hell. Far-field optical nanoscopy. In *Single Molecule Spectroscopy in Chemistry, Physics and Biology*, pages 365–398. Springer, 2010.

[122] E. Rittweger, K. Y. Han, S. E. Irvine, C. Eggeling, and S. W. Hell. Sted microscopy reveals crystal colour centres with nanometric resolution. *Nature Photonics*, 3(3):144–147, 2009.

[123] R. Hanson, V. Dobrovitski, A. Feiguin, O. Gywat, and D. Awschalom. Coherent dynamics of a single spin interacting with an adjustable spin bath. *Science*, 320(5874):352–355, 2008.

[124] J. Wrachtrup and F. Jelezko. Processing quantum information in diamond. *Journal of Physics: Condensed Matter*, 18(21):S807, 2006.

[125] J. Maze, J. Taylor, and M. Lukin. Electron spin decoherence of single nitrogen-vacancy defects in diamond. *Physical Review B*, 78(9):094303, 2008.

[126] N. B. Manson, J. P. Harrison, and M. J. Sellars. Nitrogen-vacancy center in diamond: Model of the electronic structure and associated dynamics. *Phys. Rev. B*, 74:104303, Sep 2006.

[127] A. V. Gorshkov, L. Jiang, M. Greiner, P. Zoller, and M. D. Lukin. Coherent quantum optical control with subwavelength resolution. *Phys. Rev. Lett.*, 100:093005, Mar 2008.

[128] A. G. Fowler, M. Mariantoni, J. M. Martinis, and A. N. Cleland. Surface codes: Towards practical large-scale quantum computation. *Phys. Rev. A*, 86:032324, Sep 2012.

[129] W. A. Brennan, E. D. Bird, and J. R. Aprille. Regional mitochondrial respiratory activity in huntington's disease brain. *Journal of neurochemistry*, 44(6):1948–1950, 1985.

[130] A. Navarro and A. Boveris. Rat brain and liver mitochondria develop oxidative stress and lose enzymatic activities on aging. *American Journal of Physiology-Regulatory, Integrative and Comparative Physiology*, 287(5):R1244–R1249, 2004.

[131] K. F. O'Connell, C. M. Leys, and J. G. White. A genetic screen for temperature-sensitive cell-division mutants of caenorhabditis elegans. *Genetics*, 149(3):1303–1321, 1998.

[132] R. Blatt and D. Wineland. Entangled states of trapped atomic ions. *Nature*, 453(7198):1008–1015, 2008.

[133] M. Riebe, H. Häffner, C. Roos, W. Hänsel, J. Benhelm, G. Lancaster, T. Körber, C. Becher, F. Schmidt-Kaler, D. James, et al. Deterministic quantum teleportation with atoms. *Nature*, 429(6993):734–737, 2004.

[134] R. Reichle, D. Leibfried, E. Knill, J. Britton, R. Blakestad, J. Jost, C. Langer, R. Ozeri, S. Seidelin, and D. Wineland. Experimental purification of two-atom entanglement. *Nature*, 443(7113):838–841, 2006.

[135] C. A. Ryan, C. Negrevergne, M. Laforest, E. Knill, and R. Laflamme. Liquid-state nuclear magnetic resonance as a testbed for developing quantum control methods. *Phys. Rev. A*, 78:012328, Jul 2008.

[136] T. Rosenband, D. Hume, P. Schmidt, C. Chou, A. Brusch, L. Lorini, W. Oskay, R. Drullinger, T. Fortier, J. Stalnaker, et al. Frequency ratio of al+ and hg+ single-ion optical clocks; metrology at the 17th decimal place. *Science*, 319(5871):1808–1812, 2008.

[137] D. B. Hume, T. Rosenband, and D. J. Wineland. High-fidelity adaptive qubit detection through repetitive quantum nondemolition measurements. *Phys. Rev. Lett.*, 99:120502, Sep 2007.

[138] W. M. Witzel and S. Das Sarma. Wavefunction considerations for the central spin decoherence problem in a nuclear spin bath. *Phys. Rev. B*, 77:165319, Apr 2008.

[139] J. R. Maze, J. M. Taylor, and M. D. Lukin. Electron spin decoherence of single nitrogen-vacancy defects in diamond. *Phys. Rev. B*, 78:094303, Sep 2008.

[140] W. A. Coish, J. Fischer, and D. Loss. Exponential decay in a spin bath. *Phys. Rev. B*, 77:125329, Mar 2008.

[141] F. Jelezko, T. Gaebel, I. Popa, M. Domhan, A. Gruber, and J. Wrachtrup. Observation of coherent oscillation of a single nuclear spin and realization of a two-qubit conditional quantum gate. *Phys. Rev. Lett.*, 93:130501, Sep 2004.

[142] J. J. Morton, A. M. Tyryshkin, A. Ardavan, S. C. Benjamin, K. Porfyrakis, S. Lyon, and G. A. D. Briggs. Bang–bang control of fullerene qubits using ultrafast phase gates. *Nature Physics*, 2(1):40–43, 2006.

[143] J. S. Hodges, J. C. Yang, C. Ramanathan, and D. G. Cory. Universal control of nuclear spins via anisotropic hyperfine interactions. *Phys. Rev. A*, 78:010303, Jul 2008.

[144] J. J. Morton, A. M. Tyryshkin, R. M. Brown, S. Shankar, B. W. Lovett, A. Ardavan, T. Schenkel, E. E. Haller, J. W. Ager, and S. Lyon. Solid-state quantum memory using the 31p nuclear spin. *Nature*, 455(7216):1085–1088, 2008.

[145] G. D. Fuchs, V. V. Dobrovitski, R. Hanson, A. Batra, C. D. Weis, T. Schenkel, and D. D. Awschalom. Excited-state spectroscopy using single spin manipulation in diamond. *Phys. Rev. Lett.*, 101:117601, Sep 2008.

[146] L. Jiang, J. M. Taylor, A. S. Sørensen, and M. D. Lukin. Distributed quantum computation based on small quantum registers. *Phys. Rev. A*, 76:062323, Dec 2007.

[147] S. Haroche and J.-M. Raimond. *Exploring the quantum: atoms, cavities, and photons (oxford graduate texts)*. Oxford University Press, USA, 2013.

[148] M. Sarovar, K. C. Young, T. Schenkel, and K. B. Whaley. Quantum nondemolition measurements of single donor spins in semiconductors. *Phys. Rev. B*, 78:245302, Dec 2008.

[149] T. Schulte-Herbrüggen, A. Spörl, K. Waldherr, T. Gradl, S. Glaser, and T. Huckle. The hlrb cluster as quantum cisc compiler. In *High Performance Computing in Science and Engineering, Garching/Munich 2007*, pages 517–533. Springer, 2009.

[150] P. Cappellaro, L. Jiang, J. Hodges, and M. Lukin. Coherence and control of quantum registers based on electronic spin in a nuclear spin bath. *Physical review letters*, 102(21):210502, 2009.

[151] A. Batalov, V. Jacques, F. Kaiser, P. Siyushev, P. Neumann, L. J. Rogers, R. L. McMurtrie, N. B. Manson, F. Jelezko, and J. Wrachtrup. Low temperature studies of the excited-state structure of negatively charged nitrogen-vacancy color centers in diamond. *Phys. Rev. Lett.*, 102:195506, May 2009.

[152] M. Stoneham. Is a room-temperature, solid-state quantum computer mere fantasy. *Physics*, 2:34, 2009.

[153] A. Stoneham, A. Fisher, and P. Greenland. Optically driven silicon-based quantum gates with potential for high-temperature operation. *Journal of Physics: Condensed Matter*, 15(27):L447, 2003.

[154] J. Hogan. Computing: Quantum bits and silicon chips. *Nature*, 424(6948):484–486, 2003.

[155] L.-M. Duan, B. Blinov, D. Moehring, and C. Monroe. Scalable trapped ion quantum computation with a probabilistic ion-photon mapping. *arXiv preprint quant-ph/0401020*, 2004.

[156] S. C. Benjamin, D. E. Browne, J. Fitzsimons, and J. J. Morton. Brokered graph-state quantum computation. *New Journal of Physics*, 8(8):141, 2006.

[157] Y. Makhlin, G. Schön, and A. Shnirman. Quantum-state engineering with josephson-junction devices. *Reviews of modern physics*, 73(2):357, 2001.

[158] R. Epstein, F. Mendoza, Y. Kato, and D. Awschalom. Anisotropic interactions of a single spin and dark-spin spectroscopy in diamond. *Nature physics*, 1(2):94–98, 2005.

[159] J. Weber, W. Koehl, J. Varley, A. Janotti, B. Buckley, C. Van de Walle, and D. D. Awschalom. Quantum computing with defects. *Proceedings of the National Academy of Sciences*, 107(19):8513–8518, 2010.

[160] G. Fuchs, V. Dobrovitski, D. Toyli, F. Heremans, C. Weis, T. Schenkel, and D. Awschalom. Excited-state spin coherence of a single nitrogen-vacancy centre in diamond. *Nature Physics*, 6(9):668–672, 2010.

[161] A. Bermudez, F. Jelezko, M. Plenio, and A. Retzker. Viewpoint: Driving a hard bargain with diamond qubits. *Phys. Rev. Lett*, 107:150503, 2011.

[162] A. M. Stoneham, A. H. Harker, and G. W. Morley. Could one make a diamond-based quantum computer? *Journal of Physics: Condensed Matter*, 21(36):364222, 2009.

[163] A. Tallaire, A. Collins, D. Charles, J. Achard, R. Sussmann, A. Gicquel, M. Newton, A. Edmonds, and R. Cruddace. Characterisation of high-quality thick single-crystal diamond grown by cvd with a low nitrogen addition. *Diamond and related materials*, 15(10):1700–1707, 2006.

[164] S. Bose. Quantum communication through an unmodulated spin chain. *Physical review letters*, 91(20):207901, 2003.

[165] E. Reynhardt, G. High, and J. Van Wyk. Temperature dependence of spin-spin and spin-lattice relaxation times of paramagnetic nitrogen defects in diamond. *The Journal of chemical physics*, 109(19):8471–8477, 1998.

[166] R. Raussendorf and J. Harrington. Fault-tolerant quantum computation with high threshold in two dimensions. *arXiv preprint quant-ph/0610082*, 2006.

[167] D. Wildanger, J. R. Maze, and S. W. Hell. Diffraction unlimited all-optical recording of electron spin resonances. *Physical review letters*, 107(1):017601, 2011.

[168] W. M. Itano, D. J. Heinzen, J. Bollinger, and D. Wineland. Quantum zeno effect. *Physical Review A*, 41(5):2295, 1990.

[169] G. Boero, M. Bouterfas, C. Massin, F. Vincent, P.-A. Besse, R. Popovic, and A. Schweiger. Electron-spin resonance probe based on a 100 μm planar microcoil. *Review of scientific instruments*, 74(11):4794–4798, 2003.

[170] A. V. Gorshkov, L. Jiang, M. Greiner, P. Zoller, and M. D. Lukin. Coherent quantum optical control with subwavelength resolution. *Physical review letters*, 100(9):093005, 2008.

[171] H. Lee, Y. Liu, D. Ham, and R. M. Westervelt. Integrated cell manipulation system-cmos/microfluidic hybrid. *Lab on a Chip*, 7(3):331–337, 2007.

[172] Q. Ramadan, D. P. Poenar, and C. Yu. Customized trapping of magnetic particles. *Microfluidics and nanofluidics*, 6(1):53–62, 2009.

[173] X. Yu, X. Feng, J. Hu, Z.-L. Zhang, and D.-W. Pang. Controlling the magnetic field distribution on the micrometer scale and generation of magnetic bead patterns for microfluidic applications. *Langmuir*, 27(8):5147–5156, 2011.

[174] L. Jiang, J. M. Taylor, A. S. Sørensen, and M. D. Lukin. Distributed quantum computation based on small quantum registers. *Physical Review A*, 76(6):062323, 2007.

[175] F. Evers and A. D. Mirlin. Anderson transitions. *Rev. Mod. Phys.*, 80:1355–1417, Oct 2008.

[176] L. Balents and M. P. Fisher. Delocalization transition via supersymmetry in one dimension. *Physical Review B*, 56(20):12970, 1997.

[177] P. Rabl, P. Cappellaro, M. G. Dutt, L. Jiang, J. Maze, and M. D. Lukin. Strong magnetic coupling between an electronic spin qubit and a mechanical resonator. *Physical Review B*, 79(4):041302, 2009.

[178] M. Suzuki. Generalized trotter's formula and systematic approximants of exponential operators and inner derivations with applications to many-body problems. *Communications in Mathematical Physics*, 51(2):183–190, 1976.

[179] S. Takahashi, R. Hanson, J. Van Tol, M. S. Sherwin, and D. D. Awschalom. Quenching spin decoherence in diamond through spin bath polarization. *Physical review letters*, 101(4):047601, 2008.

[180] J. H. N. Loubser and W. P. van Ryneveld. Dynamic jahn-teller and other effects in high-temperature electron spin resonance spectrum of nitrogen in diamond. *British J Appl Phys*, 18:1029–1031, 1967.

[181] C. Kedkaew, P. Limsuwan, K. Thongcham, and S. Meejoo. The spin hamiltonian parameters calculation of 14 n and 15 n in natural type i diamond. *International Journal of Modern Physics B*, 22(25n26):4740–4748, 2008.

[182] J. Roland and N. J. Cerf. Quantum search by local adiabatic evolution. *Physical Review A*, 65(4):042308, 2002.

[183] T. Caneva, M. Murphy, T. Calarco, R. Fazio, S. Montangero, V. Giovannetti, and G. E. Santoro. Optimal control at the quantum speed limit. *arXiv preprint arXiv:0902.4193*, 2009.

[184] A. Messiah. *Quantum mechanics*. Courier Dover Publications, 2014.

[185] A. Jarmola, V. Acosta, K. Jensen, S. Chemerisov, and D. Budker. Temperature-and magnetic-field-dependent longitudinal spin relaxation in nitrogen-vacancy ensembles in diamond. *Physical review letters*, 108(19):197601, 2012.

[186] D. Redman, S. Brown, R. Sands, and S. Rand. Spin dynamics and electronic states of n-v centers in diamond by epr and four-wave-mixing spectroscopy. *Physical review letters*, 67(24):3420, 1991.

[187] S. B. Bravyi and A. Y. Kitaev. Quantum codes on a lattice with boundary. *arXiv preprint quant-ph/9811052*, 1998.

[188] A. G. Fowler, A. M. Stephens, and P. Groszkowski. High-threshold universal quantum computation on the surface code. *Phys. Rev. A*, 80:052312, Nov 2009.

[189] D. S. Wang, A. G. Fowler, and L. C. Hollenberg. Surface code quantum computing with error rates over 1%. *Physical Review A*, 83(2):020302, 2011.

[190] A. Beyzavi and N.-T. Nguyen. Modeling and optimization of planar microcoils. *Journal of Micromechanics and Microengineering*, 18(9):095018, 2008.

[191] H. Lee, E. Sun, D. Ham, and R. Weissleder. Chip–nmr biosensor for detection and molecular analysis of cells. *Nature medicine*, 14(8):869–874, 2008.

[192] C. Knoernschild, X. L. Zhang, L. Isenhower, A. T. Gill, F. P. Lu, M. Saffman, and J. Kim. Independent individual addressing of multiple neutral atom qubits with a micromirror-based beam steering system. *Applied Physics Letters*, 97(13):134101–134101, 2010.

[193] H. Yuan, R. Zeier, and N. Khaneja. Elliptic functions and efficient control of ising spin chains with unequal couplings. *Phys. Rev. A*, 77:032340, Mar 2008.

[194] M. Grace, C. Brif, H. Rabitz, I. A. Walmsley, R. L. Kosut, and D. A. Lidar. Optimal control of quantum gates and suppression of decoherence in a system of interacting two-level particles. *Journal of Physics B: Atomic, Molecular and Optical Physics*, 40(9):S103, 2007.

[195] J. J. Morton and B. W. Lovett. Hybrid solid state qubits: the powerful role of electron spins. *arXiv preprint arXiv:1103.0418*, 2011.

[196] P. Maurer, G. Kucsko, C. Latta, L. Jiang, N. Yao, S. Bennett, F. Pastawski, D. Hunger, N. Chisholm, M. Markham, et al. Room-temperature quantum bit memory exceeding one second. *Science*, 336(6086):1283–1286, 2012.

[197] M. Mehring. High resolution nmr in solids, 2008.

[198] M. A. Nielsen and I. L. Chuang. *Quantum computation and quantum information*. Cambridge university press, 2010.

[199] J. L. O'Brien, G. Pryde, A. Gilchrist, D. James, N. Langford, T. Ralph, and A. White. Quantum process tomography of a controlled-not gate. *Physical review letters*, 93(8):080502, 2004.

[200] D. F. James, P. G. Kwiat, W. J. Munro, and A. G. White. Measurement of qubits. *Physical Review A*, 64(5):052312, 2001.

[201] M. A. Nielsen. A simple formula for the average gate fidelity of a quantum dynamical operation. *Physics Letters A*, 303(4):249–252, 2002.

[202] J. Rabeau, P. Reichart, G. Tamanyan, D. Jamieson, S. Prawer, F. Jelezko, T. Gaebel, I. Popa, M. Domhan, and J. Wrachtrup. Implantation of labelled single nitrogen vacancy centers in diamond using 15 n. *Applied Physics Letters*, 88(2):023113–023113, 2006.